

TD

**Advanced Modeling
of Plasma-Cathode Interaction
in Vacuum and Unipolar Arcs**

DOCTORAL THESIS

Helena Teresa da Costa Kaufmann

DOCTORATE IN PHYSICS



UNIVERSIDADE da MADEIRA

A Nossa Universidade

www.uma.pt

September | 2018

**Advanced Modeling
of Plasma-Cathode Interaction
in Vacuum and Unipolar Arcs**

DOCTORAL THESIS

Helena Teresa da Costa Kaufmann

DOCTORATE IN PHYSICS

SUPERVISORS

Mikhail S. Benilov
Mário Dionísio Cunha

*Dedicated to the glowing memory of Werner Hartmann,
a brilliant scientist, an enthusiastic mentor and a dear friend.*

Acknowledgements

I wish to thank my supervisors, Prof. Mikhail Benilov and Mário Cunha, for offering me the opportunity to work toward my PhD in the very interesting and complex field of plasma-cathode interactions in arc discharges. They have provided me with a truly gratifying and unique experience of conducting my research within the long-established and successful collaboration with Siemens AG, and have supported me through the relentless difficulties that came with developing the complex numerical model for the work of this thesis. I must thank Prof. Benilov for pushing me to grow as a person and as a scientist, for his weekly insistence that, once the model was (finally) successfully running, he was expecting microexplosions, and for being wildly enthusiastic when the results showed that no explosions occurred, and droplets detached instead. I thank Mário for frequently reminding me that no matter how many unsuccessful attempts there are in solving a problem, as long as there are ideas for more possible solutions, the work will always move forward. I thank them both for their support, for keeping me motivated and for their trust in my abilities to successfully complete the tasks of the project with Siemens.

I am grateful to Norbert Wenzel and to the late Werner Hartmann of Siemens AG for kindly welcoming me into the ongoing research project and the many fruitful discussions about the physics of vacuum arcs and about numerical modeling with COMSOL Multiphysics. I am especially grateful for the invitation to spend several weeks with the Corporate Technology division in Erlangen, which afforded me an insight into the research and development process of vacuum circuit breakers and interrupters and allowed a hands-on learning experience with useful modeling tools.

A special and heartfelt thank you is due to Werner Hartmann, the initiator of the work leading to this thesis, who passed away prematurely. His enthusiasm for this work was contagious, his scientific brilliance was inspiring, and his pleasure at seeing the results of the simulations for the first time is remembered fondly and with a sense of accomplishment. I also thank his wife Angelika and his daughter Leonie for welcoming me into their home and indulging mine and Werner's discussions of work over delicious margaritas.

I am thankful to Kevin G. Honnell and Scott D. Crockett of Group T-1 of the Los Alamos National Laboratory for providing the equation of state data for copper from the SESAME EOS library.

I thank my colleague and friend Pedro Almeida for guiding my first steps in the field of gas discharge physics while I was still a Physics undergraduate at Imperial College, and for listening to my frustrated ramblings about the many setbacks during the development of the model of this work. His incentive to persevere and constant

reminders that "it will pass", and his insistence on breaks and activities outside the immediate realm of the PhD contributed to the preservation of my sanity and my determination to see the work through till the end.

I would also like to thank my colleagues and fellow PhD students, Gabriel, Nelson, Nuno, Diego and Matt for creating a friendly and animated environment for sharing our struggles with COMSOL and other assorted software, discussing physics and providing comic relief in between long hours of hard work.

Last, but certainly not least, I must thank my parents and sister for their unwavering support. They have always been willing and available to listen to my ongoing rambles, complaints and achievements throughout this work, and offered invaluable advice, despite understanding very little to nothing of what it was that I was doing in my research.

Preamble

The work leading to this thesis was performed within activities of:

- Research Fellowship BI-1/PTDC/FIS-PLA/2708/2012 in the framework of the project PTDC/FIS-PLA/2708/2012 *Modelling, understanding, and controlling self-organization phenomena in plasma-electrode interaction in gas discharges: from first principles to applications* of Fundação para a Ciência e a Tecnologia.
- Research project *Investigation of interaction of vacuum arcs with contacts with application to vacuum circuit breakers* in the framework of the collaboration between Universidade da Madeira and Siemens AG, Corporate Technology.
- Project Pest-OE/UID/FIS/50010/2013 of Fundação para a Ciência e a Tecnologia.

Most of the results presented in this thesis are published in the following articles:

- M. D. Cunha, H. T. C. Kaufmann, M. S. Benilov, W. Hartmann, and N. Wenzel, Detailed numerical simulation of cathode spots in vacuum arcs - I (2017), IEEE Trans. Plasma Sci. 45, No. 8, 2060-2069
- H. T. C. Kaufmann, M. D. Cunha, M. S. Benilov, W. Hartmann, and N. Wenzel, Detailed numerical simulation of cathode spots in vacuum arcs: Interplay of different mechanisms and ejection of droplets (2017), J. Appl. Phys. 122, No. 16, 163303-1-14

Results presented in this thesis were reported at the following conferences:

- H. T. C. Kaufmann, M. D. Cunha, M. S. Benilov, W. Hartmann, and N. Wenzel, Detailed numerical simulation of cathode spots in high-current vacuum arcs, Proc. 27th International Symposium on Discharges and Electrical Insulation in Vacuum (September 16-23, 2016, Suzhou, China), ISBN 978-1-4673-9779-4, pp. 405-408
- H. T. C. Kaufmann, M. D. Cunha, M. S. Benilov, W. Hartmann, and N. Wenzel, Simulating Ignition and Development of Cathode Spots in Vacuum Arcs, 44th IEEE International Conference on Plasma Science (May 21-25, 2017, Atlantic City, New Jersey, USA)

- H. T. C. Kaufmann, M. D. Cunha, M. S. Benilov, W. Hartmann, and N. Wenzel, Simulating Ignition and Development of Cathode Spots in Vacuum Arcs, 33rd ICPIG (July 9-14, 2017, Estoril, Lisbon, Portugal), ed. by L. L. Alves and A. Tejero-del-Caz
- H. T. C. Kaufmann, M. D. Cunha, M. S. Benilov, W. Hartmann, and N. Wenzel, Advanced modeling of plasma-cathode interaction in vacuum and low pressure arcs, Proc. 28th International Symposium on Discharges and Electrical Insulation in Vacuum (September 23-28, 2018, Greifswald, Germany), in press
- M. S. Benilov, H. T. C. Kaufmann, W. Hartmann, and L. G. Benilova, On the mechanism of retrograde motion of cathode spots of vacuum arcs, Proc. 28th International Symposium on Discharges and Electrical Insulation in Vacuum (September 23-28, 2018, Greifswald, Germany), in press

Resumo

Este trabalho é dedicado à modelação da interacção plasma-cátodo em descargas de arco em vácuo e em descargas de arco unipolares.

Pela primeira vez foi desenvolvido um modelo numérico detalhado de manchas catódicas solitárias em descargas de arco em vácuo. O modelo leva em conta todos os mecanismos relevantes dos fenómenos físicos de manchas catódicas: o bombardeamento da superfície do cátodo por iões provenientes de um plasma pré-existente; a vaporização do material do cátodo na mancha, a ionização deste material vaporizado e a interacção do plasma produzido com o cátodo; desenvolvimento do efeito de Joule no interior do cátodo; fusão do material do cátodo e movimento do metal fundido sob o efeito da pressão exercida pelo plasma e da força de Lorentz; a deformação da superfície fundida do cátodo; a formação de crateras e jactos de metal fundido; a ejeção de gotas. Os resultados da modelação permitem identificar as diferentes fases da vida de uma mancha solitária. A emissão de electrões da superfície do cátodo e o transporte de calor por convecção são os mecanismos dominantes de arrefecimento na mancha catódica, limitando deste modo a temperatura máxima possível no cátodo. A formação de crateras na superfície do cátodo ocorre sem explosões, seguida da formação de um jacto de metal fundido e da ejeção de uma gota. Os resultados da modelação são concordantes com estimativas efectuadas para diferentes mecanismos de erosão do cátodo, com base nos dados experimentais relativos à erosão em cátodos de cobre de descargas de arco em vácuo.

A fase inicial de uma descarga de arco unipolar em condições relevantes para a fusão nuclear em reactores tokamak foi investigada no âmbito do modelo detalhado de manchas catódicas solitárias em descargas de arco em vácuo. Mais concretamente, a interacção de um fluxo intenso de energia com uma placa de tungsténio imersa num plasma de hélio e a correspondente transferência de corrente foi estudada em condições baseadas em experiências laboratoriais. Uma vez que o arco é de natureza unipolar, a transferência de corrente fora da mancha é tida em consideração no modelo utilizado e a variação do potencial da placa é avaliada a partir da condição de corrente total nula transferida para a placa a cada instante. Os resultados da modelação revelam a formação de uma cratera, mas sem a formação de um jacto de metal fundido ou a ejeção de uma gota. A modelação é realizada para diferentes condições e demonstra-se que é necessário ter em consideração a limitação da corrente termiônica de electrões

pela baínha de carga de espaço.

Palavras chave: Interação plasma-cátodo, Descargas de arco em vácuo, Descargas unipolares, Manchas catódicas

Abstract

This work is dedicated to modeling of the plasma-cathode interaction in vacuum and in unipolar arcs.

A detailed numerical model of individual cathode spots in vacuum arcs has been developed for the first time. The model takes into account all the relevant mechanisms of the physics of cathode spots: the bombardment of the cathode surface by ions coming from a pre-existing plasma cloud; vaporization of the cathode material in the spot, its ionization, and the interaction of the produced plasma with the cathode; Joule heat generation in the cathode body; melting of the cathode and motion of the molten metal under the effect of the plasma pressure and the Lorentz force; the change in shape of the molten cathode surface; the formation of craters and liquid-metal jets; the detachment of droplets. The simulation results allow the identification of the different phases of life of an individual spot. Electron emission cooling and convective heat transfer are dominant mechanisms of cooling in the spot, limiting the maximum temperature of the cathode. Craters are formed on the surface without explosions, followed by the the formation of a liquid-metal jet and the ejection of a droplet. The modeling results conform to estimates of different mechanisms of cathode erosion derived from the experimental data on the net and ion erosion of copper cathodes in vacuum arcs.

The initial stage of unipolar arcing in fusion-relevant conditions was investigated in the framework of the detailed model of cathode spots in vacuum arcs. In particular, the interaction of an intense heat flux with and current transfer to a tungsten metal plate immersed in a helium background plasma is studied in conditions based on experiments. Since the arc is unipolar, the model is supplemented with an account of current transfer outside the arc attachment and the arc voltage is evaluated from the condition of the net current transferred to the plate being zero at each moment. The simulation results reveal the formation of a crater, but no jet formation or droplet detachment. Simulations are performed for different sets of conditions, and it is found that in order for the developed model to be applicable to real experimental situations, space-charge limited thermionic electron emission must be considered.

Keywords: Plasma-cathode interaction, Vacuum arc discharges, Unipolar arcs, Cathode spots

Contents

1	Introduction	1
1.1	Plasma-cathode interaction in vacuum arcs	2
1.2	Plasma-cathode interaction in unipolar arcs	12
1.3	This work	16
2	Thermal development of an individual cathode spot in a vacuum arc	19
2.1	Introduction	19
2.2	The model	20
2.2.1	Equations and boundary conditions	20
2.2.2	Material functions	22
2.3	Results	25
2.4	Concluding discussion	33
3	Detailed numerical simulation of cathode spots in vacuum arcs: Interplay of different mechanisms and ejection of droplets	35
3.1	Introduction	35
3.2	The model	36
3.2.1	Equations and boundary conditions	36
3.2.2	Material functions	37
3.2.3	Plasma pressure acting on the cathode surface	38
3.2.4	Numerical Implementation	41
3.2.5	Validation of the model	45
3.3	Numerical results and discussion	46
3.3.1	Results	46
3.3.2	Effect of motion of the melt on the spot development	51
3.3.3	Effect of the plasma produced in the spot	52
3.3.4	Effect of magnetic field on the hydrodynamics of the molten metal in the spot	55
3.3.5	Cathode erosion	56
3.3.6	Comparison with other cathode spot models	61
3.4	Summary and concluding remarks	63
4	Numerical simulation of the initial stage of unipolar arcing in fusion-relevant conditions	66
4.1	Introduction	66

4.2	The model	67
4.2.1	Equations and boundary conditions	67
4.2.2	Material functions	72
4.3	Numerical results	75
4.4	Discussion	81
4.4.1	Comparison with spots in vacuum arcs	81
4.4.2	Effect of the nanostructure layer	82
4.4.3	Space-charge limited electron emission current	84
4.5	Summary and concluding remarks	86
5	Conclusions of the thesis	88
A	Equation of state	92
	Bibliography	93

List of Figures

1.1	Schematic representation of the life cycle of an individual cathode spot.	3
1.2	Results of simulation of the crater and jet formation for copper cathodes of vacuum arcs. From [53] (a) and [55] (b).	8
1.3	Schematic of a double sheath with ionization of emitted atoms; from [61].	9
1.4	Densities of the electric current j and energy flux q from the plasma to the cathode, evaluated with the model [61, 62]. Copper cathodes, $U = 20$ V.	10
1.5	Near-cathode plasma layer parameters evaluated with the model [64]. (a) Electric potential as a function of the distance from the cathode surface. (b) Total current density J . (c) Total energy flux density E . From [64].	11
1.6	Erosion traces and craters observed on cathodes of vacuum arcs. From [25].	12
1.7	Equilibrium potentials of an isolated plate immersed in a plasma; from [16].	13
1.8	(a) Arc trails on the tungsten plate; from [86]. (b) Micrograph of the plate surface covered in nanostructures; from [75].	14
2.1	(a) Thermal conductivity of copper; points: data according to [107–109, 112]; lines: fit formula used in this work. (b) Electrical resistivity of copper; points: data according to [109–112]; line: Wiedemann-Franz law (2.8).	24
2.2	Copper density as a function of temperature. Points: data according to [115–117]; line: fit formula used in this work.	24
2.3	Temporal evolution of the maximum temperature in the cathode with the microprotrusion.	26
2.4	Evolution of the temperature distribution in the cathode with the microprotrusion. $a = 5 \mu\text{m}$, $\tau = 70$ ns. The bar in K.	28
2.5	Temporal evolution of the maximum temperature in the planar cathode.	29
2.6	Evolution of the temperature distribution in the planar cathode. $a = 5 \mu\text{m}$, $\tau = 125$ ns. The bar in K.	29
2.7	q_{em} : energy removed from the cathode surface due to electron emission. $q_i^{(v)}$, $q_i^{(cl)}$: energies delivered to the cathode surface by the ions produced by ionization of the vapor emitted in the spot and by the ions from the leftover plasma cloud, respectively.	31

2.8	Evolution of spot current. $a = 5 \mu\text{m}$. (a) Cathode with the microprotrusion. (b) Planar cathode.	31
2.9	Parameters of the near-cathode plasma layer inside the spot. p_v : saturated vapor pressure. j_1 : density of electric current to the cathode surface due to plasma produced from the metal vapor emitted by the spot. E_w : electric field at the cathode surface. t_i : time of flight of the ions across the sheath. τ_i : time scale of ionization of the emitted vapor atoms. d : sheath thickness.	32
3.1	(a) Viscosity of liquid copper; points: data according to [115]; solid line: fit formula according to [115]; dotted line: fit formula used in this work. (b) Surface tension coefficient of liquid copper; data is shown according to [121–124].	39
3.2	p_1 : the pressure exerted by incident ions produced by the ionization of the metal vapor emitted in the spot as function of the cathode surface temperature T_w . $p_i^{(cl)}$: pressure due to incident ions originating from the leftover plasma cloud. p_v : saturated vapor pressure.	41
3.3	Jet formation computed with the simplified model. (a) Temperature distribution computed with the simplified model. The bar in K. (b) Temperature distribution reported in [53]. (a), (b) The results shown were computed for the same conditions of incident plasma pressure and heat flux.	46
3.4	Evolution of the temperature distribution and cathode surface deformation. Cathode with the microprotrusion. The bar in K.	47
3.5	Evolution of the temperature distribution and cathode surface deformation. Planar cathode. The bar in K.	48
3.6	Temporal evolution of the maximum cathode temperature. (a) Cathode with the microprotrusion. (b) Planar cathode. HD&V: full model. V: model without account of the motion of the melt (the account of the plasma produced in the spot is retained), chapter 2. HD: model without account of the plasma produced in the spot (the account of the motion of the melt is retained).	49
3.7	Temporal evolution of the spot current. Solid: cathode with the microprotrusion. Dotted: the planar cathode. HD&V: full model. V: model without account of motion of the molten metal, chapter 2.	49
3.8	Temporal evolution of the spot current (a) and the power dissipated due to Joule heating (b). Cathode with the microprotrusion. HD&V: full model. V: model without account of motion of the molten metal, chapter 2.	52
3.9	Evolution of the temperature distribution and cathode surface deformation for the case of the planar cathode. The plasma produced by ionization of the emitted vapor is neglected. The bar in K.	54
3.10	Temporal evolution of the force exerted over the cathode surface by incident ions (plasma pressure) (a) and the maximum velocity acquired by the molten metal (b). Planar cathode.	55

3.11	(a) Temporal evolution of the maximum self-induced magnetic field in the spot. (b) Effect of the magnetic field on the crater and liquid-metal jet formation; $t = 55$ ns. (c) Effect of the magnetic field on the droplet detachment; $t = 70$ ns. (b), (c) Solid line: the self-induced magnetic field is neglected; dotted line: the self-induced magnetic field is amplified by a factor of 10.	57
3.12	Schematic of cathode erosion based on estimates of different mechanisms of cathode erosion derived from the experimental data on net and ion erosion of copper cathodes.	60
3.13	Result of simulation of spots on a planar copper cathode in a vacuum arc: temperature distribution and ejected "ring" droplet. The bar is in K.	61
3.14	Jet formation and droplet detachment as a result of simulations with the model [55].	62
3.15	Formation of a jet, resulting from simulation with the simplified test model based on the work [53]. Level-set function distribution. (a): $\varepsilon_{ls} = 50$ nm. (b): $\varepsilon_{ls} = 10$ nm.	63
4.1	Computed values of q_1 , j_1 and p_1 . The solid lines represent values obtained with the model of this work. The dotted lines represent values obtained with the model of near-cathode space-charge sheaths developed for vacuum arcs [61, 62].	73
4.2	Evolution of the temperature distribution and plate surface deformation, in conditions of simulation 1. The bar in K. The black line represents the melting temperature isotherm.	76
4.3	Results of simulation of the unipolar arc burning in tungsten vapor, in conditions of simulation 1. Temporal evolution of: (a) the plate potential and of the maximum plate temperature; (b) the current transferred by the tungsten plasma in the spot; (c) the maximum pressure exerted by the tungsten plasma and the maximum velocity acquired by the molten metal.	77
4.4	Evolution of the temperature distribution and plate surface deformation, in conditions of simulation 2. The bar in K. The black line represents the melting temperature isotherm.	78
4.5	Results of simulation of the unipolar arc burning in tungsten vapor, in conditions of simulation 2. Temporal evolution of: (a) the plate potential and of the maximum plate temperature; (b) the current transferred by the tungsten plasma in the spot; (c) the maximum pressure exerted by the tungsten plasma and the maximum velocity acquired by the molten metal.	79
4.6	Evolution of the temperature distribution and plate surface deformation. The model takes into account the nanostructure layer. The bar is in K. (a), (b) The heated nanostructure layer is shown in detail. (b) The black line represents the melting temperature isotherm. (c) Global overview of the forming crater.	83

4.7	Temporal evolution of the maximum plate temperature in conditions of simulation 2. Dotted: model with account of the nanostructure layer. Solid: model without account of the nanostructure layer (from figure 4.5a).	84
4.8	Dependence of the current I_3 transferred by the helium background plasma on the voltage drop U between the surrounding plasma and the plate. Plate radius of 10 mm.	86
A.1	Lines: data on the equation of state for copper [160]. Points: mass density of liquid copper evaluated by means of a fit formula with the use of data [115, 116] and saturated vapor pressure evaluated by means of the formula [109].	93

Chapter 1

Introduction

Gas discharges have been a phenomenon of great interest for several decades in various fields of Physics, Engineering, Biophysics, and most recently, even Medicine. Arc discharges are one of many types of gas discharges, characterized by a bright plasma column attached to two electrodes, an anode and a cathode. Such-type discharges are self-sustaining, with low arc burning voltages of less than 100 V (usually of about 10 – 30 V), and large currents typically of 1 A to several kA; cathodes of arc discharges receive high amounts of energy from ions and electrons, resulting in high temperatures of the cathode, which can lead to significant surface vaporization and material erosion; e.g., [1–4]. The current continuity at the cathode is ensured by the emission of electrons resulting from thermionic, field or thermo-field emission.

Arc discharges are largely divided into two categories: discharges in an ambient gas and discharges in vacuum. They are distinguishable by the medium ensuring the transfer of current between the electrodes: in the former case, current is transferred by the plasma produced from the ionization of the ambient gas, while in the latter case, the current is transferred by the plasma produced from the ionization of material vaporized from the cathode surface. There is a great variety of arc discharge devices designed for very different industrial applications, e.g., high-power vacuum circuit interrupters [4–7], low-voltage circuit breakers [8], arc welding [9–11], high-intensity discharge lamps [12, 13], metallurgy [14], hazardous waste treatment [15], among many others. The understanding of the plasma-electrode interaction in arc discharges is currently one of the most important research topics concerning arc discharge devices and their industrial applications.

Normally, the most common occurrence of arc discharges is between two metal electrodes, however, in particular conditions, an arc discharge may also be triggered between the plasma and an isolated metal wall of the plasma-containing vessel. In this case, the metal wall acts as both the cathode and the anode: the current circulates

between the wall and the surrounding plasma, and the net current to the wall is zero. This unique type of arc discharge is called a unipolar arc [16]. The erosion of plasma-facing components in fusion devices is thought to be due to unipolar arcing, triggered by instabilities in the plasma during the device operation; this is a well-known and longstanding research issue [17].

Arc discharges have been the subject of extensive investigations for many decades; e.g., [1, 3, 4, 16, 18–25] and references therein. The present work is concerned with the plasma-cathode interaction and the erosion of the cathode in high-current vacuum arcs and in unipolar arcs; particular emphasis is thus given to the physics and modeling of cathode spots and related phenomena in vacuum arc discharges, and the applicability of similar concepts and modeling to unipolar arcs.

1.1 Plasma-cathode interaction in vacuum arcs

The erosion of cathode material in vacuum arcs provides the medium for the discharge, the cathode vapor, and the understanding of the plasma-cathode interaction is one of the most important issues in the theory of vacuum arcs. In some cases, current transfer to cathodes of vacuum arcs can occur in the diffuse mode. This happens when the average temperature of the cathode surface is high enough, typically around 2000 K; e.g., [26] and references therein. It is interesting to note that the physics of this regime, while supposedly being relatively simple, still have not been fully understood; [27] and references therein. On the other hand, in most cases the current on the cathode of a vacuum arc is localized in bright, narrow regions, or cathode spots.

Cathode spots in vacuum arcs have been an object of careful experimental investigations; e.g., [3, 4, 28–32] and references therein. Data on the spot diameter and current per spot given by different authors shows that cathode spots are characterized by several scales; review [3] and references therein. The common categorizations are: spot, macrospot or group spot, with a diameter in the range 50 – 300 μm and current per spot of several tens to a few hundred amperes; fragments, microspots or subspots, with 10 – 25 μm in diameter and 2 – 25 A of current per spot; and sub-fragments or cells, with a diameter below 10 μm and a current per spot of a few amperes. Furthermore, it is known that the spots oscillate between non-stationary stages of the order of a few nanoseconds, and more or less stationary stages lasting longer than 1 μs .

The most commonly accepted understanding of the life cycle of an individual (micro-) spot is illustrated in figure 1.1 and may be described as follows; e.g., [3, 23, 33] and references therein. Micrometer-scale nonuniformities, e.g., microprotrusions, are characteristic of cathode surfaces. It is assumed that a plasma cloud (a plasma generated at the arc triggering or a plasma left over from a previous spot) is present

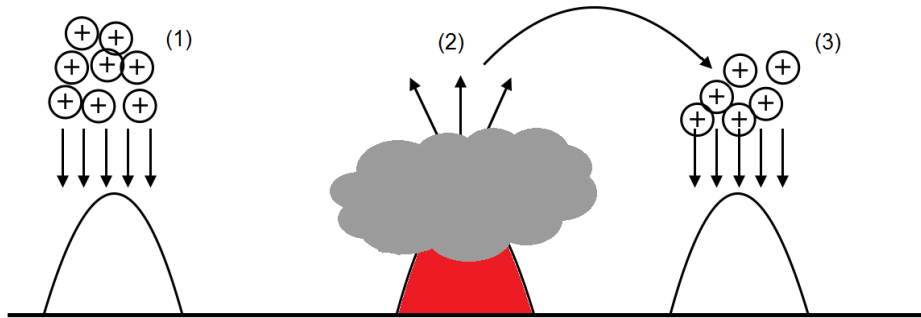


Figure 1.1: Schematic representation of the life cycle of an individual cathode spot.

in the vicinity of such a microprotrusion. The ion current from the cloud heats the cathode surface (1), thus igniting a spot. The microprotrusion is rapidly overheated through Joule heating and the Nottingham effect (i.e., the heating, rather than cooling, due to emission of electrons, which is thought to be an important mechanism in the pre-explosion stage) and explodes, with the resulting metal vapor expanding in all directions (2). This metal vapor is ionized and, in turn, starts heating a nearby protrusion (3), *etc.*

The above physical scenario is known as an explosive emission center, or ecton, e.g., [19, 23, 34, 35]. It was first suggested a long time ago, but still remains a hypothesis; experimental observations and measurements cannot provide an unambiguous verification. In such a situation, it is natural to attempt a validation of this hypothesis by means of a self-consistent numerical modeling of an individual cathode spot in a vacuum arc. This task is hindered by the diverse and complex nature of mechanisms dominating the physics of cathode spots: the bombardment of the cathode surface by ions coming from the leftover plasma cloud; vaporization of the cathode material in the spot, its subsequent ionization and the interaction of the produced plasma with the cathode; Joule heating in the cathode body; melting of the cathode and motion of the molten metal under the effect of the plasma pressure and the Lorentz force; the change in shape of the molten cathode surface; the formation of craters and liquid-metal jets; the detachment of droplets. There seems to be no available literature in which all these effects have been taken into account.

Several decades of research have resulted in a variety of approaches available in the literature for modeling cathode spots in vacuum arcs. The state of the art, as of 2013 when the work leading to this thesis was initiated, was as follows. Modeling approaches were comprised of space-resolved descriptions of spots based on numerical solution of 1D [36–43] and 2D [44–51] differential equations. Many of these available models considered the existence of an external plasma which provided ions that entered the

cathode sheath with the Bohm speed and impinged on the cathode surface. This ion source, with a given (assumed) spatial and temporal distribution, heated the cathode and initiated the spot. The development of the spot was computed with the heat conduction equation, taking into account Joule heating and the energy balance at the cathode surface. In a number of works [37, 38, 40, 43, 45, 46, 48–50], such modeling revealed a fast increase of temperature in a certain region of the cathode body up to values exceeding the critical temperature of the cathode material. This phenomenon was interpreted as a microexplosion of the cathode (in agreement with the above-described life cycle of an individual spot) and is often called thermal runaway. This is a thermal instability, characterized by a rapid and unlimited increase of the temperature in the bulk of the cathode, caused by a positive feedback between the Joule heat production in the cathode body and temperature because of the Wiedemann-Franz law (or a similar dependence of the thermal resistivity with the temperature) [22, 52].

In [36], a simple 1D model of a stationary cathode spot was proposed whose purpose was to investigate the dependence of the spot parameters on various parameters, such as the plasma temperature, dimensions of protrusions, electric field strength at the protrusion tip and maximum energy flux delivered by the plasma to the surface.

In [38] a 1D-spherically symmetric model was proposed to determine conditions necessary for the initiation and sustainment of a cathode spot. The spot was assumed to be located within an already existing hemispherical crater of a given radius. The cathode surface was initially exposed to a uniform electric field, generated due to the ions being accelerated by a cathode voltage drop of 15 V and impinging onto the surface. Heat conduction in the bulk of the cathode was evaluated through the Fourier equation, written as a power balance equation accounting for several heat production and dissipation mechanisms, namely ion impact heating, electron emission cooling, Joule heat generation, evaporation cooling and radiation cooling. The restriction of a constant crater radius was imposed, a condition also valid during the spot operation (the assumption was that the cathode spot operated at mass equilibrium conditions, i.e., the evaporated mass returned to the cathode in the form of ions and condensed back onto the surface). Thermal runaway occurred on different time scales, from a few nanoseconds to a few seconds, depending on the initial parameters. Work [37] presented a similar model, with an initially imposed arc current in the crater; however, in contrast to [38], the expansion of the initial crater was taken into account. The computed results agreed well with experimental findings for the lower limits of spot lifetimes and final crater radii. Work [40] expanded on the model [37] with the aim to improve the previous results and was successful in computing the upper limits of spot lifetimes and final crater radii in agreement with the experimental data.

The work [44] proposed a 2D self-consistent model of quasi-stationary spots of arc

discharges based on a model of non-linear surface heating [39]. The model allowed the self-consistent determination of integral parameters of the spot, such as the spot current and the spot radius, without resorting to empirical parameters or arbitrary assumptions used in most previous theories. It is important to note that the model [44] is the basis of the most commonly used self-consistent models of plasma-cathode interaction in high-pressure arcs; e.g., review [24].

In [45] a 2D numerical model was developed taking into account ion impact, electron emission, vaporization at the metal surface, Joule heat generation and heat conduction into the bulk. The solid to liquid phase transition was accounted for through a virtual specific heat. An infinite planar cathode was assumed, where a circular region of radius $10\ \mu\text{m}$ was under the influence of an external electric surface field, and (in specific simulation conditions) an impinging ion flux. Different sets of initial parameters were employed to determine necessary conditions for the development of thermal runaway below the surface of the cathode.

In work [49] a model was given with account of ion impact heating and electron emission cooling, and the assumption of the existence of a plasma over the cathode surface with given parameters. Cathode microprotrusions of different geometries were used in the calculations and thermal runaway was observed to develop below the surface of the protrusion. The time to explosion varied between 0.33 ns and 16 ns, depending on the geometry of the protrusion and on the initial parameters of the plasma, in particular, the ion density.

The spot initiation and development on a tungsten microprotrusion was considered in [50], and a threshold value of energy transferred to the surface was determined, above which heating becomes explosive in nature on a time scale of ~ 10 ns. This threshold value was found to be 2×10^{12} W/m² for initial plasma densities greater than 10^{24} m⁻³, with contributions from incident ions and electrons, and electron emission cooling.

The models [41, 42] simulate the transient phenomena of spot appearance and development on a bulk cathode, taking into account the existence of an initial plasma with given parameters, generated at arc triggering. A kinetic model is used to describe the near-cathode plasma and plasma expansion, together with a time-dependent heat equation for the bulk cathode. Contributions to the energy balance at the cathode surface are given by incident ion and electron fluxes, vaporization and electron emission. The initial plasma acted over the cathode over a period τ , after which it was switched off and the spot operated at a constant current, $I = 10$ A, until a steady-state was reached. Over this period τ , the near-cathode voltage and plasma density were assumed to be constant.

A kinetic 1D spherically symmetric model of heating of a droplet-on-neck type of protrusion was proposed in [43]. The protrusion was heated by the plasma-metal

interaction and Joule heating; evaporation from the surface and the corresponding plasma generation and evolution were taken into account. Contrary to what was generally described by the previous works, the thermal runaway was observed at the surface of the protrusion, with the prevailing heating mechanism being the incident plasma electrons. This heat source dominated over Joule heat generation below the surface of the protrusion, and was also greater than the surface heat sink mechanism of electron emission cooling.

In the above referenced works, the computed explosion time was in the range 1 – 20 ns for the case of cathodes with a protrusion. This is in agreement with the time scale of the cathode spot phenomena, which is in the range 1 – 10 ns [3]. However, the parameters of the initial plasma cloud necessary to achieve these values varied over several orders of magnitude. The explosion time computed for the case of a planar cathode [45] exceeds 1 μ s.

Most models neglect the hydrodynamic aspects of the problem, such as motion of the molten metal and convective heat transfer. The exception were the models proposed in [46–48]. Works [46, 48] assumed that the most important features of the physics of cathode spots of vacuum arcs were a continuous (without an interface) metal-plasma transition and an explosion-like expansion of the cathode material. A nonstationary two-temperature magnetohydrodynamic model was used with account of ionization kinetics and a wide-range equation of state. Cooling of the cathode due to extraction of the electrons from the metal seems to have been neglected. Also neglected were space charge effects. In [47], the hydrodynamic aspects were considered in a simplified way, on the basis of analysis of the pressure balance at the plasma-cathode interface. A stability criterion determined whether the molten protrusion remained stable or was removed, thus accounting for the change in shape of the cathode surface. No thermal runaway was found; the protrusion was destroyed by melting and under the action of the plasma pressure.

More recently, in the course of the work leading to this thesis, a number of more complete models of a cathode spot in a vacuum arc have been proposed [53–56]. The models [53–56] employ significantly different approximations from those in [46–48] and the results differ as well.

In [53, 54], the hydrodynamic aspects were treated in a more accurate way, on the basis of the Navier-Stokes equations. However, no mechanism of current transfer to the cathode surface was considered in [53] and only the ion current from the plasma cloud was accounted for in [54]. The spatial and temporal distributions of the heat flux density to and the plasma pressure on the cathode surface were specified as a part of input. The modeling results reveal the formation of a crater with an axially symmetric liquid-metal jet at the periphery, as a result of displacement of the molten

material due to the pressure exerted by the plasma over the cathode surface; figure 1.2a. Depending on the conditions, the jet head can reach the critical temperature. The formation of droplets does not occur in the modeling. The authors supposed that this occurs through a breaking of the axial symmetry of the jet due to the development of a hydrodynamic instability, presumably of the Rayleigh–Plateau type [57–59], so its simulation would require 3D modeling which was not attempted in [53, 54]. One of the consequences of current transfer to the cathode surface not being considered in [53] is the neglect of electron emission cooling, which is a strong effect [51, 60] that can significantly affect simulation results. The other consequence is the neglect of the pressure exerted over the cathode surface by ions produced by ionization of the vapor emitted in the spot.

The model [55, 56] is similar to [53], with the addition of an account of Joule heating and of cooling due to evaporation of atoms from the cathode surface. The plasma pressure, the current transfer to the cathode and the energy flux density due to ion bombardment from a leftover plasma cloud are input parameters. The formation of a crater and a molten metal jet is observed, as well as the ejection of droplets; figure 1.2b. In contrast to the results of [53], the critical temperature is not reached, presumably due to the account of the surface cooling by evaporation. The molten metal jet is extruded from the crater parallel to the cold, solid surface of the cathode, and several small droplets are detached from this jet under different conditions.

The models [53–56] are a large step forward in the numerical modeling of the hydrodynamic aspects of cathode spots in vacuum arcs, however key mechanisms occurring in the spot have been neglected in all these works, namely, the vaporization of the cathode material in the spot, its subsequent ionization and the interaction of the produced plasma with the cathode. To account for these mechanisms, a self-consistent model of the near-cathode plasma layer is needed, which the authors of those works were lacking and therefore could not implement in conjunction with the developed models.

A model of the near-cathode plasma layer on contacts of vacuum arcs has been proposed in [61, 62]. The work [61] provides a self-consistent numerical solution of the Poisson equation for the near-cathode space-charge sheath with ionization of emitted atoms vaporized from the cathode surface, and the results show that the distribution of the electric potential has a maximum inside the sheath. In short, atoms that are emitted by the cathode surface are gradually ionized by the plasma electrons as they move from the cathode and across the sheath. Ions produced before the maximum return to the cathode surface, while the ions produced after the maximum escape into the plasma; figure 1.3. The equation governing the production of ions is solved together with the Poisson equation, and distributions of parameters, such as

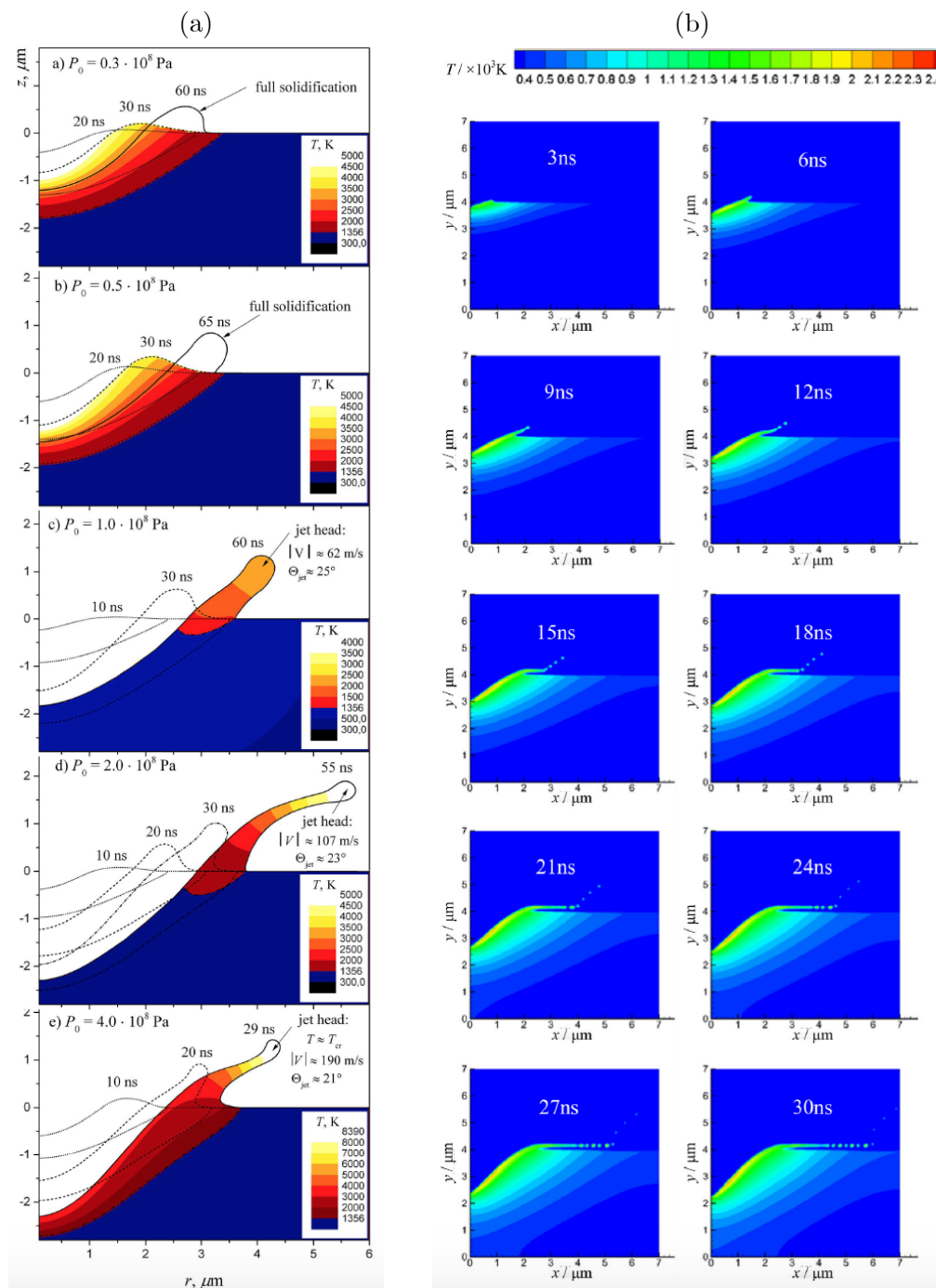


Figure 1.2: Results of simulation of the crater and jet formation for copper cathodes of vacuum arcs. From [53] (a) and [55] (b).

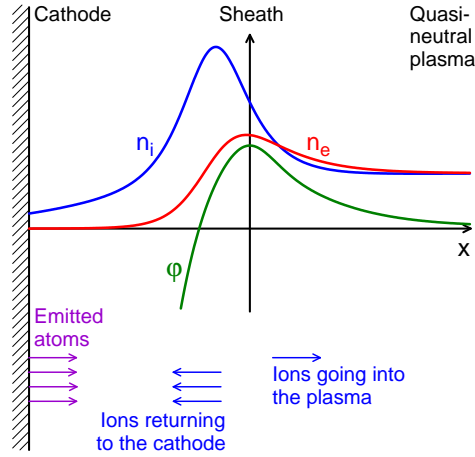


Figure 1.3: Schematic of a double sheath with ionization of emitted atoms; from [61].

the electric potential, and the densities of ions, atoms and electrons across the sheath are calculated in a self-consistent manner.

The work [61] is the basis of the model of near cathode-plasma layers developed in [62]. Parameters of the near-cathode layer, such as the electron temperature, the ion backflow coefficient, and the densities of electric current and of the energy flux from the near-cathode plasma to the surface (figure 1.4), are obtained as a result of the evaluation of the equation of balance of electron energy in the sheath. The electron emission current density is evaluated in the framework of the Murphy and Good formalism [63].

A kinetic model of formation and expansion of the near-cathode plasma was proposed in [64]. As an example, the electric potential computed as a function of the distance from the cathode surface, and the dependencies on the local cathode surface temperature T_c of the densities of electric current and of the energy flux computed with the model [64] are shown in figure 1.5, for different simulation conditions and geometry configurations.

Note that some of the results presented in [64] reveal a maximum of the potential distribution at the sheath edge, as seen in figure 1.5a, similarly to the schematic of figure 1.3 and the results of [61]. The results of [64] seem to corroborate the existence of the potential maximum, despite the given interpretation being contradictory.

For comparison with the results obtained with the model [62] for copper cathodes and a near cathode fall of 20 V, shown in figure 1.4, one should consider the distributions of figures 1.5b and 1.5c given for the geometry configuration designated by S1. It can be seen that the dependencies obtained with the two models have remarkably similar qualitative characteristics. The density of electric current grows almost exponentially with increasing surface temperature, figures 1.4a and 1.5b. The density of

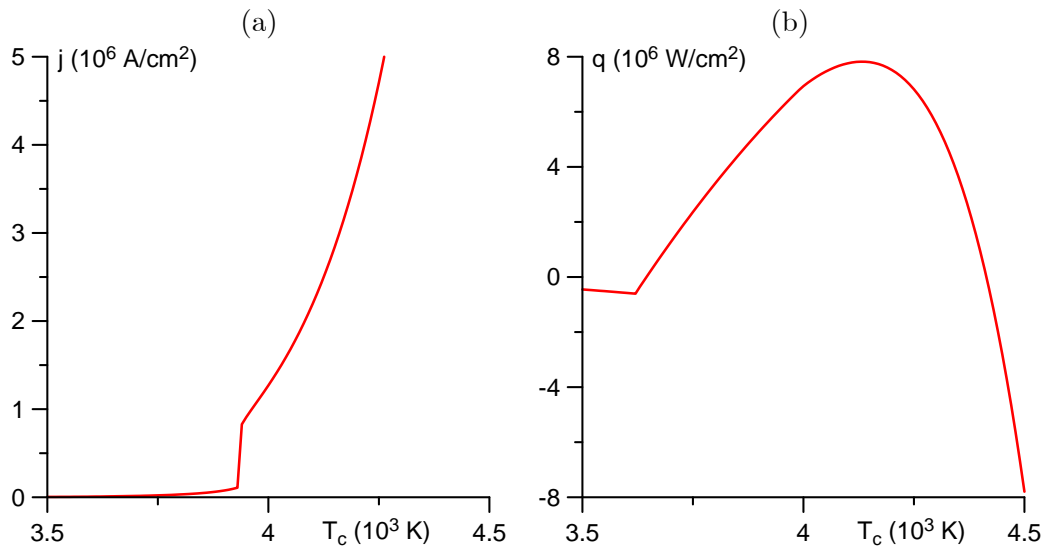


Figure 1.4: Densities of the electric current j and energy flux q from the plasma to the cathode, evaluated with the model [61, 62]. Copper cathodes, $U = 20$ V.

the energy flux is nonmonotonic with a maximum at $T_c \approx 4200$ K; figures 1.4b and 1.5c. (Up to 4200 K, the main contribution to the density of the energy flux is the heating of the cathode by ion bombardment; as the local surface temperature continues to increase, the electron emission cooling begins growing faster than the heating by the ion bombardment, and the total energy flux density becomes negative.) One can conclude that, despite the different approaches to solving the problem of the physics of the near-cathode plasma layer, the results obtained in the framework of the models [61, 62, 64] show remarkable qualitative agreement for similar conditions, and can therefore be expected to be of fundamental importance in clarifying the role of the plasma produced by ionization of the metal vapor emitted in the spot on the ignition and development of cathode spots in vacuum arcs.

In summary, although significant advances have been achieved in the last decades, the numerical modeling of cathode spots in vacuum arcs has remained inconclusive. A number of works has been dedicated to the thermal development of the spot, neglecting the hydrodynamic aspects of the problem; the resulting development of thermal runaway below the cathode surface seems to give credence to the proposed theory of formation of explosive emission centers, or ectons. The latter is currently the reigning paradigm with regard to the possible mechanisms responsible for the formation of craters on cathodes of vacuum arcs; e.g., figure 1.6 and [25, 65, 66]. Recent models have tackled the hydrodynamic phenomena in the spot and, in particular, the formation of craters and molten metal jets; while there seems to be good agreement between the predicted crater sizes and those of the experiment, the models neglected the pro-

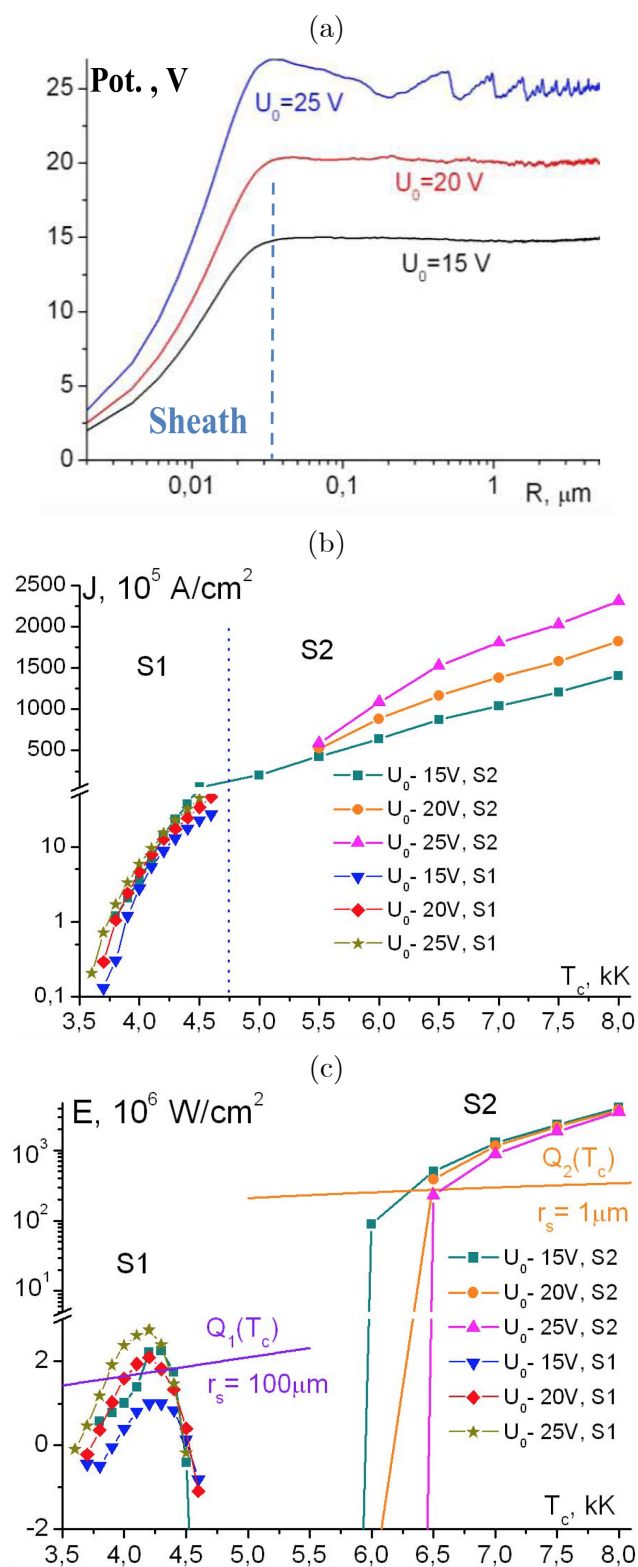


Figure 1.5: Near-cathode plasma layer parameters evaluated with the model [64]. (a) Electric potential as a function of the distance from the cathode surface. (b) Total current density J . (c) Total energy flux density E . From [64].

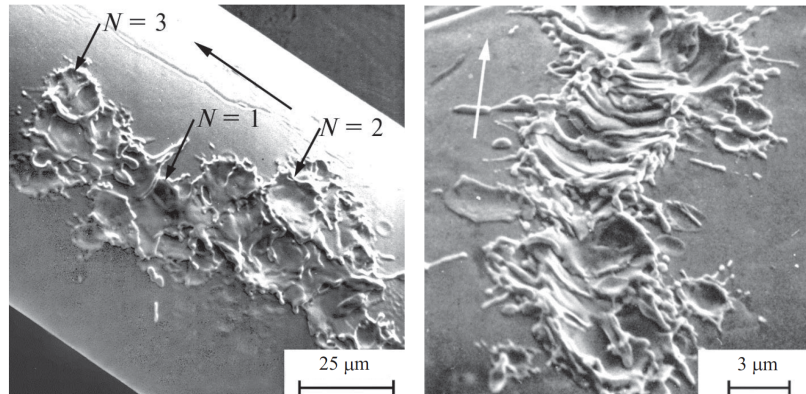


Figure 1.6: Erosion traces and craters observed on cathodes of vacuum arcs. From [25].

duction of plasma from the vaporized material in the spot, in particular, the electron emission cooling, which is one of the strongest effects that can significantly alter the simulation results.

It is clear that a model with an account of all the relevant mechanisms dominating the physics of cathode spots is still lacking. As a consequence, the field of simulation of vacuum arc-cathode interaction has become highly competitive in recent years, during the course of the work leading to this thesis. In addition to the great amount of work that has been carried out by the group of Mesyats and Uimanov at Yekaterinburg and Moscow [53, 54, 57–59], and by the group of Xi’an Jiaotong University, China [55, 56], the US Department of Energy has awarded 150,000 US\$ to CFD Research Corp. for the project "Simulations of Explosive Electron Emission in Cathodic Arcs, Phase 1" (period of performance: 06/13/2016 - 03/12/2017) [67]. The amount of 1,000,000 US\$ was awarded for Phase 2 of this project, which has recently started [68].

1.2 Plasma-cathode interaction in unipolar arcs

The erosion of plasma-facing components in fusion devices is a possible source of impurities in the core plasma, which may lead to disruptions during the device’s operation. The erosion is thought to be due to arcing between the plasma and the wall, triggered by so-called edge-localized modes (ELMs), i.e., instabilities in the plasma during its operation, which deliver high-energy particle fluxes to the walls. Since the plasma-facing components are electrically isolated, when an arc is triggered the current circulates between the plasma and the wall and the net current to the wall is zero: this is the so-called unipolar arc [16].

The mechanisms leading to the ignition of unipolar arcing may be understood as

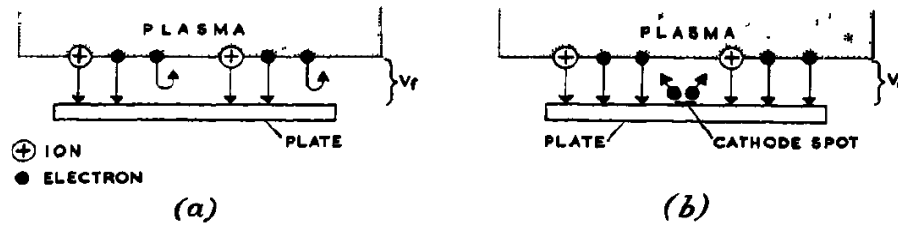


Figure 1.7: Equilibrium potentials of an isolated plate immersed in a plasma; from [16].

follows [16]. A metal plate or wall exposed to a plasma is bombarded by both electrons and positive ions. An electrically isolated plate will take up a negative potential with respect to the plasma, so that it attracts ions and repels all but the fastest electrons (i.e., the electrons that can overcome the potential in the formed sheath); in equilibrium the net current to the plate vanishes: the plate receives equal fluxes of ions and electrons. The equilibrium negative potential is known as the floating potential; figure 1.7a. A sufficiently high electron temperature of the surrounding plasma means that the floating potential exceeds the potential difference required to sustain an arc. In these circumstances, if a spot is ignited on the plate, the local emission of electrons from the spot reduces the potential difference between the plate and the plasma from the floating potential to the cathode fall potential U of the arc (or in other words, the arc burning voltage); figure 1.7b. This means that more electrons can cross the sheath and reach the plate against the retarding potential which has been lowered; outside of the immediate vicinity of the spot, a net electron current flows from the plasma to the plate. In turn, this current returns to the plasma from the arc spot, thus satisfying the condition that the total current to the plate is zero.

Arcing in fusion devices is a longstanding research issue; e.g., [17]. Until recently, it was thought that arcing was of minor importance as it is restricted to unstable phases of the plasma operation in fusion devices. However, recently this issue has gained attention (e.g., [69–71] and references therein), in particular due to the decision to begin the operation of the ITER tokamak (International Thermonuclear Experimental Reactor) with a tungsten divertor; e.g., [72] and references therein.

Many dedicated experiments and numerical modeling have been performed to study the behavior of tungsten in response to ELMs and ELM-like transient heat loads; e.g., [73–85]. As far as unipolar arcs are concerned, of particular interest is the work [75], which reports the first direct experimental observation of a unipolar arc ignited in a stationary plasma. In the experiment, an isolated tungsten plate was exposed to a helium plasma, and then irradiated by a laser pulse with a peak power of about 10^{10} W/m^2 , which corresponds to that of ELMs expected in ITER. The ignition of an

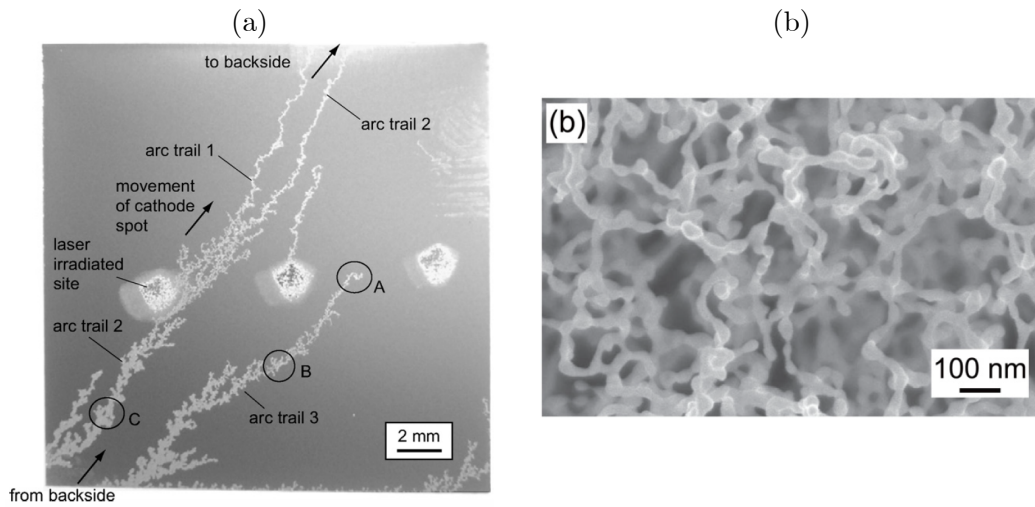


Figure 1.8: (a) Arc trails on the tungsten plate; from [86]. (b) Micrograph of the plate surface covered in nanostructures; from [75].

arc was evidenced by bright emission detected by a fast camera, the increase of the plate potential from the floating potential and by the erosion trails left on the plate, figure 1.8a, similar to what has been observed on tungsten tiles in fusion devices.

This line of research has been continued in [80, 86–92]. One of the phenomena, observed and studied in these works, is the formation of nanostructures on the surface of the tungsten plates due to the background helium plasma irradiation; figure 1.8b. It is well understood that the properties of this nanostructure layer are significantly different from those of bulk tungsten [93–96]. The thickness of this layer is a few microns, depending on the exposure time to the helium plasma. According to [75], arcing was not observed if the laser pulse irradiated the same position twice; this was thought to be due to the destruction of the nanostructures by the heat load delivered by the laser pulse in the first irradiation, which were then absent for the second irradiation. The conclusion was that the nanostructures on the plate surface are essential for arc ignition in the experimental conditions of [75].

One of the, as of yet, unanswered questions is the nature of the mechanism that determines the arc duration of approximately 3 ms in the experiment [75]. In a subsequent paper [86], it was reported that a second laser irradiation of the same tile resulted in an arc duration of approximately 0.3 ms and a third irradiation apparently resulted in no arcing. In similar experiments under different conditions, the arc duration varied from 0.6 ms [87], to a few milliseconds [88, 90].

With regard to theoretical work, a few papers [87, 89, 92] attempted simulating the behavior of arc spots with modeling based on a phenomenological description of the spot motion; special care was taken to ensure that the phenomenological model

describes grouping of the spots, which occurs in certain conditions and has an effect on the width of the erosion trails left on the plate and on the velocity of overall spot motion. In [95], a numerical analysis of the temperature evolution in the tungsten plate was carried out in an attempt to understand the temperature measurements performed in the experiment, which showed that melting of the nanostructures had occurred, despite the measured temperature never reaching the melting temperature. A number of possibilities were discussed to explain the measurements in the framework of the numerical modeling, however no definite conclusions were reached. As far as the mechanisms responsible for the unipolar arc ignition and sustainment are concerned, it had been proposed [19] that explosions of micrononuniformities on the plate surface due to field emission and Joule heating (the so-called ecton mechanism) would be a key mechanism of not only cathode spots in vacuum arcs, but also of unipolar arcs in fusion devices. This line of research was pursued in [90, 97, 98], where the experimental results of [75] and subsequent works were analyzed by means of estimates in the framework of the ecton mechanism.

The results of the above-described experimental works suggest that there are two phases of unipolar arcing. In the initial phase, arcing is triggered and sustained by an intense external heat flux, i.e., the laser pulse. After the external heat flux is switched off, arcing continues in a second phase, the mechanism of sustainment being presumably related to the nanostructures. One could think of explosions of the nanostructures due to field emission, in agreement with the ecton model [19]. Alternatively, given that heating of the surface during the initial phase is a necessary precursor for the second phase, one could think of explosions, due to thermo-field emission, of hot nanostructures in the immediate vicinity of the initial impact site, that were heated but not destroyed by the initial external heat flux irradiation.

Initial stages of formation of cathode spots in vacuum arcs are similar to the first phase of ignition of unipolar arcs in fusion devices. In short, the action of an external intense heat (and particle) flux ignites a cathode spot, and its subsequent evolution leads to the formation of a crater, and a molten metal jet at the periphery of the crater, and in some works, to the ejection of liquid droplets. At a stage when a comprehensive model of cathode spots in vacuum arcs has been developed, with account of all the relevant mechanisms, it will be of interest to apply it also for the modeling of the initial phase of unipolar arcing in fusion devices, to further the understanding of this phenomenon.

1.3 This work

The main goals of this work are as follows. As far as the plasma-cathode interaction in vacuum arcs is concerned, the aim is to develop a model and perform a numerical investigation with account of all of the relevant mechanisms of the physics of cathode spots, and thus come closer to the understanding of the nature of cathode spots of vacuum arcs. In particular, it will be shown that the effect of the plasma produced by ionization of the metal vapor emitted in the spot (neglected in the models [53–56] developed while the work of this thesis was already in progress) indeed significantly affects the development of the spot, and the formation of jets and detachment of droplets.

As far as unipolar arcs are concerned, the aim is to develop a numerical model and investigate the initial phase of unipolar arcing. More specifically, the interaction of an intense heat flux with and current transfer to a tungsten metal plate immersed in a helium background plasma in conditions based on the experiment [75] will be simulated. The detailed numerical model developed for the modeling of plasma-cathode interaction in vacuum arcs is used to this end.

The work leading to this thesis was performed within the activities of a research project between Universidade da Madeira (UMa) and Siemens AG, Corporate Technology, as far as the plasma-cathode interaction in vacuum arcs is concerned, and a collaboration between Universidade da Madeira and Instituto de Plasmas e Fusão Nuclear, Instituto Superior Técnico, as far as unipolar arcing is concerned. The majority of the thesis is a compilation of papers already published [99, 100], and a paper in preparation for publication. (It may be relevant to mention that one of the joint UMa-Siemens papers [100] on the plasma-cathode interaction in vacuum arcs, published in the Journal of Applied Physics, was selected by the editor of the journal for promotion through the American Institute of Physics Publishing’s Scilights project [101].)

The text is organized in five chapters. The first chapter represents the Introduction.

In chapter 2, corresponding to [99], the thermal development of an individual cathode spot in a vacuum arc is considered. A model of cathode spots in high-current vacuum arcs is developed with account of the plasma cloud left over from a previously existing spot, all mechanisms of current transfer to the cathode surface, including the contribution of the plasma produced by ionization of the metal vapor emitted in the spot, and the Joule heat generation in the cathode body. The simulation results allow one to clearly identify the different phases of life of an individual spot: the ignition, the expansion over the cathode surface, and the thermal explosion. The expansion phase is associated with a nearly constant maximum temperature of the cathode,

which occurs at the surface and is approximately 4700 – 4800 K. Thermal explosion is a result of a thermal instability (runaway), which develops below the cathode surface when the Joule heating comes into play. The development of the spot is interrupted if the plasma cloud has been extinguished: the spot is destroyed by heat removal into the bulk of the cathode due to thermal conduction. Therefore, different scenarios are possible depending on the time of action of the cloud: the spot may be quenched either before having been formed, or during the expansion phase, or even at the initial stage of thermal explosion.

In chapter 3, corresponding to [100], a detailed numerical model of cathode spots in high-current vacuum arcs is given with account of all the potentially relevant mechanisms. The model of chapter 2 is supplemented with an account of the motion of the molten metal under the effect of the plasma pressure and the Lorentz force, and related phenomena: deformation of the molten surface, surface tension effects, and convective heat transfer. The simulation results reveal the formation of a crater and a liquid-metal jet at its periphery, and the detachment of a droplet. No microexplosions are observed. After the spot has been ignited by the action of the cloud (which takes a few nanoseconds), the metal in the spot is melted and accelerated toward the periphery of the spot, the main driving force being the pressure due to incident ions. Electron emission cooling and convective heat transfer are dominant mechanisms of cooling in the spot, limiting the maximum temperature of the cathode to approximately 4700 – 4800 K. A crater is formed on the cathode surface in this way. After the plasma cloud has been extinguished, a liquid-metal jet is formed and a droplet is ejected. The modeling results conform to estimates of different mechanisms of cathode erosion derived from the experimental data on the net and ion erosion of copper cathodes.

In chapter 4, the detailed model developed for the modeling of the plasma-cathode interaction in vacuum arcs is used for the investigation of the initial stage of unipolar arcing in fusion-relevant conditions. The interaction of an intense heat flux with and current transfer to a tungsten metal plate immersed in a helium background plasma is studied. Since the arc is unipolar, the model is supplemented with an account of current transfer outside the arc attachment and the arc voltage is evaluated from the condition of the net current to the plate being zero at each moment. The simulation results reveal the formation of a crater, but no jet formation or droplet detachment. As the plate surface starts being subjected to the external heat load, the ignition of a spot is observed. The latter leads to a reduction of the potential difference between the plasma and the plate, from the floating potential to the arc burning voltage, which allows a greater influx of electrons from the background plasma. The current transferred by the ions and the electrons of the background plasma from the surface

of the plate into the plasma increases so as to balance the current transferred in the spot. After the external heat load is switched off, the spot is extinguished and the plate potential returns to the floating potential. Simulations are performed for different sets of conditions, and it is found that in some conditions, space-charge limited thermionic electron emission must be considered.

In chapter 5 conclusions of this work are given and possible directions of future research are discussed.

Chapter 2

Thermal development of an individual cathode spot in a vacuum arc

2.1 Introduction

The first step toward a complete numerical model of cathode spots in vacuum arcs with an account of all the relevant mechanisms, including the vaporization of the cathode material in the spot, its subsequent ionization and the interaction of the produced plasma with the cathode, began with the development of a self-consistent space-resolved numerical model of stationary cathode spots in vacuum arcs [51], which included the description of the near-cathode space-charge sheath developed in [61, 62], and the investigation of the stability of the steady-state solutions describing the stationary spots [102].

In this chapter, and building upon the description of the stationary spots developed in [51], the thermal development of a cathode spot is considered, with account of the plasma cloud left over from a previously existing spot, all mechanisms of current transfer to the cathode surface, including the contribution of the plasma produced by ionization of the metal vapor emitted in the spot, and the Joule heat generation in the cathode body. The effect of the spatial and temporal distributions of the leftover plasma on spot ignition and development is studied and the temporal evolution of the cathode temperature and of the spot current is analyzed. It is found that in the cases where the spot is ignited, it does not reach steady-state; either it explodes (thermal runaway) or is destroyed by thermal conduction after the heating by the leftover plasma has been extinguished. Results of a detailed numerical modeling with an account of hydrodynamic processes (convective heat transfer, motion of molten

2. Thermal development of an individual cathode spot in a vacuum arc 20

metal and formation of the crater, liquid-metal jet and droplets) are reported in chapter 3.

The outline of the chapter is as follows. The numerical model is introduced in section 2.2. Results of simulation are reported and discussed in section 2.3. Conclusions are summarized in section 2.4.

2.2 The model

2.2.1 Equations and boundary conditions

The model employed in this work builds upon a self-consistent space-resolved model of stationary cathode spots in vacuum arcs [51, 61, 62]. It exploits the fact that a significant power is deposited into the near-cathode space-charge sheath by the arc power supply. Part of this power is transported from the sheath to the cathode surface and the rest is transported by electric current into the arc column. The latter means that the plasma-cathode interaction, to the first approximation, is not affected by processes in the arc column. Note that this approach, which is sometimes called the model of nonlinear surface heating, has been used also in the theory and modeling of plasma-cathode interaction in arcs in ambient gases; the recent comparison of models of various levels of complexity of plasma-cathode interaction in atmospheric-pressure arcs [103] has confirmed that the model of nonlinear surface heating, while being the simplest self-consistent approach, is quite accurate.

The thickness of the near-cathode plasma layer is much smaller than the characteristic radius of the spot, hence current transfer through this layer is locally one-dimensional (1D). Therefore, the problem of plasma-cathode interaction may be solved in two steps. In the first step, characteristics of the near-cathode plasma layer are evaluated using a 1D model. In particular, the net densities of the energy flux, $q = q(T_w, U)$, and of electric current, $j = j(T_w, U)$, are found, computed as functions of the local cathode surface temperature T_w and the near-cathode voltage drop U . In the second step, the temperature T and electric potential φ distributions are calculated in the cathode body by means of solving the time-dependent heat conduction equation, written with account of Joule heat generation in the body of the electrode, and the equation of current continuity supplemented with Ohm's law:

$$\rho c_p \frac{\partial T}{\partial t} = \nabla \cdot (\kappa \nabla T) + \sigma (\nabla \varphi)^2, \quad (2.1)$$

$$\nabla \cdot (\sigma \nabla \varphi) = 0. \quad (2.2)$$

2. Thermal development of an individual cathode spot in a vacuum arc 21

Equations (2.1) and (2.2) are solved under the assumption of axial symmetry in cylindrical coordinates (r, z) . The material properties, mass density ρ , specific heat c_p , and thermal and electrical conductivities κ and σ , are treated as functions of the local temperature. Boundary conditions on the cathode surface are written in terms of densities of the energy flux, $\kappa \frac{\partial T}{\partial n} = q(T_w, U)$, and electric current, $\sigma \frac{\partial \varphi}{\partial n} = j(T_w, U)$, from the plasma to the surface, calculated in the previous step, where n is a direction normal to the cathode surface and directed outward. The boundary conditions far away from the spot are $T \rightarrow T_\infty$ and $\varphi \rightarrow 0$, where T_∞ is a given parameter (the temperature of the cathode far away from the spot).

The model employed in this chapter takes into account two contributions to the densities of energy flux q and electric current j from the plasma to the cathode surface, computed independently of each other: the plasma produced from ionization of the metal vapor emitted by the spot and the leftover plasma cloud,

$$q = q_1 + q_2, \quad j = j_1 + j_2. \quad (2.3)$$

Note that this simple superposition neglects a nonlinear interaction between the leftover plasma and the freshly-produced vapor from the spot. Contributions $q_1 = q_1(T_w, U)$ and $j_1 = j_1(T_w, U)$ are obtained by means of the model of near-cathode plasma layers in vacuum arcs [62], based on a numerical simulation of the near-cathode space-charge sheath with ionization of atoms emitted by the cathode surface [61]. Note that while electron emission from cathodes of arcs in ambient gas is of thermionic nature and is adequately described by the Richardson-Schottky formula, emission from hot cathodes of vacuum arcs is of thermo-field nature and can be adequately described by the Hantzsche fit formula [104]; see also corrections in [38] and a comparison in [105]. Since, however, this modeling is intended to describe all stages of life of a spot including ones where the cathode is cold, we do not rely on approximate formulas: the code [62] used in this work employs the Murphy and Good formalism [63]. (More precisely, the electron emission current density is evaluated by means of the method [105] and the effective work function, which governs the emission-related electron energy flux, by means of the fit formulas [106].)

The contributions of the ions from the leftover plasma cloud to the energy flux and current from the plasma to the cathode surface are written as

$$q_2 = q_i^{(\text{cl})} f_r(r) f_t(t), \quad j_2 = j_i^{(\text{cl})} f_r(r) f_t(t), \quad (2.4)$$

where $q_i^{(\text{cl})}$ and $j_i^{(\text{cl})}$ are given parameters and $f_r(r)$ and $f_t(t)$ are functions characterizing the spatial distribution and temporal variation of the leftover plasma cloud and

2. Thermal development of an individual cathode spot in a vacuum arc 22

assumed in the form

$$f_r(r) = \exp\left[-\left(\frac{r}{a}\right)^2\right], \quad f_t(t) = \begin{cases} 1, & t \leq \tau \\ \exp\left[-\left(\frac{t-\tau}{\tau_0}\right)^2\right], & t > \tau \end{cases}, \quad (2.5)$$

where a is a given parameter characterizing the spatial extension of the cloud. The plasma cloud does not change appreciably in a time interval τ and then decays with a characteristic time constant τ_0 .

Parameters $q_i^{(\text{cl})}$ and $j_i^{(\text{cl})}$ (the maximum densities of energy flux and electric current transported by the ions from the leftover plasma cloud to the cathode surface) may be expressed in terms of the maximum ion density n_i , electron temperature T_e , and average charge state Z in the plasma cloud:

$$q_i^{(\text{cl})} = j_i^{(\text{cl})} \left(U + \frac{A}{e} \right), \quad j_i^{(\text{cl})} = Z e n_i \sqrt{\frac{k Z T_e}{m_i}}, \quad (2.6)$$

where e is the electron charge, m_i is the ion mass, k is the Boltzmann constant, and the term A describes the energy with which an ion enters the sheath and the energy released at the surface due to neutralization of an ion and condensation. In the simplest case $Z = 1$, $A = kT_e/2 + A_i - A_f + A_v$, where A_i is the ionization energy, A_f is the work function, and A_v is the vaporization energy per atom.

2.2.2 Material functions

Simulation results reported in this chapter refer to copper cathodes of two geometries: a planar cathode and a cathode with a Gaussian-shaped microprotrusion of the form $z = h_0 e^{-(r/d_0)^2}$, where h_0 and d_0 are given parameters characterizing, respectively, the height and the radius of the protrusion. The values $h_0 = 1 \mu\text{m}$, $d_0 = 0.8 \mu\text{m}$ were assumed. (Note that the radius of the protrusion at $z = 0.1h_0$, given by $r_{\text{prot}} = d_0 \sqrt{\ln 10}$, equals $1.2 \mu\text{m}$.)

Data on the thermal conductivity $\kappa(T)$ of copper are shown in figure 2.1a. Note that the discontinuity in the data [107, 108] occurs at the melting point, $T_m = 1358 \text{ K}$. Also shown in figure 2.1a are the data given by the following fit formula (κ in W/m K, T in K), which is used in the modeling of this chapter:

$$\kappa = \frac{1}{2} \left(1 - \tanh \frac{T-1358}{\delta_0} \right) \kappa_1 + \frac{1}{4} \left(1 + \tanh \frac{T-1358}{\delta_0} \right) \left(1 - \tanh \frac{T-7995}{\delta_0} \right) \kappa_2 + \frac{1}{2} \left(1 + \tanh \frac{T-7995}{\delta_0} \right) \kappa_3, \quad (2.7)$$

where

$$\begin{aligned} \kappa_1 &= 418 - 0.0625T, \\ \kappa_2 &= 41.9 + 0.156T - 6 \times 10^{-5}T^2 + 1.03 \times 10^{-8}T^3 - 9.37 \times 10^{-13}T^4 + 3.43 \times 10^{-17}T^5, \\ \kappa_3 &= 9.7, \end{aligned}$$

2. Thermal development of an individual cathode spot in a vacuum arc 23

and $\delta_0 = 30$ is a smoothing parameter.

The electrical conductivity $\sigma(T)$ of copper is evaluated in terms of the thermal conductivity $\kappa(T)$ with the use of the Wiedemann-Franz law:

$$\frac{\kappa}{\sigma} = LT, \quad (2.8)$$

where $L = 2.45 \times 10^{-8} \text{ W } \Omega \text{ K}^{-2}$ is the Lorenz number. Data obtained in this way are shown in figure 2.1b. Also shown in this figure are data taken from reference books [109–111] and from the work [112]. One can see that values given by the Wiedemann-Franz law (2.8) conform remarkably well to the reference data for copper.

The specific heat values $c_p(T)$ of copper were evaluated with the use of data from [113] and with account of the latent heat of melting, which is introduced along the same lines as is done in simulation of metal casting [114],

$$c_p(T) = c_{p,\text{data}} + \Delta H \frac{1}{\Delta T \sqrt{\pi}} \exp\left(-\left(\frac{T - T_m}{\Delta T}\right)^2\right), \quad (2.9)$$

where $c_{p,\text{data}}$ are the data [113] in J/kg K, ΔH is the latent heat of fusion of copper and ΔT is the parameter characterizing the width of the assumed phase change interval.

The mass density function $\rho(T)$ for copper was evaluated with the use of experimental data [115] and estimates [116] for the mass density of liquid copper in the temperature ranges $T = 1358 - 2450 \text{ K}$ and $T = 3000 - 7000 \text{ K}$, respectively, and the value of the mass density at the critical point from [117] ($\rho = 2390 \text{ kg/m}^3$ for $T = 8390 \text{ K}$). A uniform-fit formula was constructed to ensure smooth transitions at the melting and critical temperatures to avoid numerical problems (ρ in kg/m^3 , T in K):

$$\rho = \frac{1}{2} \left(1 - \tanh \frac{T-1358}{\delta_1}\right) \rho_1 + \frac{1}{4} \left(1 + \tanh \frac{T-1358}{\delta_1}\right) \left(1 - \tanh \frac{T-8390}{\delta_2}\right) \rho_2 + \frac{1}{2} \left(1 + \tanh \frac{T-8390}{\delta_2}\right) \rho_3 \quad (2.10)$$

where

$$\begin{aligned} \rho_1 &= 8993, \\ \rho_2 &= -0.818T + 9107.565, \\ \rho_3 &= 2244.545, \end{aligned}$$

and $\delta_1 = 50$, $\delta_2 = 30$ are smoothing parameters. The resulting dependence $\rho(T)$ is shown in figure 2.2.

Contributions $q_1 = q_1(T_w, U)$ and $j_1 = j_1(T_w, U)$ and all the other characteristics of the near-cathode plasma are computed by means of a Fortran code implementing the 1D model of near-cathode plasma layers in vacuum arcs [62].

2. Thermal development of an individual cathode spot in a vacuum arc 24

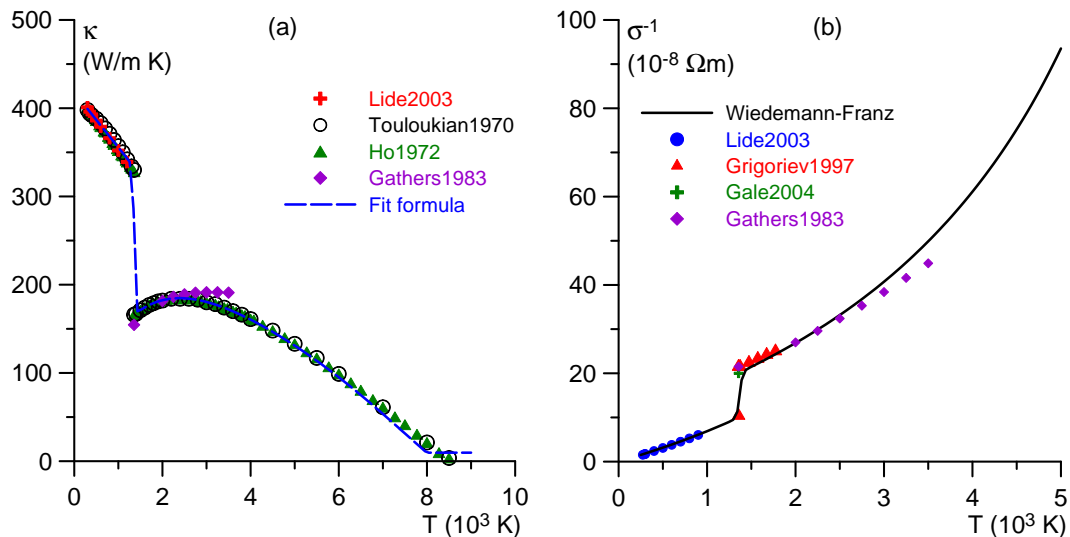


Figure 2.1: (a) Thermal conductivity of copper; points: data according to [107–109, 112]; lines: fit formula used in this work. (b) Electrical resistivity of copper; points: data according to [109–112]; line: Wiedemann-Franz law (2.8).

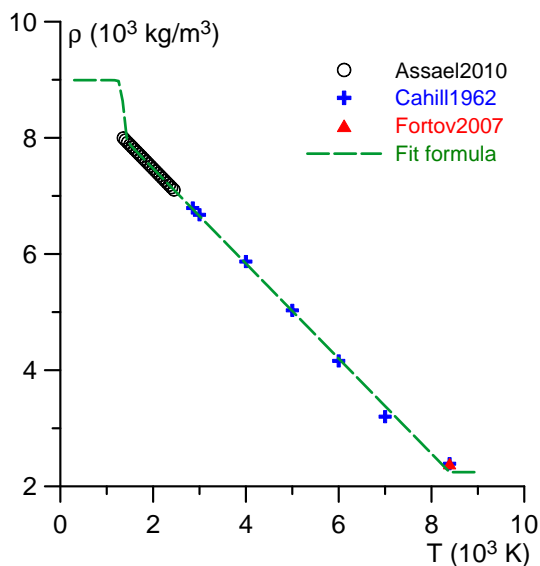


Figure 2.2: Copper density as a function of temperature. Points: data according to [115–117]; line: fit formula used in this work.

2. Thermal development of an individual cathode spot in a vacuum arc 25

Values of n_i and T_e reported in the literature vary over a wide range (e.g., [3, 33] and references therein): values of n_i higher than 10^{28} m^{-3} have been estimated for distances less than $1 \mu\text{m}$ from the cathode surface and values in the range $(1 - 6) \times 10^{26} \text{ m}^{-3}$ have been estimated for up to $5 \mu\text{m}$ from the surface; reported values of the electron temperature near the spot vary from 2 eV up to $4 - 6 \text{ eV}$. The average charge state in a vacuum arc discharge with copper electrodes has been measured as $Z \approx 2$ (e.g., [118, 119]), but the measurements have been performed in the anodic region of the arc, i.e., far away from the region of interest for this work, which is a few microns from the cathode surface. In this work, the values $n_i = 2 \times 10^{26} \text{ m}^{-3}$, $T_e = 2 \text{ eV}$, and $Z = 1$ have been assumed. The near-cathode voltage drop U is set equal to 20 V , which corresponds to initiation of spots under conditions of high-current vacuum arcs typical, e.g., for high-power circuit breakers. The term A/e in the parentheses on the rhs of the first equation (2.6) is around 7.4 V , which is small compared to U , and is neglected. This gives the values $q_i^{(\text{cl})} = 1.1 \times 10^{12} \text{ W/m}^2$ and $j_i^{(\text{cl})} = 5.6 \times 10^{10} \text{ A/m}^2$. Note that the value of $q_i^{(\text{cl})}$ is in line with the values considered by previous researchers, e.g. [49, 50, 53–55, 120]. The characteristic time τ_0 was set equal to 1 ns .

The heat conduction and current continuity equations are solved numerically by means of the commercial software COMSOL Multiphysics. The finite-element mesh is strongly non-uniform, in particular in the vicinity of the spot edge, due to a very fast variation of the density of the energy flux coming from the plasma. A free triangular mesh was used, with several successive refinements in the spot region. The boundary conditions far away from the spot are written in the same form as in [51]. The temperature of the cathode far away from the spot T_∞ was set equal to 300 K .

2.3 Results

The temporal evolution of the maximum temperature T_{max} in the body of the cathode with the microprotrusion for different values of a and τ is shown in figure 2.3. For $\tau = 10 \text{ ns}$, figure 2.3a, two scenarios are seen depending on the value of a . Scenario 1 occurs in the cases $a = 0.25$ and $0.5 \mu\text{m}$: the maximum temperature of the microprotrusion attains a value of about 1300 K for $a = 0.25 \mu\text{m}$ and 3100 K for $a = 0.5 \mu\text{m}$, and then abruptly starts decreasing once the leftover plasma is extinguished (i.e. when $t > \tau$). One can say that the spot was not formed in these two cases. In the case $a = 1 \mu\text{m}$, the maximum temperature of the microprotrusion attains a significantly higher value of about 4700 K at $t \approx 10 \text{ ns}$, however also starts decreasing immediately after. It is legitimate to say that the spot was not ignited in this case either.

Scenario 2 occurs in the cases $a = 3 \mu\text{m}$ and $a = 5 \mu\text{m}$: the temperature of the cathode does not start decreasing immediately after attaining its maximum value

2. Thermal development of an individual cathode spot in a vacuum arc 26

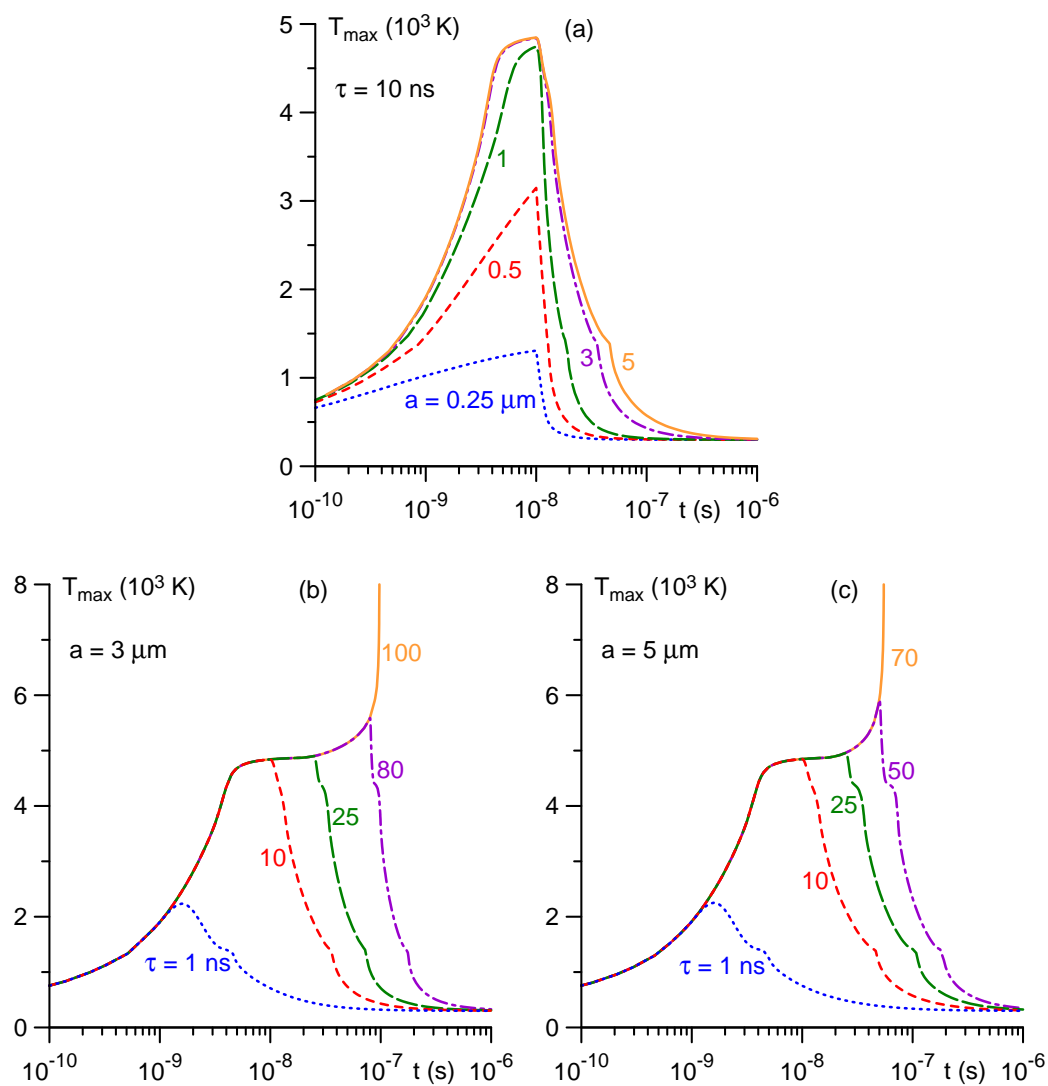


Figure 2.3: Temporal evolution of the maximum temperature in the cathode with the microprotrusion.

2. Thermal development of an individual cathode spot in a vacuum arc 27

(which happens at approximately 5 ns), but rather stays more or less constant around 4700 – 4800 K for some time. It is legitimate to say that the spot was ignited and the ignition time is $t_{ig} \approx 5$ ns. The similarity of the temporal evolution of T_{\max} in these two cases is understandable since the spatial extension of the leftover plasma cloud exceeds the protrusion radius r_{prot} in both cases. In all the cases, T_{\max} for $t \gtrsim 100$ ns is close to 300 K: the energy supplied by the leftover plasma cloud has been removed by thermal conduction into the bulk of the cathode.

The cases $a = 3 \mu\text{m}$ and $a = 5 \mu\text{m}$ for τ exceeding 10 ns should be studied in order to identify conditions where T_{\max} reaches the critical temperature of copper, which is 8390 K, i.e., thermal explosion (thermal runaway) occurs. The corresponding plots are shown in figures 2.3b and 2.3c. Results for $\tau = 1$ ns are also shown for comparison. The above-described scenario 1 occurs for $\tau = 1$ ns: for both cases $a = 3 \mu\text{m}$ (figure 2.3b) and $a = 5 \mu\text{m}$ (figure 2.3c), the temperature of the microprotrusion attains a value of about 2200 K at approximately 1.6 ns and then starts decreasing. The spot was not ignited.

The above-described scenario 2 occurs for $\tau = 10$ ns and $\tau = 25$ ns, for both cases $a = 3 \mu\text{m}$ and $a = 5 \mu\text{m}$: the spot was ignited and subsequently destroyed by heat removal into the bulk of the cathode due to thermal conduction once the leftover plasma cloud has been extinguished.

Two further scenarios are seen in figures 2.3b and 2.3c. Scenario 3 occurs for $\tau = 80$ ns for the case $a = 3 \mu\text{m}$ and for $\tau = 50$ ns for the case $a = 5 \mu\text{m}$: the thermal explosion starts developing, with T_{\max} shifting from the surface into the bulk of the protrusion and reaching 5000 – 6000 K, but then it is quenched by heat conduction once $t > \tau$ and the leftover plasma cloud has been extinguished.

Scenario 4 represents the thermal explosion of the spot. The explosion occurs at $t \approx 97$ ns for the case $a = 3 \mu\text{m}$ and at $t \approx 55$ ns for $a = 5 \mu\text{m}$. Evolution of the cathode temperature distribution for the latter case is shown in figure 2.4.

Let us proceed to modeling results for the planar cathode. For brevity, we skip the analog of figure 2.3a and only note that the minimum value of the cloud dimension needed for ignition of the spot is $a = 3 \mu\text{m}$ and the ignition time is $t_{ig} \approx 8$ ns. The temporal evolution of the maximum temperature T_{\max} in the body of the planar cathode for two values of a and different τ are shown in figure 2.5. The same four scenarios as above may be identified, although the ignition of the spot and its subsequent explosion develop somewhat slower. Scenario 1 occurs for $\tau = 1$ ns in both cases $a = 5 \mu\text{m}$ (figure 2.5a) and $a = 10 \mu\text{m}$ (figure 2.5b): the cathode temperature reaches a maximum of 1500 K at $t \approx 1.5$ ns, and immediately starts decreasing. Scenario 2 (formation of a transient spot eventually destroyed by heat removal into the bulk of the cathode due to thermal conduction) occurs for $\tau = 10$ ns and $\tau = 50$ ns, for both

2. Thermal development of an individual cathode spot in a vacuum arc 28

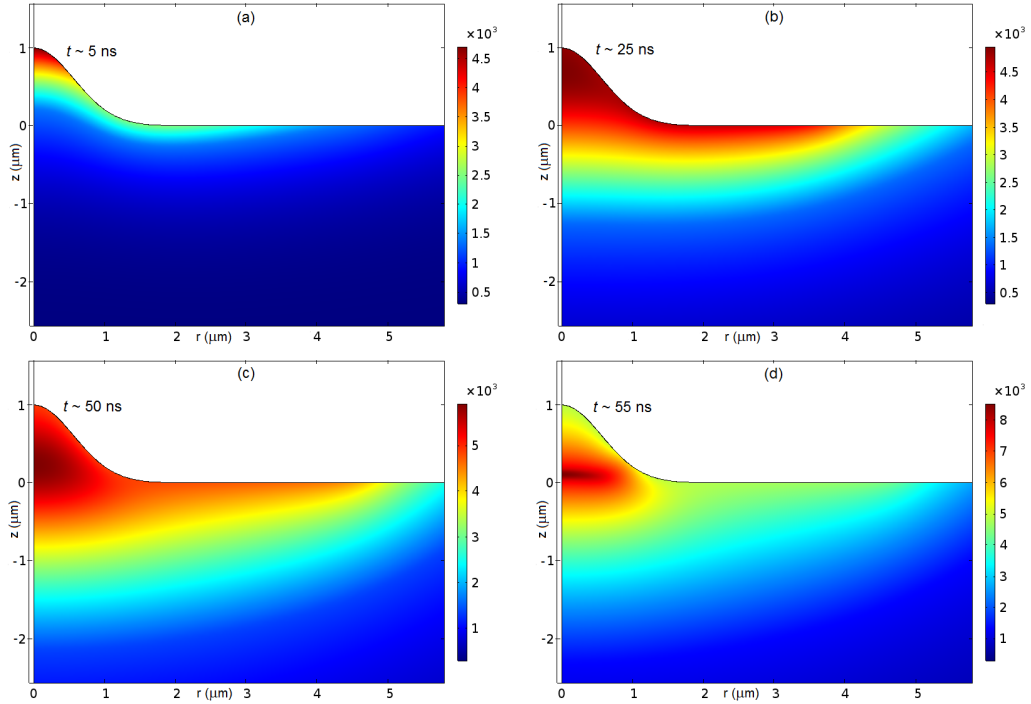


Figure 2.4: Evolution of the temperature distribution in the cathode with the micro-protrusion. $a = 5 \mu\text{m}$, $\tau = 70$ ns. The bar in K.

cases $a = 5 \mu\text{m}$ and $a = 10 \mu\text{m}$, with ignition of the spot at $t_{ig} \approx 8$ ns. Thermal runaway is initiated but then quenched by thermal conduction (scenario 3) for the case $a = 5 \mu\text{m}$ for $\tau = 100$ ns. Lastly, the thermal explosion (scenario 4) occurs at $t \approx 103$ ns for $a = 5 \mu\text{m}$ and at $t \approx 63$ ns for $a = 10 \mu\text{m}$. Similarly to the case of the microprotrusion, the maximum temperature in the spot is more or less constant after the spot has been ignited, until either the extinction of the leftover plasma cloud (scenario 2) or the beginning of thermal runaway (scenarios 3 and 4). Evolution of the cathode temperature distribution for scenario 4 in the case $a = 5 \mu\text{m}$ is shown in figure 2.6.

Thus, in both cases of the cathode with the protrusion and the planar cathode there is a plateau in the temporal evolution of the spot temperature after the ignition and before the plasma cloud has been extinguished or thermal runaway develops, whichever happens earlier. This remarkable feature is known from the modeling of cathode spots in arcs in high-pressure ambient gases [60] and may be understood as follows. As the cathode surface temperature T_w increases with time, so do the different contributions to the density $q_1 = q_1(T_w, U)$ of the energy flux from the plasma produced by ionization of the emitted vapor in the cathode spot. The most relevant contributions to q_1 are the heating by incident ions produced by ionization of the vapor,

2. Thermal development of an individual cathode spot in a vacuum arc 29

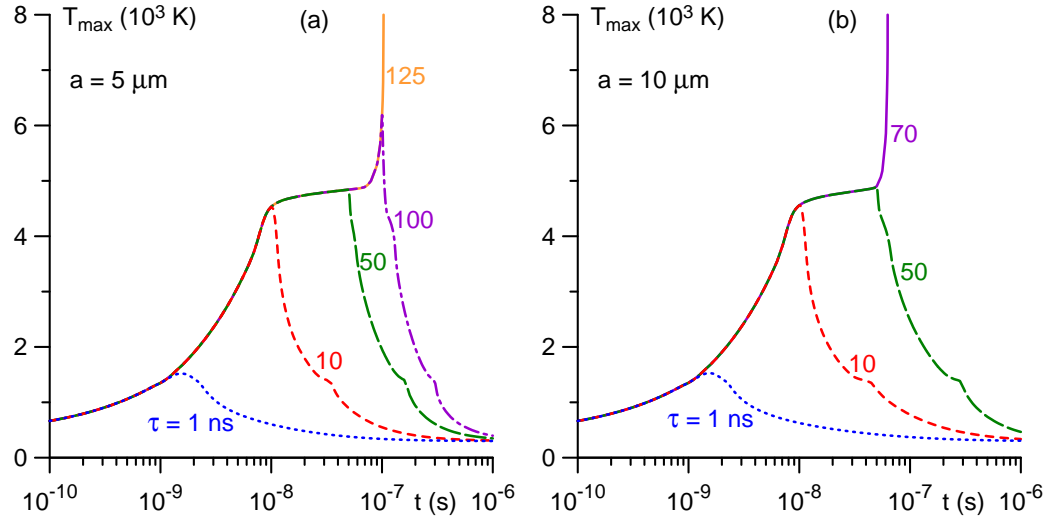


Figure 2.5: Temporal evolution of the maximum temperature in the planar cathode.

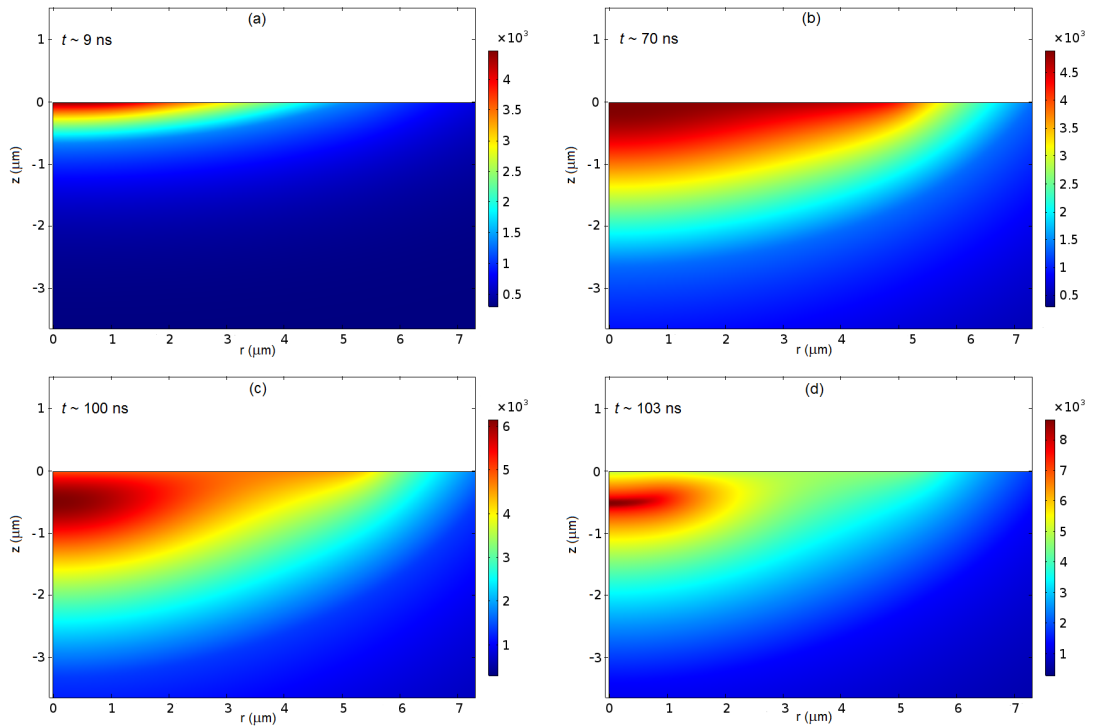


Figure 2.6: Evolution of the temperature distribution in the planar cathode. $a = 5 \mu\text{m}$, $\tau = 125$ ns. The bar in K.

2. Thermal development of an individual cathode spot in a vacuum arc 30

$q_i^{(v)}$, and the cooling by the electron emission, q_{em} . Their dependence on the cathode surface temperature T_w is shown in figure 2.7. Also shown in figure 2.7 is $q_i^{(cl)}$ the heating by the leftover plasma cloud. The combined ion heating, $q_i^{(v)} + q_i^{(cl)}$, exceeds q_{em} for T_w below approximately 4700 K. It is intuitively clear that 4700 – 4800 K represents the upper limit of the cathode temperature until the Joule heating comes into play and thermal runaway starts developing. (In mathematical terms, this is a corollary of the maximum principle for harmonic functions [60].) Note that while $q_i^{(v)}$ is smaller (by approximately a factor of 3) than $q_i^{(cl)}$ at such temperatures, its contribution to the surface heating is nevertheless appreciable.

Since the spot temperature does not change much after ignition and before the plasma cloud has been extinguished or thermal runaway develops, plasma parameters inside the spot, including the current density, also experience little variation. One can say that the "spot brightness" remains approximately constant. On the other hand, the spot significantly expands, as is illustrated by figures 2.4a and 2.4b for the cathode with the protrusion and figures 2.6a and 2.6b for the planar cathode.

The model being used allows one to self-consistently evaluate various spot parameters, including the current I . The temporal evolution of the current during the spot ignition and development is shown for the case $a = 5 \mu\text{m}$ for the cathode with the microprotrusion (figure 2.8a) and for the planar cathode (figure 2.8b). One can identify the moment of ignition of the spot, $t_{ig} \approx 5 \text{ ns}$ for the cathode with the protrusion and $t_{ig} \approx 8 \text{ ns}$ for the planar cathode, as the instant when the current starts increasing from the constant value of current supplied by the leftover plasma cloud (approximately 4.4 A). This coincides with the maximum temperature in the cathode attaining a value around 4700–4800 K; cf. figures 2.3c and 2.5a. However, the plateau visible in the evolution of T_{max} is absent in the evolution of I : the current continually increases from the moment of spot ignition until the explosion or the extinction of the leftover plasma cloud. Since there is little variation in the spot temperature after the spot has been ignited and, therefore, in the current density inside the spot, the rise in current is due to the expansion of the spot over the cathode surface seen in figures 2.4a and 2.4b and figures 2.6a and 2.6b.

It is of interest to consider also parameters of the near-cathode plasma layer inside the spot. Several such parameters evaluated by means of the model [62] are shown in figure 2.9 in the relevant range of the cathode surface temperatures. The saturated vapor pressure p_v , the electric field E_w at the cathode surface, and the current density $j_1 = j_1(T_w, U)$ are shown in figure 2.9a; note that p_v governs the density of flux of vaporized atoms by means of the Langmuir formula: $J_v = p_v / \sqrt{2\pi m_i k T_w}$. Since E_w exceeds 10^9 V/m , the electron emission is not of thermionic nature, in agreement to what was expected. Note that the emission-related electron energy flux is always di-

2. Thermal development of an individual cathode spot in a vacuum arc 31

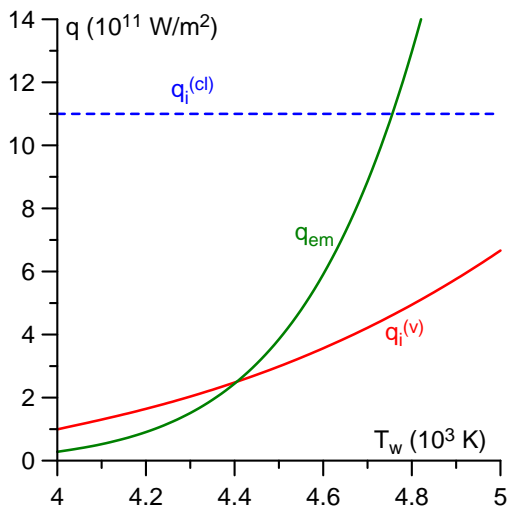


Figure 2.7: q_{em} : energy removed from the cathode surface due to electron emission. $q_i^{(v)}$, $q_i^{(cl)}$: energies delivered to the cathode surface by the ions produced by ionization of the vapor emitted in the spot and by the ions from the leftover plasma cloud, respectively.

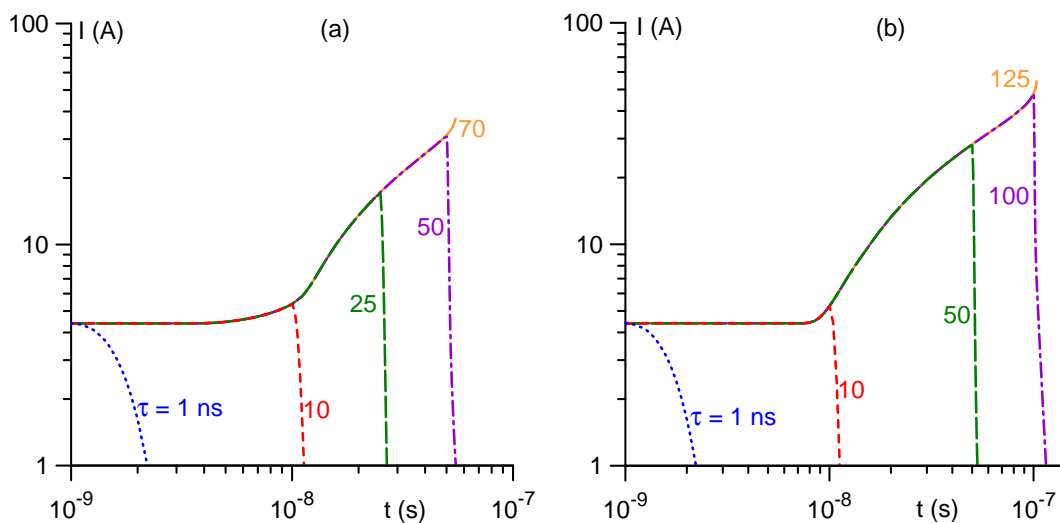


Figure 2.8: Evolution of spot current. $a = 5 \mu\text{m}$. (a) Cathode with the microprotrusion. (b) Planar cathode.

2. Thermal development of an individual cathode spot in a vacuum arc 32

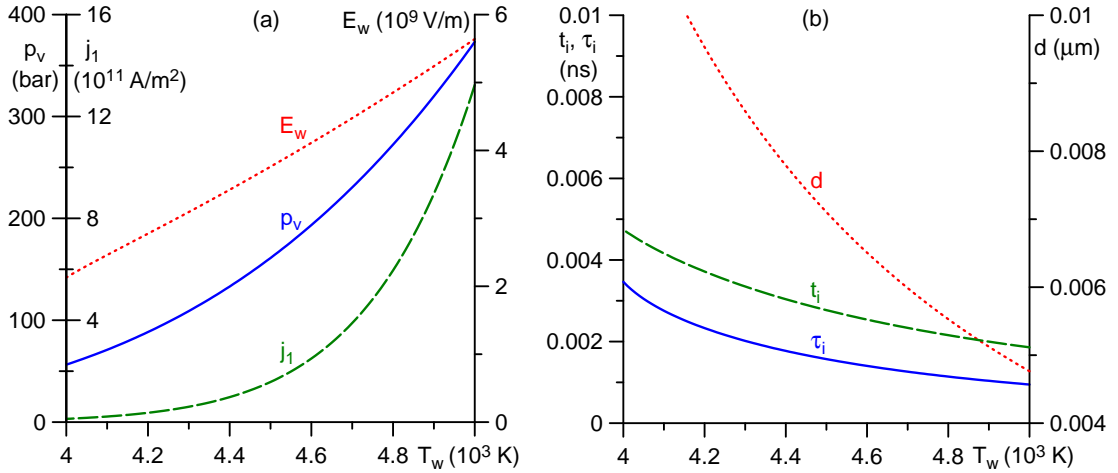


Figure 2.9: Parameters of the near-cathode plasma layer inside the spot. p_v : saturated vapor pressure. j_1 : density of electric current to the cathode surface due to plasma produced from the metal vapor emitted by the spot. E_w : electric field at the cathode surface. t_i : time of flight of the ions across the sheath. τ_i : time scale of ionization of the emitted vapor atoms. d : sheath thickness.

rected into the plasma in the conditions of figure 2.9a, i.e. electron emission contributes to cooling of the cathode.

Other parameters of interest are the sheath thickness d , the time of flight of the ions across the sheath, t_i , and the time scale τ_i of ionization of the emitted vapor atoms. Although the asymptotic sheath theory [61], which is the basis of the code [62] used in this modeling, does not involve any (finite) sheath thickness, representative values of d may be obtained by means of the Child-Langmuir sheath model evaluated in terms of the ion current density and the sheath voltage. The time of flight of the ions across the Child-Langmuir sheath evaluated for copper ions for the sheath voltage of 20 V may be written as $0.39 \frac{d}{\mu\text{m}}$ ns. In the framework of the asymptotic sheath theory [61], the time scale of ionization of the emitted vapor atoms may be estimated as $\tau_i = 1/k_i n_a^{(0)}$, where k_i is the rate constant of ionization by electron impact and $n_a^{(0)}$ is the value of the atomic density at the point of maximum of electrostatic potential. For the purposes of evaluation, this expression may be rewritten as $\tau_i = N_{aw}/k_i n_{aw}$, where n_{aw} is the value of atomic density at the cathode surface evaluated as described in [62] and N_{aw} is given by equation (3) of [62]. The parameters d , t_i , and τ_i evaluated in this way are shown in figure 2.9b.

The assumption of a 1D quasi-stationary near-cathode layer [61, 62] requires that the sheath thickness d be much smaller than the transversal dimensions (the spot radius and dimensions of protrusions) and that τ_i and t_i be much smaller than the characteristic time scales of development of the spot. Given the representative values

2. Thermal development of an individual cathode spot in a vacuum arc 33

shown in figure 2.9b, these requirements are met with a large margin.

2.4 Concluding discussion

The developed model describes the initiation and development of a cathode spot in a high-current vacuum arc, with account of the plasma cloud left over from a previously existing spot or generated at arc triggering, all the mechanisms of current transfer to the cathode surface, and the Joule heat generation in the cathode body.

The account of all the mechanisms of current transfer, including the contributions from both the leftover plasma cloud and the plasma produced by ionization of the metal vapor emitted in the spot, allows one to identify in a natural way the different phases of life of an individual cathode spot: the ignition, the expansion over the cathode surface, and the thermal explosion or destruction by heat removal into the bulk of the cathode due to thermal conduction. The states (*a*) shown in figures 2.4 and 2.6 exemplify the end of the ignition phase; the expansion phase occurs between states (*a*) and (*b*); and states (*b*), (*c*), and (*d*) exemplify the thermal runaway development.

The ignition phase is characterized by a fast increase of the temperature of the cathode surface under the effect of the ions coming from the leftover plasma. In the conditions of figures 2.3c and 2.5a, this phase terminates at approximately 5 or 8 ns, respectively. In figure 2.8, this phase is associated with the horizontal section of the dependence $I(t)$.

After the spot has been ignited, the maximum temperature of the cathode, which occurs at the surface, does not change much and is approximately 4700–4800 K. This is the surface temperature at which the heating of the cathode surface, which is due to bombardment by the ions originating in the leftover plasma cloud and by the ions produced in the ionization of atoms vaporized from the surface, is balanced by the cooling of the cathode surface, which is due to electron emission. This remarkable feature is known from the modeling of cathode spots in arcs in high-pressure ambient gases and manifests itself as the plateau in the dependence $T_{\max}(t)$ seen in figures 2.3b, 2.3c, and 2.5. One can say that the spot brightness does not change much during this phase. However, this does not mean that the spot has reached a steady-state: the spot expands over the cathode surface, so the spot current increases.

Eventually, the maximum of the cathode temperature is shifted from the surface into the cathode: the Joule heating comes into play and thermal runaway starts developing below the cathode surface, leading to an explosion (thermal runaway). The explosion can occur not only on a cathode with a microprotrusion, but on a planar cathode as well.

The development of the spot is interrupted if the leftover plasma cloud has been

2. Thermal development of an individual cathode spot in a vacuum arc 34

extinguished: the spot is destroyed by heat removal into the bulk of the cathode due to thermal conduction. Therefore, different scenarios are possible depending on the time of action of the cloud: the spot may be quenched either before having been formed, or during the expansion phase, or even at the initial stage of thermal explosion. It should be stressed that parameters of the plasma cloud required for the ignition, and eventual explosion, of the spot on the cathode with a $1\ \mu\text{m}$ -scale microprotrusion and on the planar cathode are of the same order of magnitude. Indeed, the minimum spatial extension and the time of action of the leftover plasma cloud needed for the spot to be ignited are $a = 3\ \mu\text{m}$, $t_{ig} = 5\ \text{ns}$ for the cathode with the microprotrusion and $a = 3\ \mu\text{m}$, $t_{ig} = 8\ \text{ns}$ for the planar cathode; the time of action needed for the explosion for $a = 5\ \mu\text{m}$ is $55\ \text{ns}$ for the cathode with the microprotrusion and $103\ \text{ns}$ for the planar cathode. Also of the same order are the total energies that need to be deposited by the leftover plasma cloud for the spot to be ignited and eventually explode, $Q = \pi a^2 q_i^{(cl)} t$; for example, the energy required for ignition (with $a = 3\ \mu\text{m}$) is $0.16\ \mu\text{J}$ for the cathode with the microprotrusion and $0.25\ \mu\text{J}$ for the planar cathode.

In all the cases where the spot is ignited, it either explodes or is destroyed by thermal conduction; a steady state is never reached. This is consistent with results of investigation of stability of stationary cathode spots of vacuum arcs [102]: the spots operating at a fixed value of the near-cathode voltage are unstable.

Results of simulations with account of motion of the molten metal, convective heat transfer, and surface deformation are reported in chapter 3. An important question is if parameters of the near-cathode plasma remaining after the spot extinction are sufficient to initiate a new spot. Relevant estimates are given in chapter 3.

Chapter 3

Detailed numerical simulation of cathode spots in vacuum arcs: Interplay of different mechanisms and ejection of droplets

3.1 Introduction

In chapter 2, the thermal development of the spot under the effect of the bombardment of the cathode surface by ions coming from the leftover plasma cloud, vaporization of the cathode material in the spot, its subsequent ionization and the interaction of the produced plasma with the cathode, and Joule heating in the cathode body was studied. Several phases of life of an individual cathode spot were identified: the ignition, the expansion over the cathode surface, and the thermal runaway (microexplosion) or destruction of the spot by heat removal into the bulk of the cathode due to thermal conduction. It was shown that electron emission significantly affects the development of the spot, in particular, limiting the cathode surface temperature during the expansion phase and preventing thermal runaway development until the Joule heating becomes appreciable.

The aim of this chapter is to study the ignition and development of cathode spots of vacuum arcs with account of all the above mechanisms, together with the hydrodynamic aspects of the problem: melting of the cathode and motion of the molten metal under the effect of the plasma pressure and the Lorentz force, the change in shape of the molten cathode surface the formation of craters and liquid-metal jets, and the detachment of droplets. To this end, the model of chapter 2 is supplemented with an

account of the motion of the molten metal and related phenomena: deformation of the molten surface, surface tension effects, and convective heat transfer. Several features of the development of the cathode spot reported in chapter 2 remain present in the framework of the more detailed physical picture given here: the ignition and expansion phases remain clearly identifiable; the plateau in the maximum cathode temperature evolution during the expansion phase remains present; the destruction of the spot by heat removal into the bulk of the cathode due to thermal conduction (accompanied by solidification of the molten metal) occurs after the leftover plasma cloud has been extinguished. The motion of the molten metal comes into play on a time scale longer than the spot ignition times, which is why the results presented in chapter 2 on the spot ignition time and the initial stage of the expansion phase remain applicable. On the other hand, no thermal explosion occurs: the development of the spot results in the formation of a crater and a molten metal jet, and the ejection of a droplet.

The outline of this chapter is as follows. The numerical model is introduced in section 3.2. Results of simulation are reported and discussed in section 3.3. Conclusions are summarized in section 3.4.

3.2 The model

3.2.1 Equations and boundary conditions

The model comprises the time-dependent heat conduction equation, describing heat transfer in the cathode body (including both the melt and the solid part); the equation of current continuity in the cathode body, supplemented with Ohm's law; and the continuity and Navier-Stokes equations, written in the incompressible form and describing the motion of the melt:

$$\rho c_p \frac{\partial T}{\partial t} + \rho c_p \mathbf{u} \cdot \nabla T = \nabla \cdot (\kappa \nabla T) + \sigma (\nabla \varphi)^2, \quad (3.1)$$

$$\nabla \cdot \mathbf{j} = 0, \quad (3.2)$$

$$\nabla \cdot \mathbf{u} = 0, \quad (3.3)$$

$$\rho \frac{\partial \mathbf{u}}{\partial t} + \rho (\mathbf{u} \cdot \nabla) \mathbf{u} = \nabla \cdot [-p \mathbf{I} + \mu (\nabla \mathbf{u} + (\nabla \mathbf{u})^T)] + \mathbf{j} \times \mathbf{B}. \quad (3.4)$$

Here ρ is the the mass density of the metal, c_p , κ , σ and μ are, respectively, the specific heat, the thermal and electrical conductivities of the metal, and the viscosity of the melt (known functions of the temperature T), φ is the electric potential, \mathbf{u} is the velocity, p is the pressure, \mathbf{I} is the identity tensor, $\mathbf{j} = -\sigma \nabla \varphi$ is the density of electric current in the cathode body, and \mathbf{B} is the magnetic field. The second term on the lhs of equation (3.1) describes the convective heat transfer in the molten part of the

cathode (an effect not taken into account in the model of chapter 2); in the solid part this term vanishes. The last term on the rhs of equation (3.4) represents the Lorentz force.

The equations are solved under the assumption of axial symmetry in cylindrical coordinates (r, z) . Only self-induced magnetic field is taken into account, so \mathbf{B} has only the azimuthal component which is related to the axial component of the current density \mathbf{j} in the cathode body by Ampère's law. The calculation domain for equations (3.1) and (3.2) is the whole of the cathode, including both the melt and the solid part. The boundary conditions for these equations are the same as those given in section 2.2 for the model of chapter 2. In particular, the boundary conditions on the cathode surface are

$$\kappa \mathbf{n} \cdot \nabla T = q_1 + q_2, \quad \sigma \mathbf{n} \cdot \nabla \varphi = j_1 + j_2, \quad (3.5)$$

where \mathbf{n} is the unit vector normal to the cathode surface and directed outward, q_1 and j_1 are contributions to the densities of energy flux and electric current from the plasma to the cathode surface due to the vapor emitted in the spot, ions and electrons produced by ionization of the vapor, and the electron emission from the cathode surface, and q_2 and j_2 are densities of energy flux and electric current transported by the ions from the leftover plasma cloud.

The calculation domain for equations (3.3) and (3.4) is the molten part of the cathode. The boundary condition at the cathode surface is

$$[-p\mathbf{I} + \mu(\nabla \mathbf{u} + (\nabla \mathbf{u})^T)] \cdot \mathbf{n} = -p_{pl}\mathbf{n} + \mathbf{F}_{st}, \quad (3.6)$$

where p_{pl} is the pressure exerted over the cathode surface by the plasma (see subsection 3.2.3 below) and \mathbf{F}_{st} is the surface tension force evaluated in the usual way in terms of the curvature of the molten cathode surface and the surface tension coefficient of the cathode material. The velocity \mathbf{u} vanishes at the interface between the molten and solid metal.

3.2.2 Material functions

Simulation results reported in this chapter refer to cathodes made of copper, with a Gaussian-shaped microprotrusion as in chapter 2 and planar. The (temperature-dependent) mass density, specific heat, and thermal and electrical conductivities of copper are specified as in section 2.2.2. The account of the latent heat of melting is introduced along the same lines as is done in simulation of metal casting [114].

Data on the temperature-dependent viscosity μ of liquid copper was taken from the experimental work [115]. The data reported and the fit function proposed in [115]

are shown in figure 3.1a. Also shown in figure 3.1a are the data given by the fit formula used in this work (μ in Pa s, T in K),

$$\mu = \frac{1}{2} \left(1 - \tanh \frac{T-1358}{\delta_3} \right) \mu_1 + \frac{1}{4} \left(1 + \tanh \frac{T-1358}{\delta_3} \right) \left(1 - \tanh \frac{T-1950}{\delta_3} \right) \mu_2 + \frac{1}{2} \left(1 + \tanh \frac{T-1950}{\delta_3} \right) \mu_3, \quad (3.7)$$

where

$$\begin{aligned} \mu_1 &= 4.03 \times 10^{-3}, \\ \log_{10} (\mu_2 / \mu_{\text{const}}) &= -0.422 + \frac{1393.4}{T}, \\ \mu_3 &= 1.96 \times 10^{-3}, \end{aligned}$$

and $\mu_{\text{const}} = 10^{-3}$ Pa s and $\delta_3 = 10$ is a smoothing parameter.

Data on the temperature-dependent surface tension coefficient σ_{st} of liquid copper can be found in a number of experimental works, however the reported values are rather scattered when compared and are also dependent on the method utilized for the measurements; figure 3.1b. The most recent experimental data can be found in the work [121]. The proposed formula in [121] was adapted into the fit formula used in this work (σ_{st} in N/m, T in K),

$$\sigma_{\text{st}} = \frac{1}{2} \left(1 - \tanh \frac{T-1287}{\delta_3} \right) \sigma_{\text{st},1} + \frac{1}{4} \left(1 + \tanh \frac{T-1287}{\delta_3} \right) \left(1 - \tanh \frac{T-2000}{\delta_3} \right) \sigma_{\text{st},2} + \frac{1}{2} \left(1 + \tanh \frac{T-2000}{\delta_3} \right) \sigma_{\text{st},3}, \quad (3.8)$$

where

$$\begin{aligned} \sigma_{\text{st},1} &= 1.2708, \\ \sigma_{\text{st},2} &= 1.257 - 0.2 \times 10^{-3} (T - 1356), \\ \sigma_{\text{st},3} &= 1.1286. \end{aligned}$$

Quantities q_1 , q_2 , j_1 , and j_2 in equation (3.5) are evaluated in the same way as in section 2.2 for the model of chapter 2. The near-cathode voltage drop U is set equal to 20 V, which corresponds to initiation of spots under conditions of high-current vacuum arcs typical, e.g., for high-power circuit breakers. The parameters τ and a in equation (2.5) for quantities q_2 and j_2 were set equal to 25 ns and $5 \mu\text{m}$, respectively, unless indicated otherwise. (These values have been chosen on the basis of experimental data on the lifetime of an individual spot on copper cathodes [25, 35, 66], and on the spatial extension of the plasma cloud produced by a spot [33, 125]. The effect of the variation of these parameters on the spot ignition was studied chapter 2.) The characteristic time τ_0 was set equal to 1 ns.

3.2.3 Plasma pressure acting on the cathode surface

The plasma pressure p_{pl} acting on the cathode surface comprises contributions of the plasma produced from the metal vapor emitted in the spot and of the leftover plasma

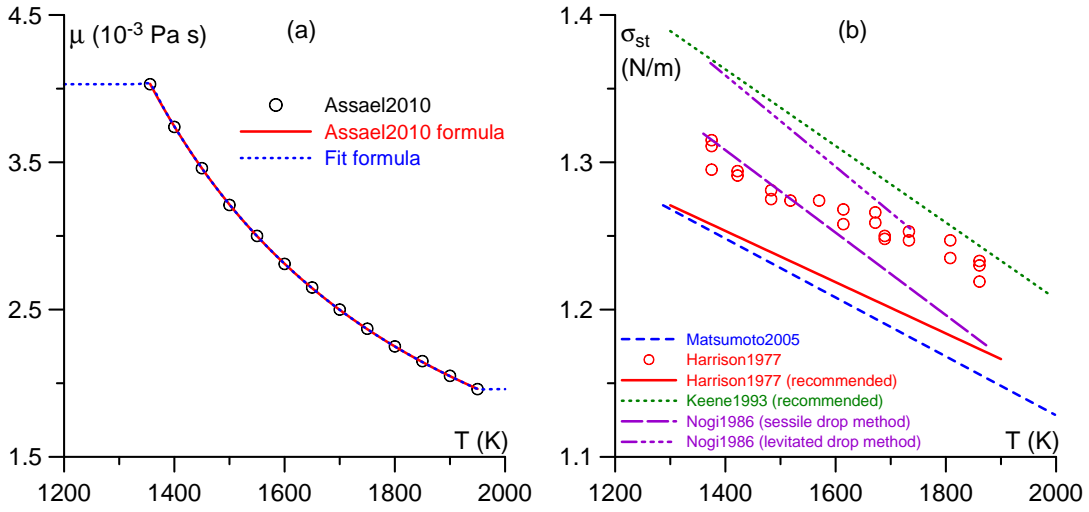


Figure 3.1: (a) Viscosity of liquid copper; points: data according to [115]; solid line: fit formula according to [115]; dotted line: fit formula used in this work. (b) Surface tension coefficient of liquid copper; data is shown according to [121–124].

cloud, evaluated independently of each other: $p_{pl} = p_1 + p_2$. As for quantities q and j (defined in section 2.2), this simple superposition neglects a nonlinear interaction between the leftover plasma and the freshly-produced vapor from the spot.

The contribution $p_1 = p_1(T_w, U)$ is computed as a function of the local cathode surface temperature T_w and the near-cathode voltage drop U by means of the model of near-cathode space-charge sheaths in vacuum arcs [61], based on a self-consistent description of ionization of evaporated atoms in the sheath and of a maximum of potential occurring inside the sheath. The sheath thickness is much smaller than the scale of ion-atom collisions (cf. figure 2.9b of section 2.3), hence the total energy of an ion is conserved. The velocity of ions generated at a point z when they have reached a point x will be (designations used in this section are the same as those in [61])

$$v_i(x, z) = \pm \sqrt{\frac{2e}{m_i} [\varphi(z) - \varphi(x)]}. \quad (3.9)$$

The ions generated in the region $x < 0$ (i.e., between the cathode and the point of the maximum of potential) move back to the cathode. The ions generated in the region $x > 0$ move into the plasma. We are interested in the ions moving back to the cathode, hence equation (3.9) should be applied for $x < z < 0$ with the sign minus.

The number of ions generated in the layer $z \leq x \leq z + dz$ per unit time and unit area (i.e., the density of ion flux generated in this layer) is $w(z) dz$. When these ions have reached a point x positioned between the point z and the cathode, their speed is $|v_i(x, z)|$ and the density of flux of momentum transported by these ions

in the direction to the cathode is $-w(z) dz m_i v_i(x, z)$. The total density of flux of momentum of ions in the direction to the cathode at a point x is

$$p_1(x) = -m_i \int_x^0 w(z) v_i(x, z) dz. \quad (3.10)$$

Equation (14) of [61] in dimensional variables reads

$$\frac{\varepsilon_0}{2n_e^{(0)}kT_e} \left(\frac{d\varphi}{dx} \right)^2 = e^\Phi - 1 - \frac{\sqrt{2m_i e k_i}}{n_e^{(0)}kT_e} \int_0^x n_e(z) n_a(z) \sqrt{\varphi(z) - \varphi(x)} dz. \quad (3.11)$$

Taking into account equations (3.9), (3.10) and the equality $w = k_i n_e n_a$, equation (3.11) may be rewritten as

$$p_1(x) = \frac{\varepsilon_0}{2} \left(\frac{d\varphi}{dx} \right)^2 + n_e^{(0)}kT_e (1 - e^\Phi). \quad (3.12)$$

Here $\Phi = \frac{e\varphi}{kT_e} - \frac{e\varphi^{(0)}}{kT_e}$ as in [61]. Thus, the ion pressure is expressed in terms of the local electric field and potential and of parameters at the point of maximum of potential (values of potential $\varphi^{(0)}$ and electron density $n_e^{(0)}$). Since all the ions are absorbed by the cathode surface in the framework of the model considered, the pressure exerted on the cathode by the ions equals the flux of momentum of the incident ions and may be evaluated by means of equation (3.12) applied at the cathode surface.

Note that equation (3.12) has a clear physical meaning, which is revealed by rewriting this equation in the form

$$p_1(x) + n_e kT_e - n_e^{(0)}kT_e = \frac{\varepsilon_0}{2} \left(\frac{d\varphi}{dx} \right)^2. \quad (3.13)$$

The lhs of this equation represents the pressure difference to which the plasma layer between the point x and the potential maximum is subjected, while the rhs represents the integral (electrostatic) force acting on this layer, evaluated with the use of the Poisson equation.

Expression (3.12) at the cathode surface is evaluated by means of the same Fortran code which is used for evaluation of q_1 and j_1 ; the term e^Φ in equation (3.12) is exponentially small at the cathode surface and is neglected.

The contribution of the leftover plasma cloud is written as

$$p_2 = p_i^{(cl)} f_r(r) f_t(t), \quad p_i^{(cl)} = \frac{2 q_i^{(cl)}}{\sqrt{2eU/m_i}}.$$

Note that the quantity $\sqrt{2eU/m_i}$ has the meaning of speed of the ions impinging on the cathode surface estimated neglecting the kinetic energy of the ions at the sheath edge.

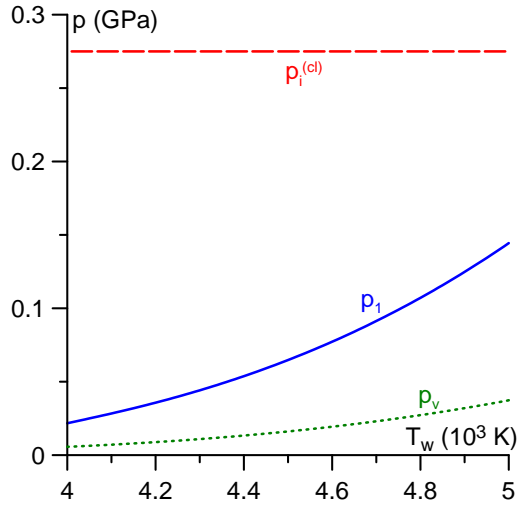


Figure 3.2: p_1 : the pressure exerted by incident ions produced by the ionization of the metal vapor emitted in the spot as function of the cathode surface temperature T_w . $p_i^{(cl)}$: pressure due to incident ions originating from the leftover plasma cloud. p_v : saturated vapor pressure.

As an example, the data on p_1 in the range of temperatures relevant to the simulations of this work and the value of $p_i^{(cl)}$ are shown in figure 3.2. One can see that $p_i^{(cl)}$ exceeds p_1 by at least a factor of 2; however, p_1 is important and should not be neglected as will be shown below.

Also shown in figure 3.2 is the saturated vapor pressure p_v . One can see that p_v is significantly smaller than p_1 and $p_i^{(cl)}$. Furthermore, p_v is significantly smaller than the pressure inside the metal, which is close to $p_{pl} = p_1 + p_2$. It follows that, independently of the presence or absence of the leftover plasma cloud, the pressure inside the molten metal is sufficient to prevent a transition into the gaseous state; bubbles do not appear (i.e., no boiling occurs).

3.2.4 Numerical Implementation

Different methods are available to account for a solid to liquid phase change in numerical simulations. They are largely divided into two main categories: front-tracking methods and fixed-grid methods [114, 126]. Front-tracking methods consist of two domains, one liquid and one solid, with a different set of equations solved in each domain. The solid-liquid interface is modeled as a boundary between the two domains, with a boundary condition accounting for heat transfer between phases; this is the well-known classical Stefan problem. A moving grid that distorts with time is required to track the shape and position of the interface. However, due to this deformation of the grid, this type of method is not suitable for problems that involve highly

distorted interfaces, or mergers or break-ups. On the other hand, fixed-grid methods (more commonly known as enthalpy methods) consider only one computational domain where both phases are present, and solve only one set of equations. There is no explicit tracking of the interface. Latent heat transfer and zero velocities in the solid are introduced through the inclusion of appropriate source terms in the heat and Navier-Stokes equations [114, 126].

The implementation of both types of methods was tested during the development of the model of cathode spots in vacuum arcs. The enthalpy-porosity method [127, 128] was chosen for modeling the solid-liquid phase transition in the cathode body, as such an approach is particularly relevant when the phase change is only a part of a more complex problem to be solved; it allows the solution of the phase change problem on a fixed grid, making the model as a whole more numerically tractable. Enthalpy methods more commonly account for the latent heat in the system by adding an appropriate source term to the energy equation written in terms of enthalpy [114, 126–128]. However, when the energy equation is written in terms of temperature, the latent heat can be accounted for through the effective specific heat method [114], as in equation (2.9).

The enthalpy-porosity method treats the entire calculation domain as a liquid, and the major problem encountered is ensuring zero velocities in the solid region. In broad terms, this approach consists in treating the phase change as a problem of flow in porous media, governed by Darcy’s law [128]. Three distinct regions are present in such a problem: a fully solid region, a totally liquid region and a mushy region consisting of liquid dispersed among solid. It can be assumed that the medium undergoing a change of phase behaves as a porous medium with porosity defined as

$$f_{\text{LF}}(T) = \begin{cases} 1, & T > T_m + \Delta T \\ \frac{T - T_m + \Delta T}{2\Delta T}, & T_m - \Delta T \leq T \leq T_m + \Delta T \\ 0, & T < T_m - \Delta T \end{cases} . \quad (3.14)$$

Equation (3.14) represents the fraction of liquid present in different regions of the calculation domain; $T_m = 1358 \text{ K}$ is the melting temperature of copper; ΔT defines the temperature range over which the phase transition occurs, thus defining the width of the mushy zone.

An appropriate source term may be derived [127–129] for the Navier-Stokes equation in the form of a volume force:

$$\mathbf{F}_{\text{pc}} = -\frac{(1 - f_{\text{LF}})^2}{f_{\text{LF}}^3 + \varepsilon_{\text{pc}}} A_{\text{pc}} \mathbf{u}, \quad (3.15)$$

with a small number ε_{pc} added to f_{LF}^3 in the denominator in order to avoid overflow caused by division by zero in the solid phase.

This source term affects the phase change calculations in the following way: in the liquid region, the source term is zero, $\mathbf{F}_{\text{pc}} = 0$, and the momentum equations are reduced to the conventional Navier-Stokes equations. In the mushy region the value of \mathbf{F}_{pc} increases such that it begins to dominate over the other terms of the equations, and in the solid phase the large value of \mathbf{F}_{pc} will swamp out all terms of the equations, thus effectively forcing the velocities to vanish [128].

The value of the constant A_{pc} depends on the morphology of the porous media, controlling the degree of penetration of the convection field into the mushy region. In the limiting case where the function $f_{\text{LF}}(T) = 0$ (solid phase), the value given by the ratio of the constants, $\mathbf{F}_{\text{pc}} = -\frac{A_{\text{pc}}}{\varepsilon_{\text{pc}}}\mathbf{u}$, has to be large enough for \mathbf{F}_{pc} to dominate over all the other terms in the Navier-Stokes equation.

Expression (3.15) was included in the Navier-Stokes equations (3.4), with the constants set equal to $A_{\text{pc}} = 10^{14}$ and $\varepsilon_{\text{pc}} = 10^{-2}$.

The level-set method [130–132] is implemented for tracking the deformation of the molten cathode surface. The method was developed to model moving interfaces on fixed Eulerian grids (similarly to how the melting front is described in the framework of the enthalpy-porosity method). It is particularly useful for two-phase flow problems in which the topology of the evolving interface changes with time (e.g., break-up of a jet or droplet detachment). The method relies on an implicit representation of the interface between two fluids by means of an auxiliary function, the so-called level-set function ϕ . This function is defined as a signed-distance function, representing the distance from any point in the calculation domain to the initial interface position at time $t = 0$ [133]. The main drawback of the originally proposed level-set method is that it is not conservative, i.e., during modeling, loss or gain of mass can occur, which is physically incorrect [131]. Several approaches have since been suggested to improve mass conservation in the level-set method, the most relevant for this work being the conservative level-set method [131, 132], which is the basis of the level-set method available in COMSOL Multiphysics (a special module is available for modeling two-phase flows with this method).

The equation that governs the level-set function and thus the position of the interface is written as

$$\frac{\partial \phi}{\partial t} + \mathbf{u} \cdot \nabla \phi = \gamma_{ls} \nabla \cdot \left(\varepsilon_{ls} \nabla \phi - \phi (1 - \phi) \frac{\nabla \phi}{|\nabla \phi|} \right). \quad (3.16)$$

The lhs of equation (3.16) controls the advection of the interface, while the rhs controls the numerical stability of the solution [131, 132]. The parameter ε_{ls} determines the thickness of the interface. As the interface evolves in time it may change shape, which can cause numerical problems. To keep the profile and width of the interface constant, reinitialization is necessary [133]; the parameter γ_{ls} controls the amount of

reinitialization (stabilization) of the level-set function, and needs to be tuned for each specific problem. If γ_{ls} is too small, the thickness of the interface may not remain constant and this leads to numerical instabilities which will cause oscillations in ϕ ; if γ_{ls} is too large the interface will be advected incorrectly. A suitable value for γ_{ls} is the maximum magnitude of the velocity field in the calculation domain.

In the framework of the level-set method, the Navier-Stokes equations are written in a slightly different form, to account for surface tension effects explicitly. Surface tension effects are handled through the continuous surface force model, developed in [134], which redefines the surface force as a volume force spread over the finite interface width ε_{ls} . This force is expressed as

$$\mathbf{F}_{st} = \sigma_{st} \kappa_c \delta(\phi) \hat{\mathbf{n}}, \quad (3.17)$$

where $\hat{\mathbf{n}}$ is the unit normal vector of the interface, and $\delta(\phi)$ is the Dirac delta function dependent on ϕ , localized on the interface and that restricts the influence of the body force to the interface only.

One must also consider two "fluids": the whole of the (copper Cu) cathode body, and a medium beyond the cathode (which will be termed "gas phase"). There is no explicit separation (i.e., an interface) between the "cathode phase" and the "gas phase", i.e., the same set of equations is solved in both fluids. The material parameters are redefined as global parameters, dependent on the level-set function ϕ and on the relevant parameter of each individual fluid. For example, the mass density ρ takes the form

$$\rho = \rho_{Cu}(T) + (\rho_{gas} - \rho_{Cu}(T)) \phi,$$

and so do the remaining material parameters (specific heat c_p , thermal and electrical conductivities κ and σ , and viscosity μ).

It should be stressed that the "gas phase" is merely a numerical construct required for the use of the level-set method, i.e., its addition to the model should not affect the spot ignition and development on the cathode surface, nor influence the evolution of the molten surface. To ensure this, the material parameters of the "gas" were chosen so as to not impede the motion of the molten metal or the deformation of the molten surface, and so that the flow of energy and current from the plasma are directed onto the cathode (and not into the "gas phase"). Furthermore, a velocity damping term (i.e., a stabilization term) is necessary in the "gas phase" so as to minimize spurious oscillations due to numerical instabilities during simulation.

Appropriate values for parameters ε_{ls} and γ_{ls} were determined by means of a simplified model similar to the model [53]; cf. subsection 3.2.5.

The problem is solved numerically by means of the commercial software COMSOL Multiphysics, which offers the option of modeling compressible ($\rho = \rho(p, T)$), weakly

compressible ($\rho = \rho(T)$), or incompressible flows ($\rho = \text{const}$). It follows from the analysis in Appendix A that the most accurate formulation for the continuity and Navier-Stokes equations in the modeling of this work would be the weakly compressible one. However, an attempt to use the weakly compressible form, which is supposedly compatible with the level-set method used to track the deformation of the molten surface, proved unsuccessful. Such an issue requires further extensive investigation, which was not carried out in this work. Instead, the incompressible formulation of the continuity and Navier-Stokes equations is used (equations (3.3) and (3.4)); the temperature dependence of the mass density described in subsection 2.2.2 is used in the heat and Navier-Stokes equations, without account of the temporal and spatial derivatives of ρ in the continuity equation.

Note that a similar physical problem for plasma-anode interaction in vacuum arcs has been solved in works [135–138] by means of the software FLUENT. The enthalpy-porosity method was used for the modeling of the solid-liquid phase transition in the anode body, although the approach differs from the one used in this work: the energy conservation equation is solved in terms of the enthalpy instead of the temperature. In [138], the anode surface deformation is simulated by means of the volume-of-fluid method, which is an alternative to the level-set method used in this work.

3.2.5 Validation of the model

In order to validate the hydrodynamics part of the model, a simplified version was built similar to the model [53]: the account of current transfer to the cathode was discarded, the contributions of the plasma produced in the spot were neglected. The simulation reproduces results of [53] with only minor discrepancies (figure 3.3), which can be attributed to differences in the chosen temperature dependencies of the material properties of copper and the distinct numerical methods employed.

Furthermore, so as to accurately reproduce the development of the liquid metal jet with the simplified model, the appropriate values for the interface width ε_{ls} and stabilization parameter γ_{ls} were found to be 10 nm and 200 m/s, respectively. Otherwise, the interface is too wide to properly resolve the head of the jet, and the numerical stabilization of equation (3.16) is insufficient for a successful simulation. The same values of ε_{ls} and γ_{ls} are used in the above-described model.

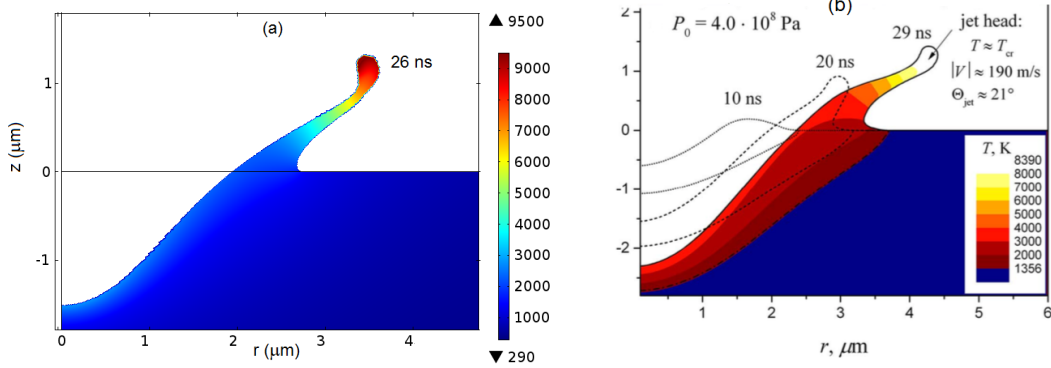


Figure 3.3: Jet formation computed with the simplified model. (a) Temperature distribution computed with the simplified model. The bar in K. (b) Temperature distribution reported in [53]. (a), (b) The results shown were computed for the same conditions of incident plasma pressure and heat flux.

3.3 Numerical results and discussion

3.3.1 Results

Let us consider the results obtained by simulations in the framework of the (full) model described in section 3.2 and accounting for all the previously mentioned cathode spot mechanisms, in particular, the effects of the motion of the molten metal and of the plasma production by ionization of vapor emitted in the spot. The temporal evolution of the temperature distribution in the cathode and of the cathode surface deformation is shown in figure 3.4 for the cathode with the microprotrusion and in figure 3.5 for the planar cathode. The temporal evolution of the maximum cathode temperature T_{max} and of the spot current I is shown in figures 3.6 and 3.7 by the lines marked by "HD&V".

The temporal evolution in the cases of the cathode with the microprotrusion and of the planar cathode occurs in essentially the same way. At first, the maximum temperature of the cathode rapidly increases; figure 3.6. At 5 ns for the cathode with the microprotrusion and at 8 ns for the planar cathode (figures 3.4a and 3.5a), T_{max} has reached a value of approximately 4700 – 4800 K and changes little from then on until the leftover plasma cloud has been extinguished (at $t = 25$ ns) and the temperature starts falling. In the case of the cathode with the microprotrusion, the protrusion starts melting around 3 ns and is completely destroyed within 14 ns. In both cases, a crater of approximately $1 \mu\text{m}$ in depth and $5 \mu\text{m}$ in radius has been formed by the time of extinction of the leftover plasma cloud; figures 3.4b and 3.5b. An axially symmetric jet develops at the crater periphery (figures 3.4c and 3.5c), followed by the detachment of the jet head (figures 3.4d and 3.4e, and 3.5d and 3.5e). The explosion

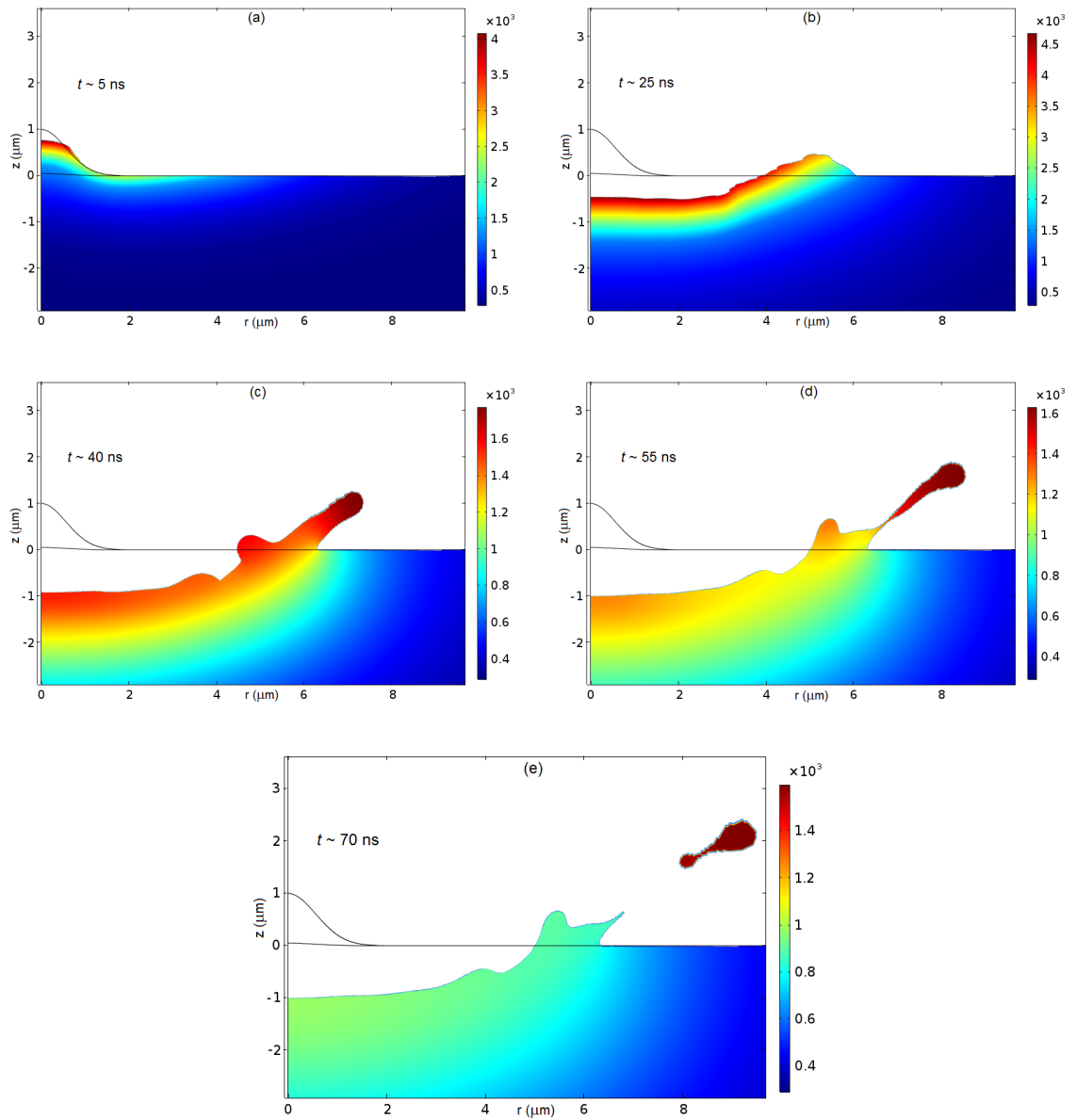


Figure 3.4: Evolution of the temperature distribution and cathode surface deformation. Cathode with the microprotrusion. The bar in K.

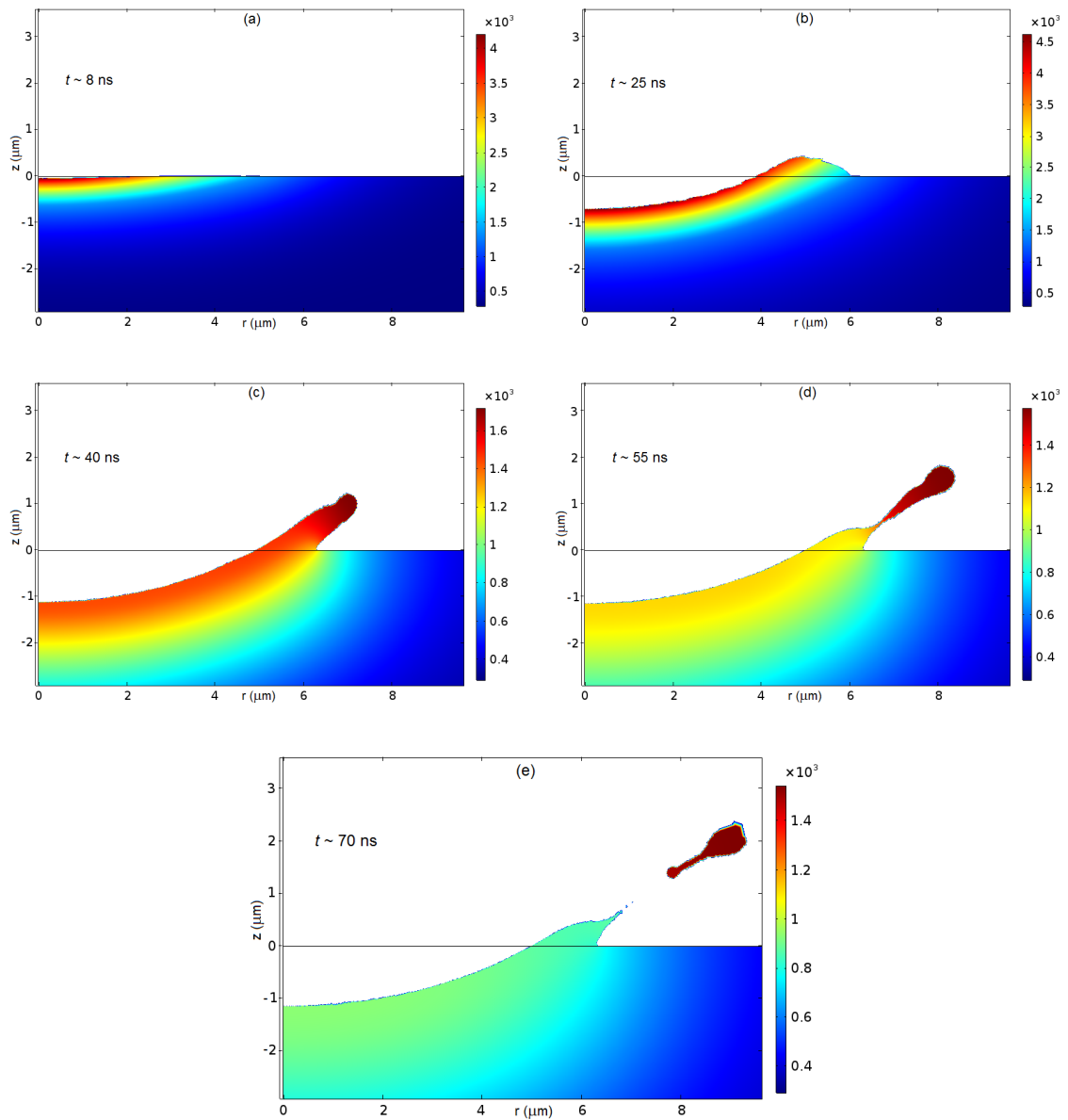


Figure 3.5: Evolution of the temperature distribution and cathode surface deformation. Planar cathode. The bar in K.

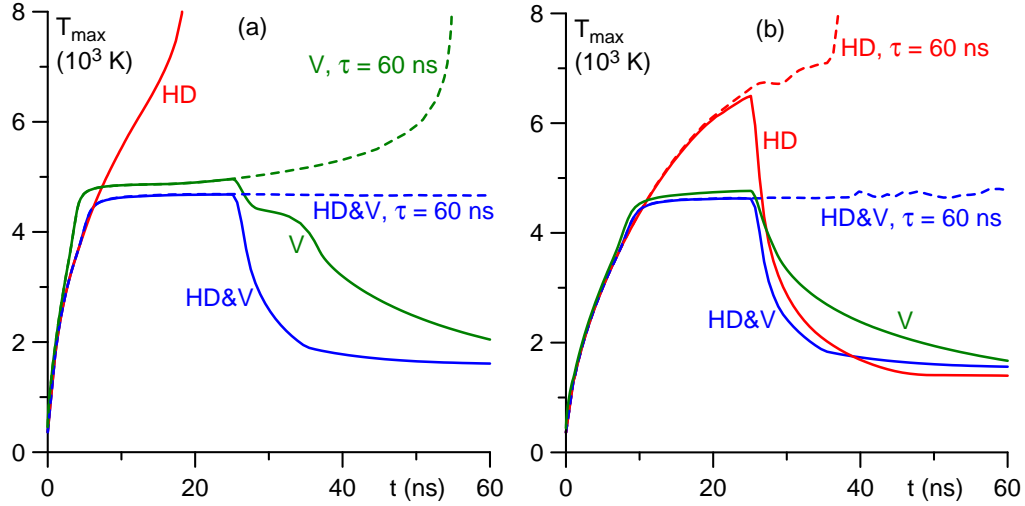


Figure 3.6: Temporal evolution of the maximum cathode temperature. (a) Cathode with the microprotrusion. (b) Planar cathode. HD&V: full model. V: model without account of the motion of the melt (the account of the plasma produced in the spot is retained), chapter 2. HD: model without account of the plasma produced in the spot (the account of the motion of the melt is retained).

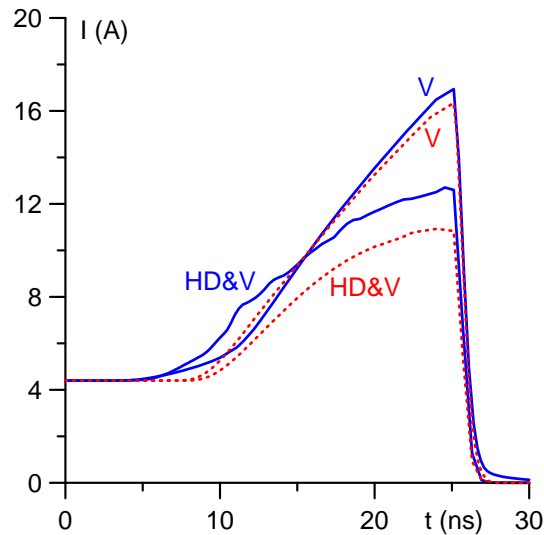


Figure 3.7: Temporal evolution of the spot current. Solid: cathode with the microprotrusion. Dotted: the planar cathode. HD&V: full model. V: model without account of motion of the molten metal, chapter 2.

(thermal runaway) does not occur. Note that the shape of the crater surface in the case of the cathode with the microprotrusion is not smooth, in contrast to the case of the planar cathode, due to the growth of small instabilities that develop as the protrusion is destroyed and are presumably related to the implementation of the level-set method.

Let us now consider the above-described evolution in some detail. The initial phase of the (rapid) temperature increase was interpreted in chapter 2 as the spot ignition phase. The current is constant during this phase as shown by the horizontal section of the dependence $I(t)$ in figure 3.7. Some melting of the cathode surface occurs, however the deformation of the surface on such short times is small; figures 3.4a and 3.5a. Therefore, the inclusion of the account of the motion of the molten metal in the modeling has not greatly affected the ignition phase and this explains the identical spot ignition times, $t_{ig} \approx 5$ ns for the cathode with the microprotrusion and $t_{ig} \approx 8$ ns for the planar cathode, obtained in this work and in the modeling without account of the motion of the melt in chapter 2.

The spot ignition phase is followed by the expansion phase: the spot expands, while the maximum spot temperature changes little. The expansion phase comprises states between (a) and (b) in figures 3.4 and 3.5. The spot current increases; this is due to the spot expansion and a moderate increase of the current density caused by a weak increase in temperature. The motion of the molten metal comes into play during the expansion phase: the shape of the cathode surface changes and the molten material is pushed outward; a crater with a rim is formed. The main driving mechanism of the motion of the molten metal is the action of the plasma pressure due to incident ions. Craters are thus formed without an explosion, as the maximum temperature of the metal does not exceed 4700 – 4800 K.

The expansion stops at $t = 25$ ns, when the leftover plasma cloud is extinguished, and the temperature rapidly decays ($T_{\max} \approx 2000$ K already at $t \approx 30$ ns): the spot is quenched by heat removal into the cathode bulk due to thermal conduction. However, the melt velocity is rather high (the maximum velocity is approximately 180 m/s) by the moment when the leftover plasma cloud is extinguished, so a liquid-metal jet is formed under the effect of fluid inertia.

Thus, one can speak of a jet development phase which follows the expansion phase, i.e., starts after the leftover plasma cloud has been extinguished. At $t = 40$ ns (figures 3.4c and 3.5c), the bottom of the crater has cooled further, the temperature being approximately 1400 K, while the jet head is slightly hotter with a temperature above 1700 K. At $t \approx 55$ ns most of the crater has attained a temperature below the melting temperature of copper, which is 1358 K, and has solidified; figures 3.4d and 3.5d. The still molten jet head detaches soon after; figures 3.4e and 3.5e. We remind that the model used in this work is axially symmetric, so the detached droplet is, in fact, a

ring. For brevity, we shall continue to refer to the ejected material as a "droplet".

3.3.2 Effect of motion of the melt on the spot development

Lines "V" in figures 3.6 and 3.7 depict results of simulation for the same conditions as above-described, but without the account of the motion of the molten metal. (These lines depict data taken from chapter 2; cf. figures 2.3c and 2.8a of section 2.3 for the cathode with the microprotrusion.) One can see that the evolution of the maximum cathode temperature and spot current with and without account of the melt motion is similar. Moreover, there is little quantitative difference between the values of the maximum cathode temperature for $t \leq 25$ ns, i.e., during the ignition and expansion phases; figure 3.6. The value of approximately 4700 – 4800 K achieved during the expansion phase in both models is the surface temperature at which the combined ion bombardment heating is balanced by the electron emission cooling, as discussed in section 2.3. Slightly lower values of T_{\max} given by the full model (lines "HD&V" in figures 3.6a and 3.6b) result from an additional cooling mechanism in the spot accounted for in this model: the heat transport due to motion of the molten metal.

There is little quantitative difference between the values of the current obtained with and without account of the melt motion during the ignition phase (for $t \leq 5$ ns for the cathode with the microprotrusion and for $t \leq 8$ ns for the planar cathode); figure 3.7. The difference becomes more pronounced during the expansion phase: the maximum current attained with account of the melt motion is of about 10 – 12 A (lines "HD&V" in figure 3.7), while without the melt motion the current reaches approximately 16 A (lines "V" in figure 3.7). One of the factors contributing to this difference are the above-mentioned slightly lower values of the surface temperatures and, consequently, of the density of electric current delivered to the cathode by the plasma produced in the spot.

It was shown in chapter 2 that as the Joule heating comes into play in the modeling without account of the motion of the molten metal, the maximum of the cathode temperature is shifted from the surface into the cathode and thermal runaway starts developing. This instability is quenched if the time of action of the leftover plasma cloud is too short; otherwise the explosion occurs. The latter is exemplified by the line marked "V, $\tau = 60$ ns" in figure 3.6a for the case of the cathode with the microprotrusion. In this example, the explosion occurs at 55 ns.

In this connection, calculations were also performed with account of the motion of the melt (i.e., by means of the full model) with the time of action of the leftover plasma cloud extended up to 60 ns. The resulting temporal evolution of the maximum cathode temperature is shown in figures 3.6a and 3.6b by lines marked "HD&V, $\tau = 60$ ns".

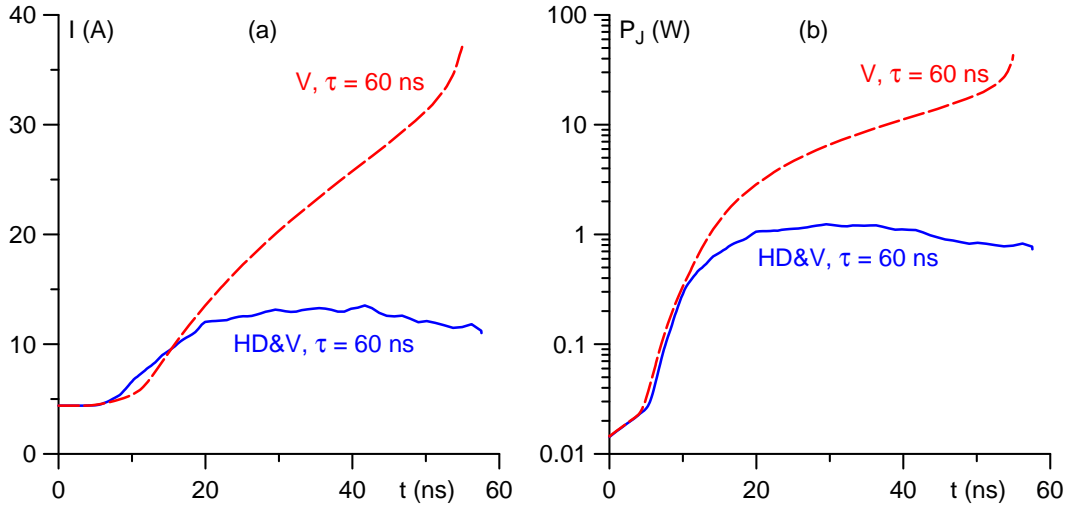


Figure 3.8: Temporal evolution of the spot current (a) and the power dissipated due to Joule heating (b). Cathode with the microprotrusion. HD&V: full model. V: model without account of motion of the molten metal, chapter 2.

It can be seen that the temperature in the cathode remains limited: thermal runaway does not develop either. Note that the crater continues expanding and the jet does not form.

The spot current and the Joule heating computed with and without the account of the motion of the molten metal with $\tau = 60$ ns are depicted in figure 3.8 by the lines "HD&V, $\tau = 60$ ns" and "V, $\tau = 60$ ns", respectively. The current computed with the account of the motion of the melt with $\tau = 60$ ns does not change much in the time range $25 \text{ ns} < t < 60 \text{ ns}$ and is around 12 A, while the current computed without the account of the melt motion continues to rapidly increase; figure 3.8a. Therefore, the Joule heating with the account of the melt motion is considerably lower (figure 3.8b), which is why the thermal runaway does not develop.

3.3.3 Effect of the plasma produced in the spot

The only mechanism of current, momentum, and energy transfer to the cathode surface included in the model of the previous works [53, 54] was the flux of ions from the plasma cloud; the contributions of the vapor emitted in the spot, ions and electrons produced by ionization of the vapor, and the electron emission from the cathode surface have been neglected. In designations of this work, the contributions j_2 , p_2 , and q_2 were taken into account but j_1 , p_1 , and q_1 neglected. In this section, the effect of the mechanisms represented by the terms j_1 , p_1 , and q_1 is investigated. For brevity, this effect is referred to as that of the plasma produced in the spot.

Results of simulations performed without account of the terms j_1 , p_1 , and q_1 are shown by the lines "HD" in figures 3.6a and 3.6b. There is no plateau in the evolution of T_{\max} , as the cathode surface temperature is not limited by the mechanism of electron emission cooling. In the case of the cathode with the microprotrusion, the critical temperature is reached in $t \approx 19$ ns; line "HD" in figure 3.6a. Note that, in contrast to the case of the model where the plasma produced in the spot is taken into account while the melt motion is neglected (chapter 2), the achievement of the critical temperature in these simulations is not due to the development of a thermal instability, but simply due to heating of the cathode surface by an external energy source. In this sense, the term "thermal runaway" does not seem to be appropriate. Another manifestation of the difference between the results of the two models is that T_{\max} in the model without the plasma produced in the spot occurs on the surface, rather than inside the cathode; in this sense, the term "explosion" does not seem to be appropriate either.

The evolution of T_{\max} in the case of the planar cathode (line "HD" in figure 3.6b) is similar but slower: the maximum cathode temperature attained at $t = 25$ ns is approximately 6500 K. If the time of action of the leftover plasma cloud is extended, the critical temperature may be reached at $t \approx 38$ ns; line "HD, $\tau = 60$ ns" in figure 3.6b.

In the case of the cathode with the microprotrusion, the protrusion is destroyed but a crater does not form before the critical temperature has been reached. Heating of the planar cathode is slower, which allows sufficient time for a crater to form. The evolution of the temperature distribution in the planar cathode and of the cathode surface deformation is shown in figure 3.9. The evolution is similar to that found in the framework of the full model and shown in figure 3.5, however, with an important difference: solidification of the liquid metal jet occurred before a droplet could detach; figure 3.9d.

This result can be understood as follows. In the simulations in the framework of the full model given in this chapter, the plasma pressure p_{pl} includes the contribution from the plasma produced in the spot, i.e., $p_{pl} = p_1 + p_2$, and the pressure at the spot center for $t = 25$ ns equals 0.38 GPa. In the modeling where the plasma produced in the spot is neglected, $p_{pl} = p_2$ and the pressure at the spot center for $t \leq 25$ ns equals 0.28 GPa. As a consequence, the maximum force exerted by the plasma pressure p_{pl} on the cathode surface in the full model is about 15% higher as seen in figure 3.10a. The maximum velocity acquired by the molten metal is thus about 40% higher in the framework of the full model; figure 3.10b. For this reason, the speed of motion of the jet under its inertia is greater than the speed of propagation of the solidification front in the jet, culminating in the detachment of the droplet in the framework of the full model. The opposite occurs in the modeling where the plasma produced in the

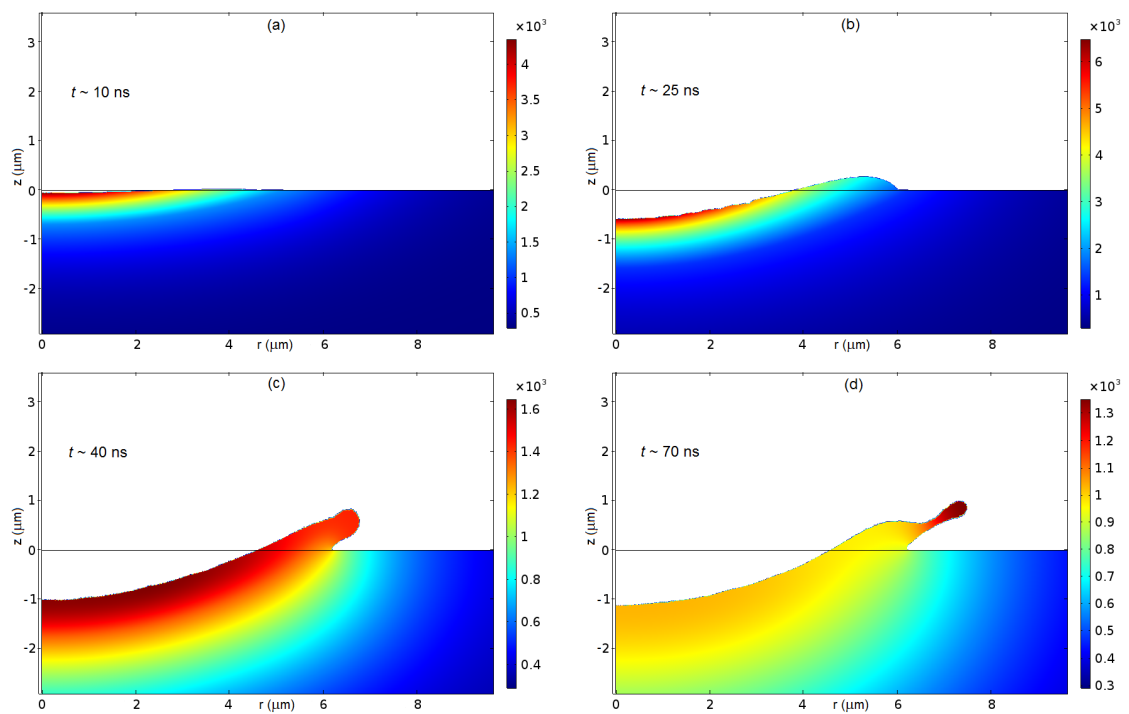


Figure 3.9: Evolution of the temperature distribution and cathode surface deformation for the case of the planar cathode. The plasma produced by ionization of the emitted vapor is neglected. The bar in K.

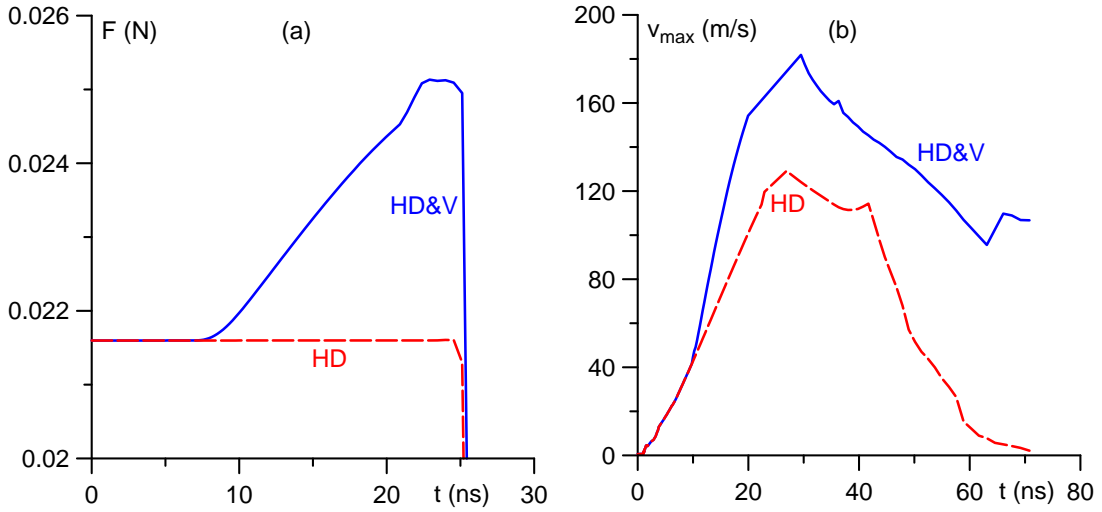


Figure 3.10: Temporal evolution of the force exerted over the cathode surface by incident ions (plasma pressure) (a) and the maximum velocity acquired by the molten metal (b). Planar cathode.

spot is neglected: the speed of propagation of the solidification front, being greater than the speed of the jet head, causes complete solidification before the detachment of the jet head could occur; figure 3.9d. Thus, the pressure exerted by incident ions produced by the ionization of the metal vapor emitted in the spot plays a key role in the detachment of the jet head.

3.3.4 Effect of magnetic field on the hydrodynamics of the molten metal in the spot

It is well-known that when a transverse magnetic field is present, spots on arc cathodes move predominantly in the anti-Amperian, or retrograde, direction. This retrograde motion of cathode arc spots was discovered over one hundred years ago, and while a number of theoretical models have been proposed to explain the phenomenon, the first-principle understanding is still missing; e.g., [3, 4, 139].

The net transverse magnetic field in the spot is a superposition of the external and self-induced fields. A first step to understanding the motion of spots due to the presence of a magnetic field is to study the effects of the transverse magnetic field on the distribution of spot parameters. The effect of the magnetic field on the hydrodynamic processes in the spot, in particular on the formation of the liquid-metal jet and droplet detachment is discussed here.

The temporal variation of the maximum self-induced magnetic field $B_{\phi, \max}$ computed in the framework of the full model is shown in figure 3.11a for both the cathode

with the microprotrusion and the planar cathode. Shortly after the leftover plasma cloud has been extinguished at $t = 25$ ns, $B_{\phi, \max}$ attains a maximum value of about 0.55 T for the cathode with the microprotrusion and of about 0.4 T for the planar cathode.

Since the model employed in this work is axially symmetric, it is not possible to study the effect of an external transverse magnetic field (this would require 3D simulations, which have not been attempted). Nevertheless, in order to obtain an estimate of the effect of the transverse magnetic field on the hydrodynamic processes in the cathode spot, two sets of simulations have been performed: the first, without an account of the self-induced magnetic field, and the second, with the self-induced magnetic field amplified by a factor of 10. As an example, the shape of the cathode surface and the developing liquid-metal jet at the moment $t = 55$ ns is shown in figure 3.11b, and the shape of the cathode surface and the detached droplet at the moment $t = 70$ ns are shown in figure 3.11c. Both figures refer to simulations for the planar cathode. One can clearly see that, to the numerical accuracy, there is no effect on the motion of the molten metal; there are no differences in the evolution of the spot, crater formation or droplet detachment, whether or not the self-induced magnetic field is taken into account, or even when it is amplified.

3.3.5 Cathode erosion

The modeling results relevant for analysis of cathode erosion are summarized in table 3.1. The designations are as follows. $\Gamma_v = \int \int m_i J_v dA dt$ is the total mass of the vapor emitted from the spot during its lifetime, where J_v is the flux of atoms emitted by the surface estimated by means of the Langmuir formula and the integrals are evaluated over the cathode surface and over the lifetime of the spot. Γ_d is the mass of the ejected droplet. $\Gamma_1 = \Gamma_v - \int \int G dA dt$ is the mass of the atoms vaporized in the spot that have returned to the cathode surface in the form of ions (here G is the rate of loss of mass by the cathode due to the vaporized atoms that have not immediately returned to the cathode surface; in the framework of the 1D model of near-cathode plasma layers in vacuum arcs [62] employed in this work, G is evaluated as a function of the local cathode surface temperature and near-cathode voltage drop with the use of the self-consistent solution of the Poisson equation describing the space-charge sheath on vaporizing cathodes [61]). $\Gamma_2 = \frac{m_i}{e} j_i^{(cl)} \pi a^2 \tau$ is the total mass of the ions from the leftover plasma cloud that have reached the cathode surface during the lifetime of the spot. $Q_1 = \int \int j_1 dA dt$ and $Q_2 = j_i^{(cl)} \pi a^2 \tau$ are charges transported to the cathode by the plasma produced in the spot (including the emission current) and by the ions from the plasma cloud, respectively. Finally, $\gamma_v = (\Gamma_v - \Gamma_1) / \Gamma_v$ is the fraction of

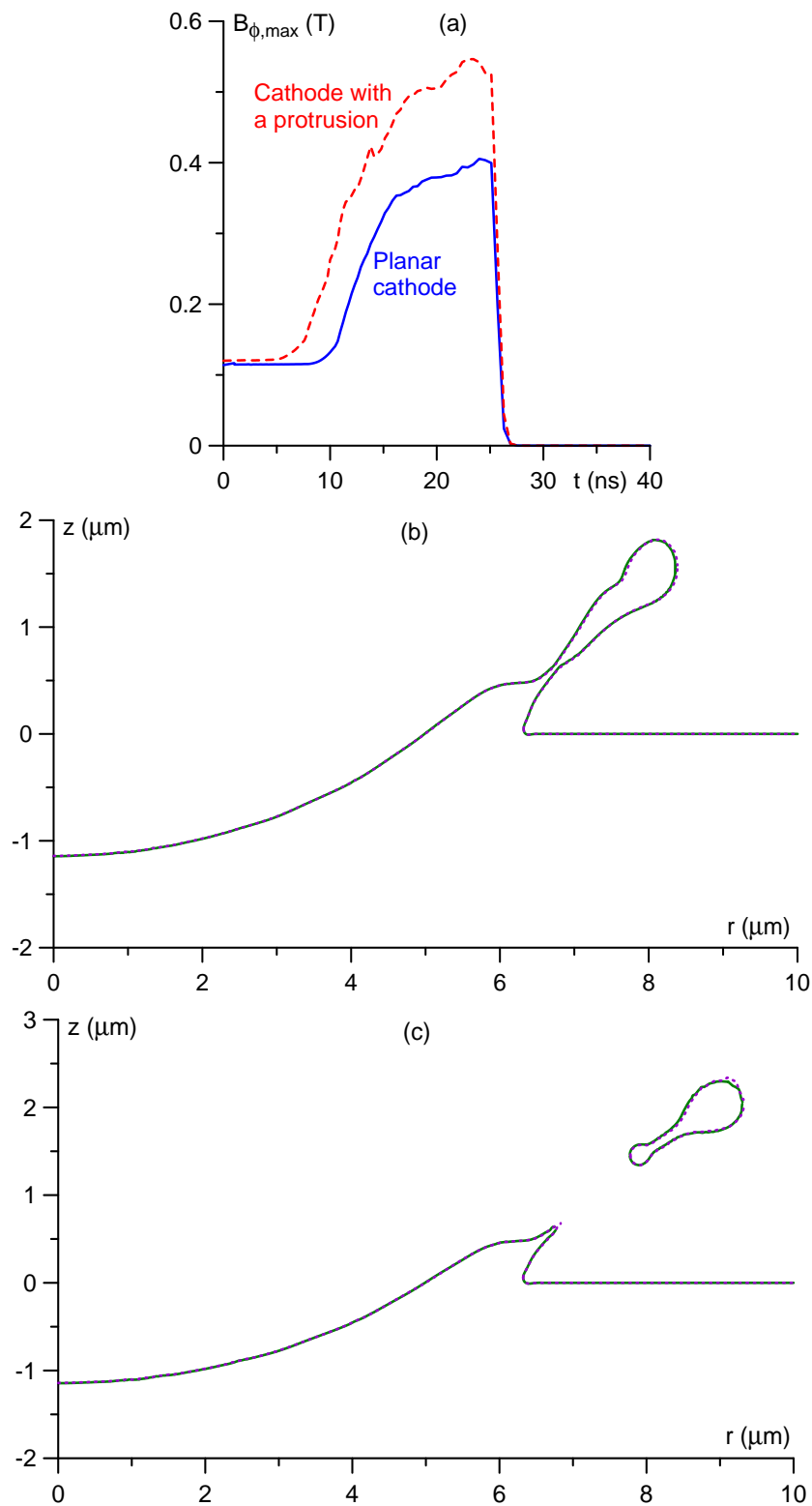


Figure 3.11: (a) Temporal evolution of the maximum self-induced magnetic field in the spot. (b) Effect of the magnetic field on the crater and liquid-metal jet formation; $t = 55$ ns. (c) Effect of the magnetic field on the droplet detachment; $t = 70$ ns. (b), (c) Solid line: the self-induced magnetic field is neglected; dotted line: the self-induced magnetic field is amplified by a factor of 10.

	microprotrusion	planar
Γ_v (10^{-12} g)	6	5
Γ_d (10^{-12} g)	210	220
Γ_1 (10^{-12} g)	5.2	4.3
Γ_2 (10^{-12} g)	74	74
Q_1 (μC)	0.1	0.07
Q_2 (μC)	0.11	0.11
γ_v	0.13	0.14
g_2 ($\mu\text{g}/\text{C}$)	340	400
g_v ($\mu\text{g}/\text{C}$)	28	27
g_d ($\mu\text{g}/\text{C}$)	980	1200

Table 3.1: Relevant erosion data computed in the framework of the model of this work.

the vaporized atoms that have not immediately returned to the cathode surface; the so-called escape factor.

The rate of erosion of electrodes is usually characterized by the specific erosion (the so-called g -factor), defined as the loss of mass by the electrode per unit charge transported. In this connection, also shown in table 3.1 are quantities $g_\alpha = \Gamma_\alpha/Q$, $\alpha = 2, v, d$, where $Q = Q_1 + Q_2$ is the total charge transported in the spot.

Before discussing the data shown in table 3.1, it is convenient to give a few simple considerations based on available experimental information. If there are no explosions that could result in the emission of ionized cathode material or solid particles, then the transport of mass from the cathode into the near-cathode plasma is due to the emission of vapor and the ejection of droplets: $\Gamma_+ = \Gamma_v + \Gamma_d$. The material returns to the cathode surface in the form of ions: $\Gamma_- = \Gamma_1 + \Gamma_2$. The net loss of mass of the cathode caused by the existence of an individual spot is

$$\Gamma = \Gamma_v + \Gamma_d - \Gamma_1 - \Gamma_2. \quad (3.18)$$

Dividing equation (3.18) by Q , one can write it in the form

$$g = \gamma_v g_v + g_d - g_2, \quad (3.19)$$

where $g = \Gamma/Q$ is the specific erosion of the cathode.

Since $\Gamma_2 = m_i Q_2/e$, one can write

$$g_2 = \frac{Q_2 m_i}{e(Q_1 + Q_2)}. \quad (3.20)$$

An upper estimate of the rhs can be obtained by neglecting the charge transport by the plasma produced in the spot, following [53]. A bit more realistic estimate can be obtained by assuming that contributions of the cloud and the plasma produced in the

spot (once again, including the emission current) are comparable. Setting in equation (3.20) $Q_1 = Q_2$, one obtains $g_2 = 330 \mu\text{g}/\text{C}$.

Assuming that most of the vaporized atoms are ionized in the immediate vicinity of the cathode surface and return to the cathode surface as ions, one can drop the first term on the rhs of equation (3.19). Experimental values $g = 115 - 130 \mu\text{g}/\text{C}$ have been reported for the erosion for copper cathodes [139]. Setting in equation (3.19) $g = 120 \mu\text{g}/\text{C}$, one can estimate the specific mass flux from the cathode surface related to the droplet ejection: $g_d = 450 \mu\text{g}/\text{C}$.

The droplets are partially vaporized in the very dense and hot plasma ball adjacent to the spot; e.g., [140]. The vapor is ionized and a part of the produced ions move away from the cathode with the plasma jet. The rest of the ions remain in the near-cathode region and thus form a new plasma cloud, which will eventually ignite the next spot. The flux of the ions in the vacuum arc plasma jet (the so-called ion erosion) measured for copper cathodes is $33 - 37 \mu\text{g}/\text{C}$ [4, p. 157], hence the flux of the liquid phase may be estimated as $120 \mu\text{g}/\text{C} - 35 \mu\text{g}/\text{C} = 85 \mu\text{g}/\text{C}$. It follows that of the initial mass of the droplet ejected only about $85 \mu\text{g}/\text{C}$ move into the bulk of the arc in the form of a droplet. The rest of the mass of the droplet, $365 \mu\text{g}/\text{C}$, is vaporized in the plasma ball, with $330 \mu\text{g}/\text{C}$ forming the new plasma cloud in the near-cathode region and $35 \mu\text{g}/\text{C}$ going into the bulk with the jet in the form of ions. A schematic illustrating these estimates is shown in figure 3.12.

The above estimates are based on experimental values. They do not make use of results of simulations of this work and can therefore be compared with these results. In fact, the results shown in table 3.1 conform to the estimates. Values of Q_1 and Q_2 in table 3.1 are indeed comparable as assumed above. It is not surprising therefore that the values of the specific mass flux g_2 from the plasma cloud in table 3.1 are close to the estimated value of $330 \mu\text{g}/\text{C}$. The specific flux of ions originating in the vaporization of the cathode surface which do not return to the cathode, $\gamma_v g_v$, evaluated using γ_v and g_v from table 3.1, amounts to about $3.7 \mu\text{g}/\text{C}$ and is much smaller than the other terms of equation (3.19) as expected.

As previously discussed, the assumption of axial symmetry in the modeling leads to the formation of an axially symmetric jet at the crater periphery and the detachment of a ring; figure 3.13. In reality, however, neither the leftover plasma cloud that causes spot ignition nor protrusions on the surface of the cathode are axially symmetric, thus a ring jet cannot develop; instead, one or a few 3D jets will be formed. Another reason for breaking of the axial symmetry may be the development of the Rayleigh-Plateau hydrodynamic instability at the crater rim [53, 57–59]. Thus, the mass of the computed hypothetical ring gives an upper estimate of the mass of the ejected droplet. Indeed, the values of g_d of $980 \mu\text{g}/\text{C}$ and $1200 \mu\text{g}/\text{C}$ appearing in table 3.1, exceed

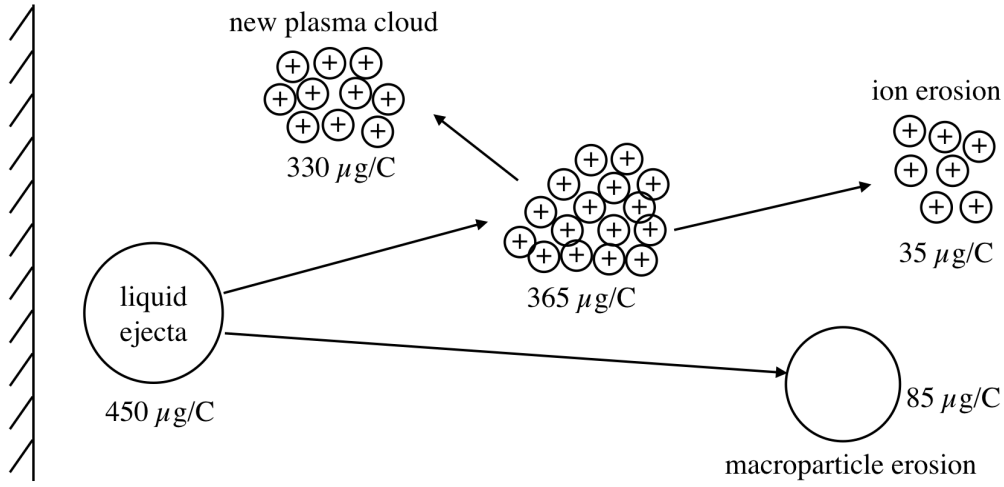


Figure 3.12: Schematic of cathode erosion based on estimates of different mechanisms of cathode erosion derived from the experimental data on net and ion erosion of copper cathodes.

the value of $450 \mu\text{g}/\text{C}$ deduced above from the experimental data by a factor of 2.2 or 2.7. In other words, no more than approximately 40% of the material constituting the hypothetical ring computed in the axially symmetric geometry actually detaches from the surface.

It is of interest to estimate the energy deposited in the plasma ball by the plasma produced in the spot during its lifetime. It may be estimated as $\int \int \frac{j_1}{e} 3.2kT_e^{(1)} dA dt$ (here $T_e^{(1)}$ is the temperature of electrons in the near-cathode layer, which is computed as a function of the local cathode surface temperature and near-cathode voltage drop by means of the code [62]) and equals $1.5 \mu\text{J}$ for the cathode with the microprotrusion and $1.1 \mu\text{J}$ for the planar cathode. In order for the model to be self-consistent, this energy should coincide with, or exceed, the energy needed to vaporize and ionize a part of the ejected droplet and thus form a new plasma cloud similar to the original leftover plasma cloud assumed in the modeling to ignite the spot. The latter energy cannot be computed without accurate 3D simulations of the detachment of the droplets, their interaction with the near-cathode plasma, and vaporization. However, one can perform a crude estimate with the use of the above-given simple considerations based on available experimental information: $365 \frac{\mu\text{g}}{\text{C}} \frac{0.2\mu\text{C}}{m_i} (A_v + A_i + \frac{3}{2}kT_e) = 1.5 \mu\text{J}$. This value coincides with the above value of the deposited energy in the case of the cathode with the microprotrusion. There is an energy deficit in the case of the planar cathode, however this deficit is modest and certainly below the margin of error of the estimates.

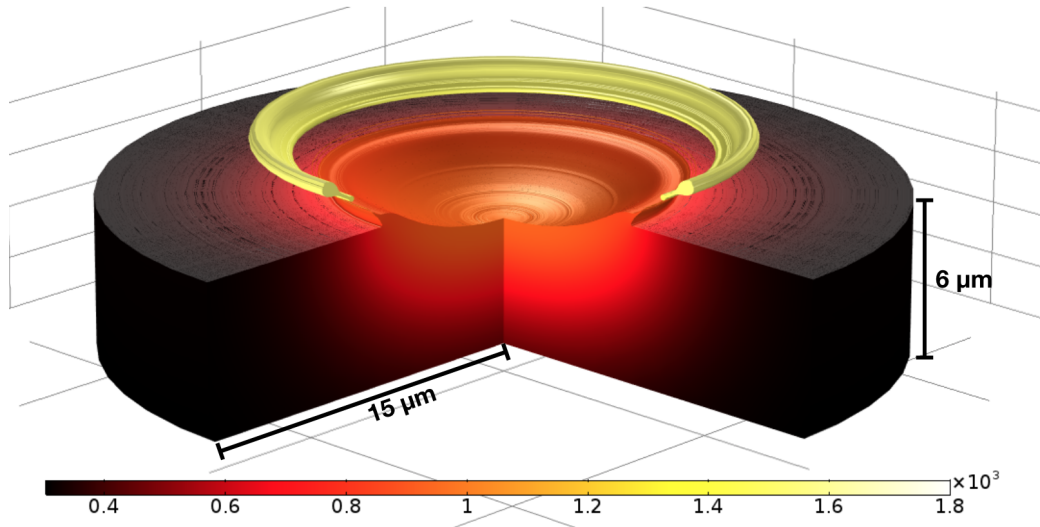


Figure 3.13: Result of simulation of spots on a planar copper cathode in a vacuum arc: temperature distribution and ejected "ring" droplet. The bar is in K.

3.3.6 Comparison with other cathode spot models

Various modes of the crater formation process have been identified in the modeling [53]. If the maximum pressure exerted over the cathode by the plasma cloud was set equal to 0.1 – 0.2 GPa (this pressure was treated in [53] as an input parameter), then the inertial splashing mode occurred: the velocity acquired by the molten metal during the time of action of the leftover plasma cloud leads to the formation of a jet after the cloud has been extinguished. The active splashing mode occurred at a pressure of 0.4 GPa: the jet has developed and the critical temperature is reached during the time of action of the cloud.

In the modeling of this work, the jet formation occurs due to inertia, as in the inertial splashing mode of [53]. However, the computed plasma pressure attains a maximum value of approximately 0.38 GPa, which is comparable with that required for the active splashing mode in [53]. Other substantial differences are that the detachment of a droplet was not observed in the modeling [53], while in the modeling of this work the heating up to the critical temperature was not observed.

The different results obtained in [53] and in this work are owed to the neglect of the interaction of the plasma produced in the spot with the cathode surface in the model [53], in particular the neglect of the cooling due to electron emission and of the pressure exerted by the ions produced from the metal vapor emitted in the spot. The former limits the cathode temperature, while the latter provides the necessary acceleration to the molten metal so that a droplet may detach from the jet before the

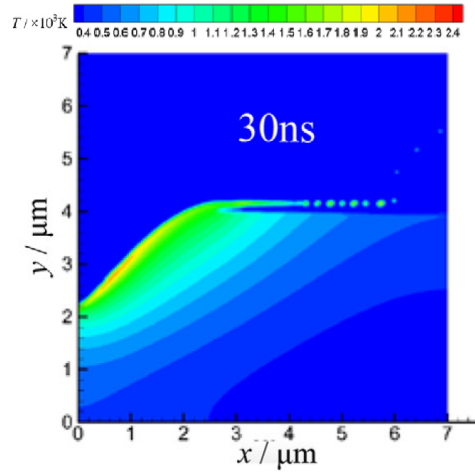


Figure 3.14: Jet formation and droplet detachment as a result of simulations with the model [55].

solidification front has reached the jet head.

In [55, 56], the addition of an account of Joule heating and of cooling due to evaporation of atoms from the cathode surface to the model [53] also resulted in the formation of a crater and a liquid-metal jet at the periphery. In contrast to [53], the ejection of many small droplets parallel to the flat surface of the cathode is observed, figure 3.14. However, this reported simulation result may have been interpreted incorrectly. In order to understand the reported results, let us consider the simplified model of subsection 3.2.5 similar to the model [53]. Appropriate values for the interface width ε_{ls} and stabilization parameter γ_{ls} had to be found, so as to accurately reproduce the liquid-metal jet structure. For example, a preliminary simulation with the simplified model wherein ε_{ls} was set to 50 nm, appeared to result in the detachment of a droplet; figure 3.15a. In the following simulation, ε_{ls} was set to 10 nm, figure 3.15b. It is thus immediately apparent that the previously observed droplet detachment, figure 3.15a, was merely a numerical artifact, i.e., the chosen value of ε_{ls} resulted in an interface too wide to properly resolve the head of the jet. The same incorrect interpretation of the simulation results has presumably occurred in [55, 56].

The modeling of this work could have, in principle, confirmed the physical picture of the ecton concept described in section 1, since all relevant mechanisms are taken into account. However, no explosions are observed in the conditions considered in this work; there is no appreciable effect of the pre-existing μm -size protrusion; craters are formed and droplets detach without an explosion; and even without an explosion, the ejected material and the energy deposited in the plasma are sufficient to instigate the

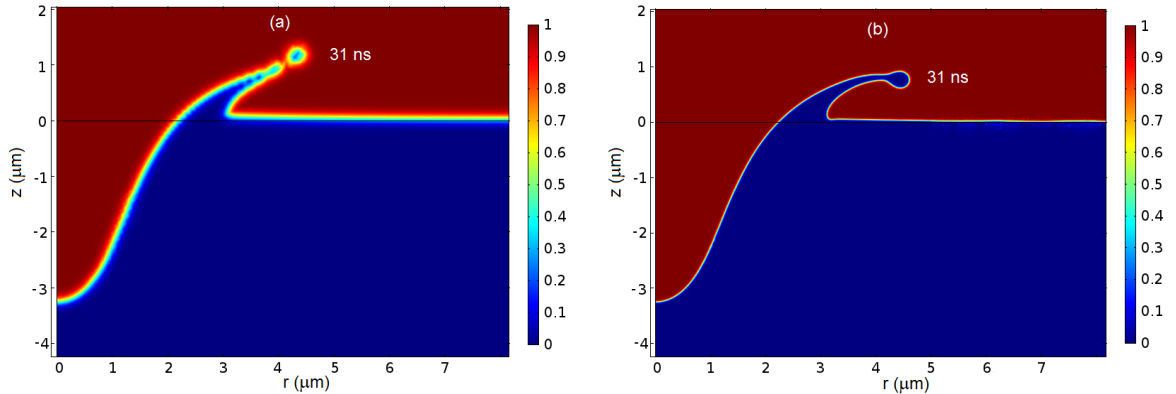


Figure 3.15: Formation of a jet, resulting from simulation with the simplified test model based on the work [53]. Level-set function distribution. (a): $\varepsilon_{ls} = 50$ nm. (b): $\varepsilon_{ls} = 10$ nm.

formation of a new plasma cloud that will ignite a subsequent spot.

Another physical picture of cathode spot development was proposed in [41, 42]: an external plasma heats the cathode and initiates the spot; once the external plasma has been extinguished, the spot evolves until a steady state is reached. The results of the modeling of this work are in a clear contradiction with the latter conclusion. The model [41, 42] differs from the model of this work in a number of important aspects: the heat conduction in the cathode is treated by means of an equation of integral heat balance instead of the differential equation (which results in a loss of information and, consequently, the model not being self-consistent [141]); the development of a spot is computed for a given value of the spot current (and not of the near-cathode voltage drop, as done in this work in order to simulate high-current vacuum arcs); and the hydrodynamic phenomena are not taken into account. Presumably, the latter difference is the most important one: the account of motion of the molten metal, taken into account in this work, prevents a spot from attaining a steady state.

3.4 Summary and concluding remarks

The developed model describes the initiation and development of an individual cathode spot in a high-current vacuum arc with account of the most important mechanisms: the bombardment of the cathode surface by ions coming from a previously existing plasma; vaporization of the cathode material in the spot, its subsequent ionization and the interaction of the produced plasma with the cathode; Joule heating in the cathode body; motion of the molten metal under the effect of pressure exerted by the plasma and the Lorentz force; the change in shape of the molten cathode surface; the

formation of craters and liquid-metal jets; the detachment of droplets.

The results of the modeling allow one to identify three phases of the spot life cycle. The ignition phase is characterized by a rapid increase of the cathode temperature up to 4700–4800 K and lasts for approximately 5 ns on the cathode with the microprotrusion and 8 ns on the planar cathode; figures 3.4a and 3.5a. Some melting of the cathode surface occurs, however the deformation of the surface on such short times is small. Therefore, the spot development during this phase occurs essentially in the same way as in the modeling without account of the motion of the melt in chapter 2.

The subsequent expansion phase is characterized by a plateau in the temporal evolution of T_{\max} and an increase in the spot current I . A crater is formed due to the displacement of the molten metal from the center of the spot due to the pressure exerted by the plasma.

After the leftover plasma cloud has been extinguished at $t = 25$ ns (figures 3.4b and 3.5b), no more energy is supplied to the cathode. The crater expansion stops and the spot starts being rapidly destroyed by heat removal into the bulk of the cathode due to thermal conduction. However, the melt velocity is quite high at this moment, leading to the formation of a liquid-metal jet under the effect of fluid inertia; figures 3.4c and 3.5c. This stage may be called the jet development phase. It culminates in the detachment of the head of the jet: a droplet appears; figures 3.4d and 3.4e, and 3.5d and 3.5e.

The cathode temperature does not exceed 4700 – 4800 K during the whole lifetime of the spot even if the time of action of the plasma cloud is extended. This is a consequence of the cooling due to electron emission and of convective heat transfer. If the latter mechanism is discarded, then the Joule heating becomes sufficient to initiate the thermal runaway inside the cathode body and the temperature reaches the critical temperature of copper: a microexplosion occurs; e.g., line "V, $\tau = 60$ ns" in figure 3.6a. In the simulations where the contribution of the plasma produced in the spot (and the electron emission cooling) is discarded, the critical temperature is attained as well; e.g., line "HD" in figure 3.6a. However, the temperature maximum occurs on the cathode surface in this case; the achievement of the critical temperature is simply due to heating by an external source rather than due to the development of a thermal instability (thermal runaway). In this sense, the term "explosion" is not appropriate in this case.

Craters are formed during the expansion phase, under the action of the pressure exerted by the plasma over the cathode surface. Jet formation and droplet detachment occur under the effect of fluid inertia once the leftover plasma cloud has been extinguished. Thus, craters form and droplets detach without an explosion. Moreover, the spot and cathode surface evolution are essentially the same on both the planar cath-

ode and the cathode with the $1\ \mu\text{m}$ -scale microprotrusion: the presence of a surface nonuniformity has no appreciable effect on the spot development.

The pressure exerted over the cathode by the ions produced from the metal vapor emitted in the spot is significantly higher than the saturated vapor pressure. It follows that, independently of the presence or absence of the leftover plasma cloud, the pressure inside the molten metal is sufficient to prevent a transition into the gaseous state; bubbles do not appear and no boiling occurs.

It was found that for typical conditions of cathode spots in vacuum arcs the effect of the self-induced magnetic field on the formation of the liquid-metal jet and droplet detachment is negligible, even when (artificially) enhanced by a factor of 10. The self-induced magnetic seems to be hardly relevant for the retrograde motion of cathode spots, and the first-principle understanding of the retrograde motion is still lacking.

The modeling results conform to estimates of different mechanisms of cathode erosion, derived from experimental data on the net and ion erosion of copper cathodes of vacuum arcs. The loss of mass of the cathode due to vaporization is virtually compensated by the return of the vaporized atoms in the form of ions, so the dominant erosion mechanism is the ejection of liquid droplets, partially compensated by ion flux from the plasma cloud. The emitted droplets are partially vaporized in the near-cathode region. The produced vapor is ionized and a part of the ions move away from the cathode with the plasma jet. The rest of the ions remain in the near-cathode region and thus form a new plasma cloud, which will eventually ignite the next spot.

In real experimental situations, neither the leftover plasma cloud nor protrusions on the surface of the cathode are axially symmetric, hence the droplets are 3D rather than ring-shaped, as in the (axially symmetric) modeling of this work. Thus, the computed mass of the hypothetical ejected ring gives only an upper estimate of the mass of the ejected droplet: the former exceeds the latter by a factor of about 2.5.

Chapter 4

Numerical simulation of the initial stage of unipolar arcing in fusion-relevant conditions

4.1 Introduction

Arcing in fusion devices has been a longstanding research issue for many years; e.g., [17]. It is known that arcing between the plasma and the wall, triggered by instabilities in the plasma during its operation, is of unipolar nature. A number of experimental works on the ignition of unipolar arcs in a laboratory have been carried out (cf. section 1); of particular interest for this work, is the experiment [75]. In the experiment, an isolated tungsten plate was exposed to a helium plasma, and then irradiated by a laser pulse with a peak power of about 10^{10} W/m². The ignition of an arc was evidenced by bright emission detected by a fast camera, the increase of the plate potential from the floating potential by about 30 V and by the erosion trails left on the plate. The laser pulse had a pulse width of approximately 0.6 ms. After having increased by about 30 V at the beginning of the pulse, the plate potential did not immediately return to the floating potential when the laser was switched off and rather remained more or less constant at about 30 V above the floating potential for nearly 3 ms, before returning to the floating potential.

The results of the experiment [75] suggest that there are two phases of unipolar arcing. In the initial phase, arcing is triggered and sustained by an intense external heat flux, i.e., a laser pulse, similar to what happens at the initial stages of formation of cathode spots in vacuum arcs. Order-of-magnitude estimates show that a nanostructure with a height of the order of $1\ \mu\text{m}$, as those of the experiments, will attain the melting temperature within $1\ \mu\text{s}$ and will then be destroyed within another mi-

crosecond. Hence, the nanostructures can hardly affect the initial stage of unipolar arcing and this stage is similar to what happens at the initial stages of formation of cathode spots in vacuum arcs. After the external heat flux is switched off, arcing continues in a second phase, the mechanism of sustainment being presumably related to the nanostructures present on the metal surface. One could think of explosions of the nanostructures due to field emission, in agreement with the model [19]. Alternatively, given that heating of the surface during the initial phase is a necessary precursor for the second phase, one could think of explosions, due to thermo-field emission, of hot nanostructures in the immediate vicinity of the initial impact site, that were heated but not destroyed by the initial external heat flux irradiation; a mechanism observed in simulations of chapter 2.

It is therefore of interest to apply a model similar to that used for the description of the plasma-cathode interaction in vacuum arcs for the initial phase of unipolar arcing in fusion devices. The latter is the objective of this chapter. More specifically, we will simulate the interaction of an intense heat flux with and current transfer to a tungsten metal plate immersed in a helium background plasma in conditions based on the experiment [75]. The detailed numerical model developed for the modeling of plasma-cathode interaction in vacuum arcs in chapter 3 is used to this end. The model takes into account an external energy source (the laser beam), which delivers the intense heat load to trigger the arcing, the vaporization of the tungsten atoms at the laser impact site, the ions and electrons produced by ionization of the vapor and the electron emission from the metal surface, and relevant hydrodynamic phenomena, including convection and surface deformation. Since the arc is unipolar, the model of chapter 3 is supplemented with an account of current transfer outside the arc attachment and the arc voltage is evaluated from the condition of the net current to the plate being zero at each moment.

The outline of the chapter is as follows. The numerical model is introduced in section 4.2. Results of simulation are reported in section 4.3 and discussed in section 4.4. Conclusions are summarized in section 4.5.

4.2 The model

4.2.1 Equations and boundary conditions

Let us consider a metal plate immersed in a background plasma and subjected on one side to an intense external heat load. The model of chapter 3 is used in this work with appropriate modifications. The model comprises the Navier-Stokes equations describing the motion of the molten metal of the plate, in conjunction with the heat

transfer equation in the plate, including both the melt and the solid:

$$\nabla \cdot \mathbf{u} = 0, \quad (4.1)$$

$$\rho \frac{\partial \mathbf{u}}{\partial t} + \rho(\mathbf{u} \cdot \nabla)\mathbf{u} = \nabla \cdot [-p\mathbf{I} + \mu(\nabla\mathbf{u} + (\nabla\mathbf{u})^T)], \quad (4.2)$$

$$\rho c_p \frac{\partial T}{\partial t} + \rho c_p \mathbf{u} \cdot \nabla T = \nabla \cdot (\kappa \nabla T). \quad (4.3)$$

Here ρ is the the mass density of the metal, c_p and κ are the specific heat and the thermal conductivity of the metal, and μ is the viscosity of the melt, \mathbf{u} is the velocity, p is the pressure, and \mathbf{I} is the identity tensor. The equations are solved under the assumption of axial symmetry in cylindrical coordinates (r, z) , with material parameters ρ , c_p , κ and μ considered as known functions of the temperature T . The calculation domain for equations (4.1) and (4.2) is the molten part of the plate, and for equation (4.3) it is the whole of the plate, including both the molten and solid parts.

Forces due to surface tension effects and due to the pressure p_{tot} exerted by the plasma and by the external heat load are introduced as boundary conditions on the molten metal surface for the Navier-Stokes equations,

$$[-p\mathbf{I} + \mu(\nabla\mathbf{u} + (\nabla\mathbf{u})^T)] \cdot \mathbf{n} = -p_{tot}\mathbf{n} + \mathbf{F}_{st}. \quad (4.4)$$

The pressure p_{tot} comprises contributions from the plasma produced from the metal vapor emitted in the spot, p_1 , from the external heat load, p_2 , and from the background plasma, p_3 ; the force \mathbf{F}_{st} due to surface tension is evaluated in the usual way, in terms of the curvature of the molten metal surface and the surface tension coefficient of the material. The velocity \mathbf{u} vanishes at the interface between the molten and solid metal.

The boundary conditions for the heat conduction equation (4.3) are written in terms of densities of the energy flux q from the plasma to the plate surface, i.e., $\kappa \mathbf{n} \cdot \nabla T = q$. The model takes into account four contributions to q , computed independently of each other:

$$q = q_1 + q_2 + q_3 - q_4, \quad (4.5)$$

where q_1 is the contribution to the density of the energy flux to the plate surface due to the vapor emitted in the spot, ions and electrons produced by ionization of the vapor, and the electron emission from the metal surface; q_2 is the density of the energy flux delivered to the surface by the external heat load (laser beam); q_3 is the density of the energy flux delivered to the plate by the ions and the electrons from the background plasma, and q_4 is the density of the energy flux lost by the plate surface due to radiation into the plasma.

The net density of electric current j transferred from the plasma to the metal surface is comprised of two independent contributions,

$$j = j_1 + j_3, \quad (4.6)$$

where j_1 is the density of electric current due to the ions generated from the vaporized atoms and due to the emission of electrons in the spot, and j_3 is the density of electric current transported to the plate surface by the ions and electrons from the background plasma, which is minor inside the laser impact area and of primary importance on the rest of the plate surface.

Quantity q_1 is defined as a function of the local surface temperature T_w and of the voltage drop U between the surrounding plasma and the plate, given by:

$$q_1 = q_i - q_{em} - q_{ev}, \quad (4.7)$$

where q_i is the density of the energy flux delivered to the metal surface by incident ions (generated from the vaporized atoms); q_{em} is the density of the energy flux due to electron emission; q_{ev} is the density of the energy flux due to emission of atoms. These quantities are evaluated as

$$q_i = \frac{j_{iw}}{e} (eU + A_i - A_f), \quad (4.8)$$

$$q_{em} = \frac{j_{em}}{e} (2kT_w + A_f), \quad (4.9)$$

$$q_{ev} = J_v (A_v + 2kT_w), \quad (4.10)$$

where j_{iw} is the density of current of ions coming to the metal surface, generated from the vaporized atoms and evaluated assuming that all emitted atoms are ionized and return to the surface, $j_{iw} = eJ_v$; j_{em} is the (field-enhanced thermionic) electron emission current density, evaluated by means of the Richardson-Dushman formula with the Schottky correction, with the surface electric field obtained from the Mackeown equation; e is the electron charge; A_i is the ionization energy; A_f is the work function (without the Schottky correction); A_v is the energy of vaporization per atom; k is the Boltzmann constant; and J_v is the flux of atoms emitted by the cathode surface, evaluated by means of the Langmuir formula $J_v = p_v / \sqrt{2\pi m_i k T_w}$, where p_v is the pressure of the saturated vapor of the plate metal and m_i is the mass of the ions formed from the metal vapor.

The density of electric current j_1 is defined as a function of T_w and U , and is given by:

$$j_1 = j_{iw} + j_{em}. \quad (4.11)$$

The pressure p_1 exerted by the plasma produced from the ionization of the emitted vapor is evaluated, as a function of T_w and U , by means of expression:

$$p_1 = \frac{2q_i}{\sqrt{2eU/m_i}}. \quad (4.12)$$

The quantity $\sqrt{2eU/m_i}$ has the meaning of speed of the ions impinging on the cathode surface estimated neglecting the kinetic energy of the ions at the sheath edge.

Quantity q_2 is specified as

$$q_2 = q_{\text{peak}} f_r(r) f_t(t), \quad (4.13)$$

where q_{peak} is a given parameter characterizing the maximum density of energy flux delivered by the external intense heat load; and $f_r(r)$ and $f_t(t)$ are functions characterizing the spatial distribution and temporal variation of the intense heat load and assumed in the form

$$f_r(r) = \exp\left[-\left(\frac{r}{a}\right)^2\right], \quad f_t(t) = \exp\left[-\left(\frac{t-t_0}{\tau}\right)^2\right], \quad (4.14)$$

where a , τ , and t_0 are given parameters.

Quantity j_3 is determined as

$$j_3 = j_i - j_e, \quad (4.15)$$

where

$$j_i = Zen_i \sqrt{\frac{ZkT_e}{m_i^{(\text{bp})}}}, \quad j_e = \frac{1}{4}en_e \sqrt{\frac{8kT_e}{\pi m_e}} \exp\left(-\frac{eU}{kT_e}\right). \quad (4.16)$$

Here n_i , n_e , Z and T_e are the ion and electron densities, the ion charge number, and the electron temperature in the background plasma (note that $n_e = Zn_i$), $m_i^{(\text{bp})}$ is the mass of an ion of the background plasma gas, and m_e is the mass of an electron. Quantities j_i and j_e in these equations represent the densities of electric currents of ions and electrons coming to the plate from the background plasma. The term $\sqrt{ZkT_e/m_i^{(\text{bp})}}$ in the first expression of equation (4.16) is the Bohm speed; in the second expression of (4.16), the term $\frac{1}{4}n_e \sqrt{\frac{8kT_e}{\pi m_e}}$ is the thermal flux of electrons and the factor $\exp\left(-\frac{eU}{kT_e}\right)$ takes into account repulsion of the electrons by the potential barrier. For evaluations, it is convenient to rewrite equation (4.15) as

$$j_3 = j_i \left[1 - \frac{1}{4} \sqrt{\frac{8m_i^{(\text{bp})}}{\pi Zm_e}} \exp\left(-\frac{eU}{kT_e}\right) \right]. \quad (4.17)$$

Quantity q_3 is specified as in [142], with some minor terms (those proportional to the ion temperature, the electron emission current density, and the Schottky correction) omitted:

$$q_3 = \frac{j_i}{e} \left[\frac{kT_e}{2} + eU + E - A_f + \frac{1}{4} \sqrt{\frac{8m_i^{(\text{bp})}}{\pi Zm_e}} \exp\left(-\frac{eU}{kT_e}\right) (2kT_e + A_f) \right], \quad (4.18)$$

where E is the average ionization energy.

Estimates based on the laser beam characteristics and of plasma parameters in typical experimental conditions show that the pressures p_2 and p_3 exerted by the external heat load and by the background plasma on the metal plate are negligible when compared to the pressure p_1 exerted by the plasma produced from the metal vapor. Therefore, the pressures p_2 due to the external heat load and p_3 due to the background plasma are neglected, and $p_{tot} = p_1$.

Quantity q_4 is given by the Stefan-Boltzmann law,

$$q_4 = \varepsilon \sigma T^4, \quad (4.19)$$

where σ is the Stefan-Boltzmann constant and ε is the emissivity of the plate surface.

All the above-described terms are taken into account in the boundary conditions at the face of the plate which is subjected to the external heat load. At all the other faces, q_1 , q_2 , and j_1 are dropped (and no boundary conditions for the Navier-Stokes equations are needed since these faces are not melted).

A characteristic of the unipolar arc is that the net current to the plate is zero. The variation of the plate potential, $U = U(t)$, is computed with this condition, i.e., the current transferred by the plasma produced in the spot I_1 is balanced by the current transferred by the background plasma over the whole surface of the plate. Since j_3 takes the same value at all points of the plate surface, this condition reads

$$I_1 = j_3 A_{\text{plate}}, \quad I_1 = \int j_1 dA, \quad (4.20)$$

where the integral is evaluated over the face subjected to the external heat load and A_{plate} is the total surface area of all faces of the plate.

The initial condition is $T = T_0$, where T_0 is the temperature of the plate while it is immersed in the background plasma before the laser pulse irradiation. T_0 is governed by the condition of equilibrium between the density of the energy flux q_3 delivered by the background plasma to the plate surface and the density of energy flux q_4 lost by the plate surface due to radiation into the plasma, i.e., $q_3 = q_4$.

The problem is solved numerically by means of the finite-element method. The enthalpy-porosity method [127, 128] is used for modeling the solid-liquid phase transition in the metal. The account of the latent heat of melting is introduced along the same lines as is done in simulation of metal casting [114]. A front-tracking method is implemented for explicitly tracking the deformation of the molten surface on a moving grid.

4.2.2 Material functions

The choice of conditions of modeling reported in this work is based on the experiment [75]. Let us consider a circular tungsten plate immersed in a helium background plasma and subjected on one side to an intense heat load from a laser. The plate thickness in the modeling is 0.2 mm; two values of the plate radius have been considered for the modeling, namely 10 mm and 10 cm. The model of this work does not take into account the nanostructure layer, since the nanostructures within the impact site of the intense heat load are rapidly destroyed and will have no effect on the initial stage of arcing, as evidenced by the estimates given in section 4.1 and by special simulations reported in subsection 4.4.2. Thus, the (temperature-dependent) mass density, specific heat, thermal conductivity, viscosity and surface tension coefficient are set equal to those of bulk tungsten and taken from [143]. The pressure of the saturated tungsten vapor p_v , a known function of the local temperature, is taken from [111]. The work function and the Richardson constant for tungsten were assumed to be equal equal to 4.55 eV and $60 \times 10^4 \text{ A/m}^2 \text{ K}^2$ [4, 111].

As an example, the computed values of q_1 , j_1 and p_1 are shown in figure 4.1 for two values of the voltage drop between the surrounding plasma and the plate of $U = 20 \text{ V}$ and $U = 30 \text{ V}$ in the range of surface temperatures T_w relevant to the simulations of this work. For low local surface temperatures, the production of the vapor and its ionization are negligible and q_1 , j_1 , and p_1 are virtually zero. A significant tungsten plasma production starts as the temperature increases up to approximately 4000 K and $(-q_1)$, j_1 , and p_1 rapidly grow. It is interesting to note that the density of the energy flux q_1 is negative in the whole range of temperatures shown, figure 4.1a. The reason is that as the surface temperature increases, so does the emission of electrons from the surface; in fact, electron emission cooling increases much faster than the heating due to ion bombardment, which means that the production of the tungsten plasma contributes to the cooling of the plate surface against the intense heating due to the external heat load. Furthermore, the density of electron emission current is also the dominant contribution to the density of electric current j_1 transferred in the spot, which reaches values of the order of 10^9 A/m^2 at $T_w = 5000 \text{ K}$, figure 4.1b. Note that while the emission of electrons from the surface is the dominant mechanism in the energy and current transfer to the plate surface, the pressure exerted due to ion bombardment is appreciable, of the order of 1 atm, and is sufficient to push the molten metal in the spot outward, as shown below.

The dotted lines in figure 4.1 show the results of evaluation by means of the model of near-cathode space-charge sheaths developed for vacuum arcs [62], based on numerical modeling of the near-cathode space-charge sheath with ionization of atoms vaporized

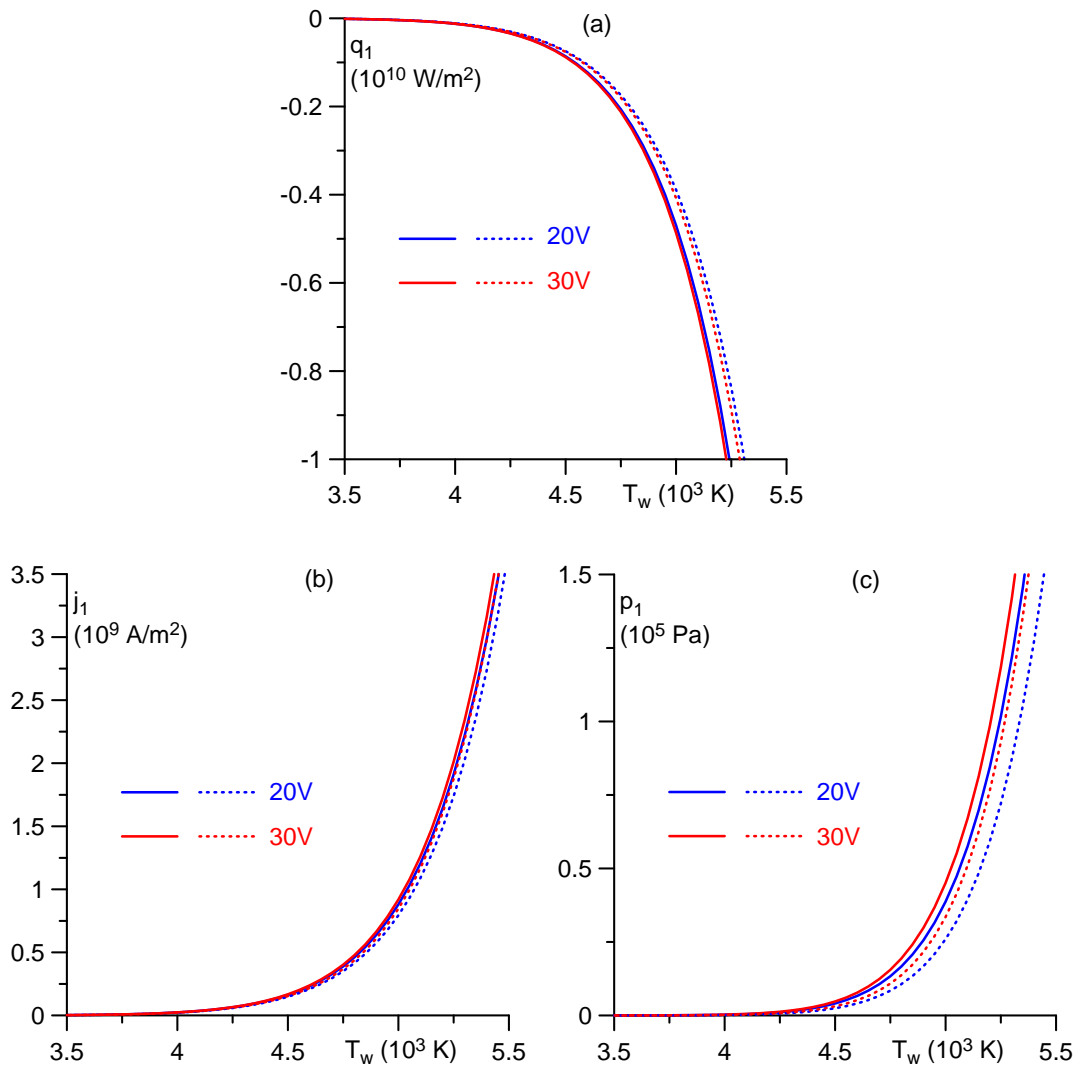


Figure 4.1: Computed values of q_1 , j_1 and p_1 . The solid lines represent values obtained with the model of this work. The dotted lines represent values obtained with the model of near-cathode space-charge sheaths developed for vacuum arcs [61, 62].

from the cathode surface [61], and employed in the modeling in chapters 2 and 3. One can see that there is little difference between the solid and dotted curves. Thus, the results given by equations (4.7), (4.11) and (4.12) do not differ significantly from those given by the more detailed description of the near-cathode layer [61, 62] and are sufficient for a qualitatively accurate description of the current transfer in the unipolar arc spot on the metal plate.

It is of interest to compare the above parameters of the near-cathode layer on a tungsten electrode with those of copper cathodes in vacuum arcs [62]. Quantities q_1 , j_1 and p_1 are overall several orders of magnitude higher for copper cathodes: the density of energy flux q_1 is positive for surface temperatures up to approximately 4300 K, since the ion heating exceeds the electron emission cooling, and is greater by up to 2 orders of magnitude; the density of electric current j_1 transferred in the spot and the pressure p_1 exerted by the plasma on the surface are up to 3 orders of magnitude higher. This difference arises due to the different natures of the two metals: copper is a volatile metal, while tungsten is a refractory metal with a significantly higher energy of vaporization per atom. The latter, in particular, leads to an increase of the temperature at which the metal starts being vaporized and ionized in the spot.

In the experiment [75], the laser pulse used to trigger the unipolar arc had a peak power of 10^{10} W/m^2 (which corresponds to that of ELMs expected in ITER), a pulse width of $\sim 0.6 \text{ ms}$, and a laser beam size at the impact site on the plate with a diameter of approximately 0.8 mm, when injected normal to the plate. In the modeling, the parameters q_{peak} , τ and t_0 of equations (4.13) and (4.14) are specified such that the density of the energy flux q_2 delivered by the external heat load to the surface has similar characteristics to the laser pulse used in the experiment: $q_{\text{peak}} = 10^{10} \text{ W/m}^2$, and $\tau = 0.3 \text{ ms}$. The temporal shift t_0 of the maximum is set equal to 5 ms. Two values of the parameter a are considered for simulations, $a = 0.1 \text{ mm}$ and $a = 0.4 \text{ mm}$.

The emissivity ε of tungsten, a known function of the local temperature, is taken from [144].

The helium ions of the background plasma in the conditions of experiment [75] are doubly ionized, so it was set $Z = 2$. The ionization energy E in equation (4.18) is set as 39.5 eV, which is the sum of the first and second ionization energies for helium, divided by Z .

In the experiment [75], the plate potential increases by approximately 30 V from the floating potential in response to the laser irradiation. Assuming 10 V as a typical value of the near-cathode voltage drop during arcing (i.e., the arc burning voltage), one comes to the conclusion that the floating potential is about 40 V, which corresponds to an electron temperature in the helium background plasma of about 13 eV. Thus, it was assumed $T_e = 13 \text{ eV}$. The initial temperature of the plate is set to $T_0 = 1900 \text{ K}$, a

value of the plate temperature immersed in the helium plasma before the laser pulse irradiation reported in [75]. The background plasma ion current density in equations (4.17), (4.18) was found by solving the equation $q_3 = q_4$ and turned out to be equal to $1.6 \times 10^3 \text{ A/m}^2$.

It should be stressed that the aim of the work of this chapter is to develop a simulation model of the initial stage of a unipolar arc and report illustrative modeling results, rather than simulate the particular experiment [75]. Accordingly, no attempt was made to perform simulations for exactly the same conditions as in [75]: the tungsten plate in the experiment [75] was square and not circular, the electron temperature in the background plasma mentioned in [75] was 6 eV *etc.*

4.3 Numerical results

Let us consider the results obtained by simulations in the framework of the model described above. Two sets of simulation conditions have been considered for the modeling of this section. Simulation 1 refers to a simulation with a plate radius of 10 mm, and the parameter a specifying the spatial variation of the external heat load equal to 0.1 mm. Simulation 2 refers to a simulation with a plate radius of 10 cm, and a equal to 0.4 mm.

The computed temporal evolution of the temperature distribution in the metal plate and of the plate surface deformation is shown in figure 4.2 for simulation 1, and in figure 4.4 for simulation 2. The temporal evolution of the plate potential U and of the maximum plate temperature T_{\max} are shown in figure 4.3a for simulation 1 and in figure 4.5a for simulation 2. The temporal evolution of the current transferred by the tungsten plasma in the spot is shown in figure 4.3b for simulation 1 and in figure 4.5b for simulation 2. The temporal evolution of the maximum pressure exerted by the produced tungsten plasma $p_{1,\max}$, and of the maximum velocity of the melt v_{\max} are shown in figure 4.3c for simulation 1 and in figure 4.5c for simulation 2.

The temporal evolution in the cases of simulation 1 and of simulation 2 occurs in essentially the same way. The external heat flux comes into play at, say, $t = 4.5 \text{ ms}$ (at this moment, $q_2 \approx 10\% q_{\text{peak}}$). The maximum plate temperature starts rapidly increasing and at approximately 4.7 ms melting of the surface begins, figures 4.2b and 4.4b. Simultaneously, the pressure exerted over the surface by the produced tungsten plasma grows, figures 4.3c and 4.5c, and pushes the molten metal outwards and at approximately 4.8 – 4.9 ms a crater begins forming, figures 4.2c and 4.4c. When the power delivered by the intense heat load is at maximum, which happens at 5 ms, the surface temperature attains a maximum of about 5100 K, figures 4.3a and 4.5a. Simultaneously, the plate potential is reduced from the floating potential to

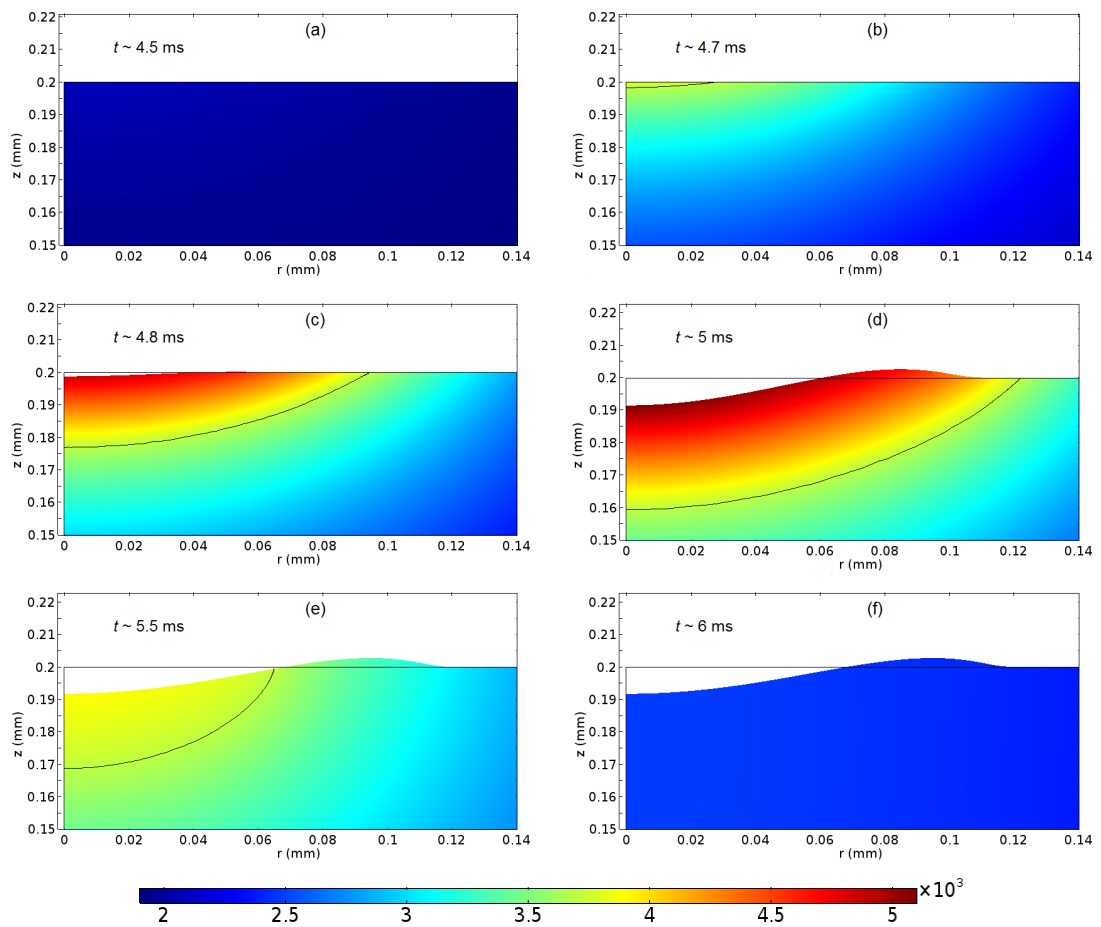


Figure 4.2: Evolution of the temperature distribution and plate surface deformation, in conditions of simulation 1. The bar in K. The black line represents the melting temperature isotherm.

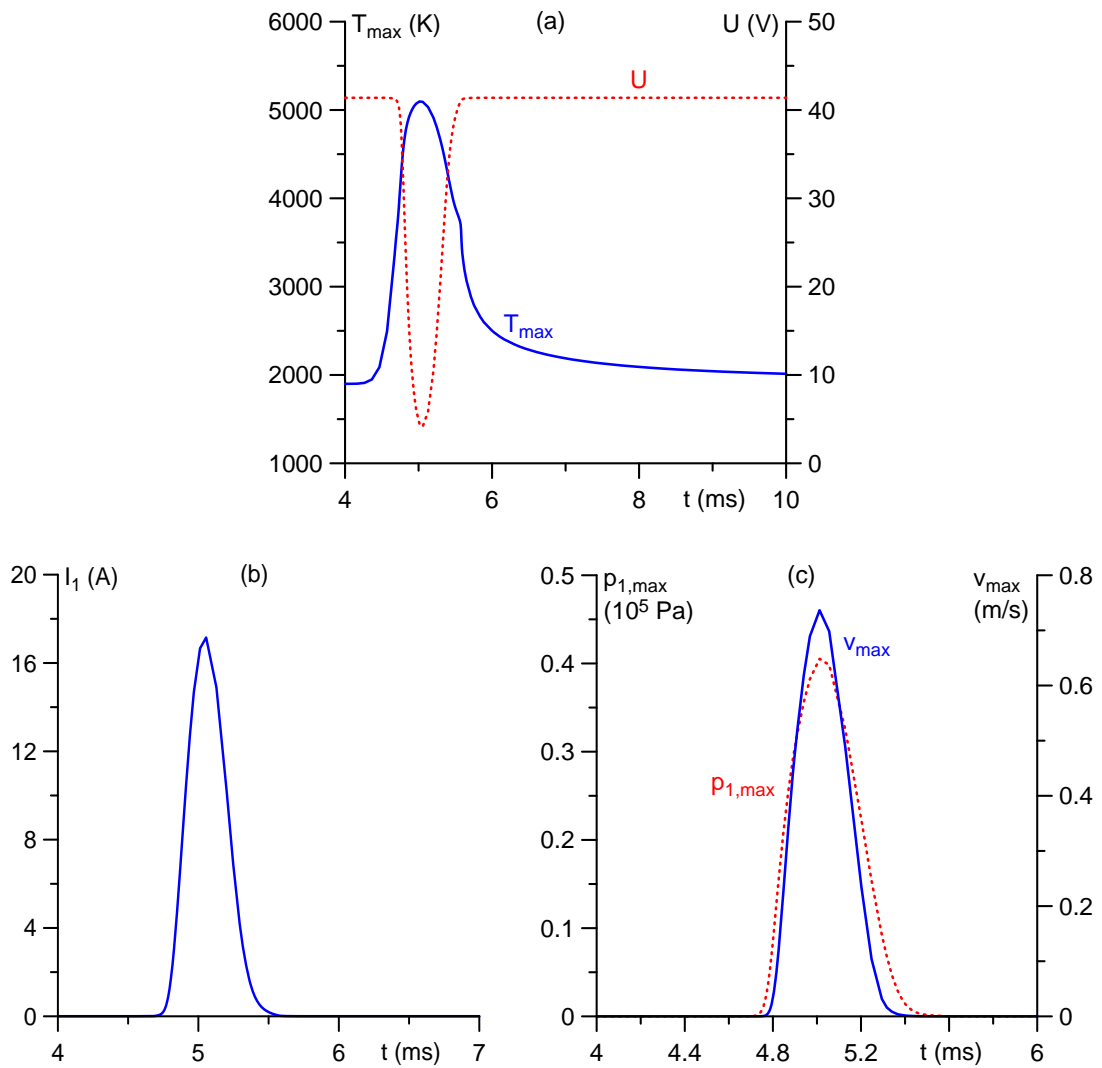


Figure 4.3: Results of simulation of the unipolar arc burning in tungsten vapor, in conditions of simulation 1. Temporal evolution of: (a) the plate potential and of the maximum plate temperature; (b) the current transferred by the tungsten plasma in the spot; (c) the maximum pressure exerted by the tungsten plasma and the maximum velocity acquired by the molten metal.

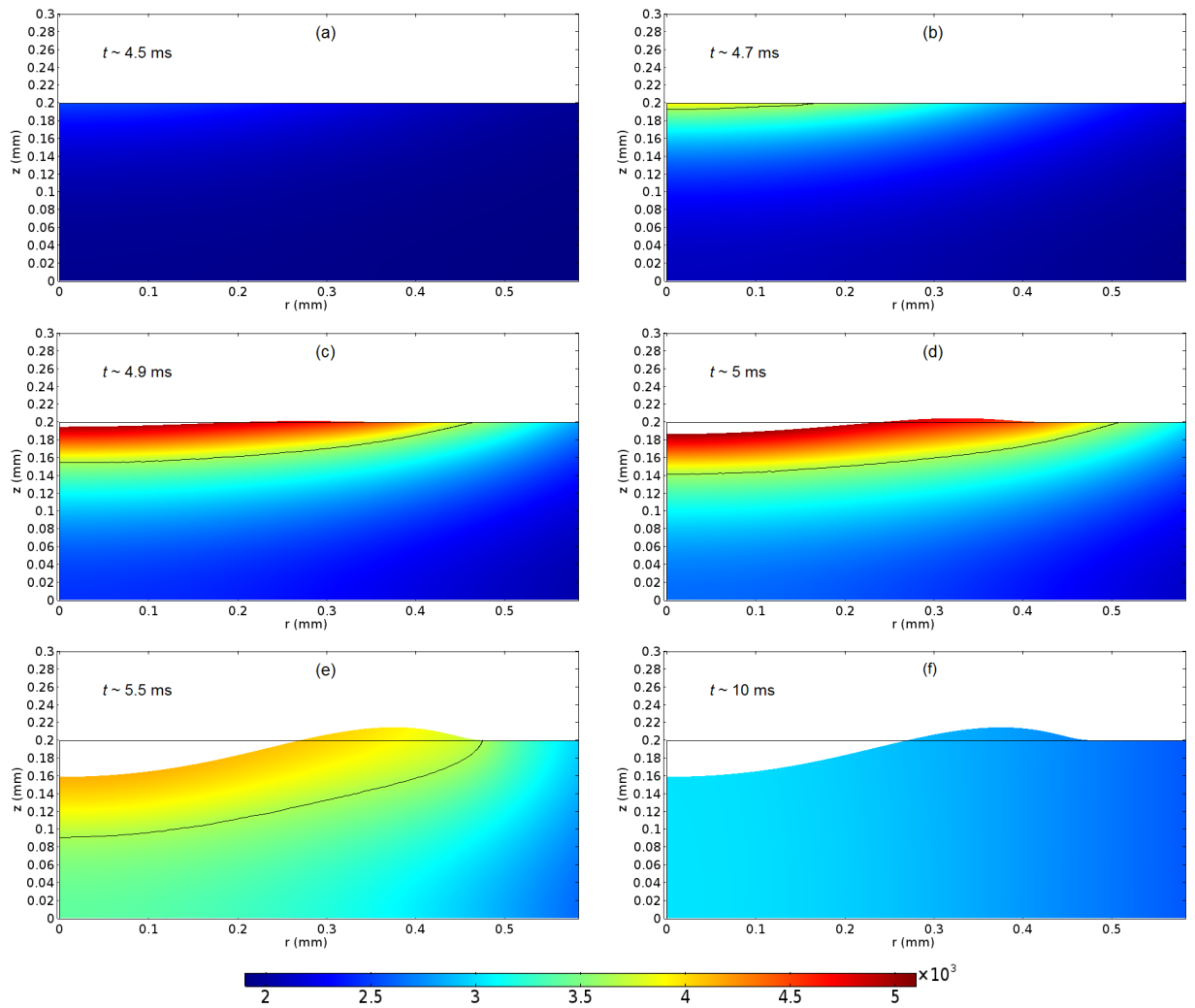


Figure 4.4: Evolution of the temperature distribution and plate surface deformation, in conditions of simulation 2. The bar in K. The black line represents the melting temperature isotherm.

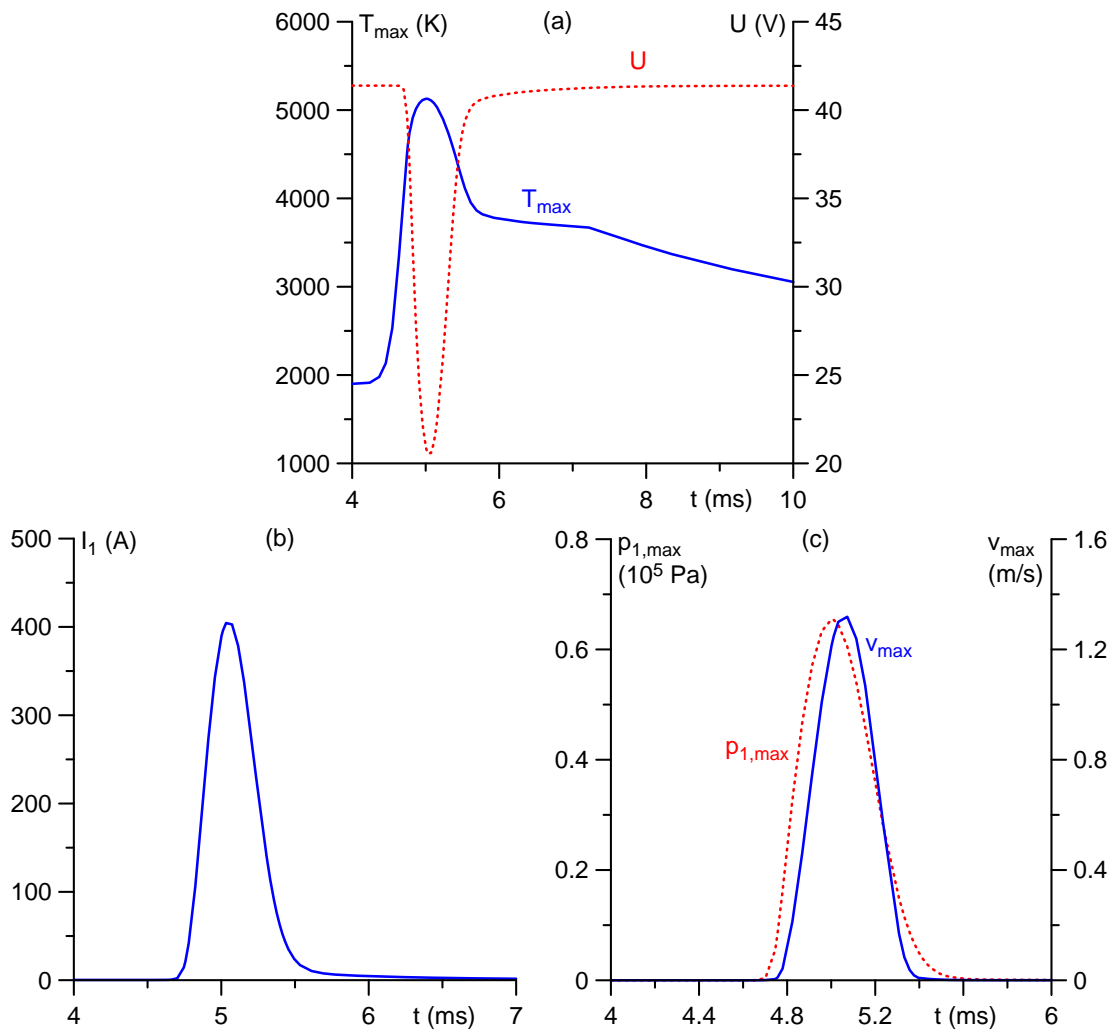


Figure 4.5: Results of simulation of the unipolar arc burning in tungsten vapor, in conditions of simulation 2. Temporal evolution of: (a) the plate potential and of the maximum plate temperature; (b) the current transferred by the tungsten plasma in the spot; (c) the maximum pressure exerted by the tungsten plasma and the maximum velocity acquired by the molten metal.

approximately 5 V in simulation 1, figure 4.3a, and to approximately 20 V in simulation 2, figure 4.5a. The formed crater expands on the plate surface (states (c) to (e) in figures 4.2 and 4.4), achieving a final depth of approximately 10 μm and a radius of approximately 60 μm in simulation 1, figure 4.2f, and a depth and radius of about 40 μm and 280 μm , respectively, in simulation 2, figure 4.4f. After the external irradiation has ceased at $t \approx 5.5$ ms, the temperature decays very quickly in simulation 1; in the case of simulation 2, the temperature decays quickly to a little less than 4000 K, and then remains approximately constant for nearly 2 ms (until $t \approx 7.5$ ms), after which the temperature decay resumes. No jet formation, or droplet detachment occurs in either case.

Let us now consider the above-described evolution in some detail. At first, the tungsten plate immersed in the background plasma receives equal fluxes of helium ions and electrons, such that the net current delivered to the surface is zero and the plate is at the floating potential, as shown by the horizontal section of the dependencies $U(t)$ in figures 4.3a and 4.5a and by the zero value of the current I_1 in figures 4.3b and 4.5b (since the current transported by the helium plasma equals I_1 , it is zero as well). As the plate surface starts being subjected to the external heat load at approximately 4.5 ms, the increase in the temperature results in the initiation of electron emission and vaporization of tungsten atoms with their subsequent ionization, i.e., the ignition of a spot. The transfer of current by the produced tungsten plasma is initiated. I_1 starts growing, figures 4.3b and 4.5b, and rapidly increases with the continued increase in temperature and with the expansion of the spot, shown by states (b) to (d) of figures 4.2 and 4.4. Furthermore, as the production of the tungsten plasma increases and the ionized atoms return to the surface, the pressure exerted on the surface by these ions starts growing as well, figures 4.3c and 4.5c, and pushes the molten material in the spot outward, with a velocity of about 0.7 m/s and 1.3 m/s, in simulations 1 and 2, respectively. A crater with a rim begins forming.

The ignition of the spot leads to a reduction of the potential difference U between the plasma and the plate, from the floating potential to the arc burning voltage of about 5 V and 20 V in simulations 1 and 2, respectively; figures 4.3a and 4.5a. This decrease allows a greater influx of electrons from the background plasma; the current transferred by the ions and the electrons of the background plasma from the surface of the plate into the plasma increases so as to balance the current I_1 transferred in the spot.

After the external heat load is switched off, the spot starts cooling down as heat is removed from the spot by heat conduction into the plate and the transfer of current in the spot rapidly decays, as well as the net current transferred by the helium plasma. The crater expansion stops, figures 4.2e and 4.4e, as the melt velocity quickly reduces

to zero. The plate potential returns to the floating potential. In the case of simulation 1, the surface temperature decays very quickly, within 0.5 ms, to a level slightly above 2000 K, after which the plate cools down further at a slower rate. In the case of simulation 2, after the initial rapid decrease, the surface temperature remains more or less constant for some time at a level slightly below 4000 K, after which the plate cools down further. Note that the net current transferred to the plate is zero at all stages of the simulation, as is characteristic of the unipolar arc [16].

4.4 Discussion

4.4.1 Comparison with spots in vacuum arcs

Estimates based on parameters used in the model of this chapter show that the pressure p_2 exerted by external source (laser beam) is approximately 33 Pa, and the pressure p_3 exerted by the helium background plasma ions is 6 Pa. One can see from figures 4.3c and 4.5c that the initial assumption that the pressure p_1 exerted over the plate surface by the ions produced from the vaporization of atoms from the plate surface dominates over the other terms in p_{tot} is valid, and $p_{tot} \approx p_1$. Furthermore, a comparison with results of the modeling of cathode spots in vacuum arcs of chapter 3 shows that the pressure due to the tungsten plasma is up to 3 orders of magnitude lower than the plasma pressure of up to 0.38 GPa in the modeling of vacuum arcs. This explains why the maximum velocities of approximately 0.7 m/s and 1.3 m/s, computed in the modeling of this chapter and seen in figures 4.3c and 4.5c, are significantly smaller than the velocity of up to 180 m/s in the modeling of vacuum arcs (cf. figure 3.10b of subsection 3.3.3, in chapter 3). As a consequence, the maximum velocity acquired by the molten metal in the modeling of this chapter is insufficient to drive the formation of liquid-metal jets at the crater periphery.

The plateau in the temporal evolution of the maximum temperature in the case of simulation 2, seen in figure 4.5a, is seemingly similar to the plateau in the modeling of cathode spots in vacuum arcs reported in chapters 2 and 3, which is also a feature known from the modeling of cathode spots in arcs in high-pressure ambient gases [60]. However, the physics responsible for the plateau in the modeling of this work is different. In the modeling of chapters 2 and 3, the plateau is owed to a balance between the heating due to ion bombardment and electron emission cooling. In the modeling of this chapter, quantity q_1 is negative in the whole range of the temperatures in the plate, which means that electron emission cooling is always greater than the heating due to ion bombardment. When the external heat load is switched off, at first, there is a fast decrease of the surface temperature due to strong electron emission cooling.

As T_{\max} decreases, the cooling due to electron emission is reduced significantly. The plate continues to cool down due to heat conduction into the bulk, but since the latter is a less intense mechanism compared to electron emission cooling, the plateau in the temporal evolution of the temperature appears, figure 4.5a. Eventually, the crater solidifies completely and the thermal conductivity almost doubles: the plate temperature continues decaying further at a faster rate.

4.4.2 Effect of the nanostructure layer

In the experiment [75], the tungsten plate is initially exposed for 30 min to the helium plasma, the consequence of which is the formation of a fine layer of nanostructures with a height of about $1.5 \mu\text{m}$. The estimates cited in section 4.1 have shown that such nanostructures are rapidly destroyed when subjected to the external heat load and can hardly affect the initial stage of unipolar arcing. In order to verify these estimates, special simulations have been undertaken.

A circular calculation domain representing the nanostructure layer is introduced directly above the circular tungsten plate, with the same radius and a height of $1.5 \mu\text{m}$. The mass density and thermal conductivity of this layer are known to be significantly different from those of bulk tungsten; according to the experiments [94, 96], the mass density is reduced to approximately 10% of that of bulk tungsten, while the thermal conductivity becomes 1% or less of that of bulk tungsten. Thus, the (temperature dependent) mass density ρ_{layer} and the thermal conductivity κ_{layer} of the nanostructure layer were set to $\rho_{\text{layer}} = 0.1\rho$ and $\kappa_{\text{layer}} = 0.01\kappa$ in the simulations reported in this section. Furthermore, κ_{layer} is assumed to be anisotropic, since the nanostructures are known to be extremely thin. The other material properties (specific heat, viscosity and surface tension coefficient) remain unchanged, as well as all other parameters and material functions described in subsection 4.2.2. Note that, as the nanostructure layer is heated to the melting temperature T_{melt} and begins melting, the distinction between this layer and the bulk of the plate disappears, so the properties ρ_{layer} and κ_{layer} are those of bulk tungsten for temperatures above T_{melt} .

Results of simulations performed with the account of the nanostructure layer in the case of conditions of simulation 2 are shown in figures 4.6 and 4.7. The temporal evolution of the temperature field differs only at the beginning: the hot layer is much thinner, figures 4.6a and 4.6b; and the maximum plate temperature is slightly higher, figure 4.7. Of course, these differences are due to the reduced thermal conductivity of the nanostructure layer.

At approximately 4.6 – 4.7 ms, points on the plate surface start reaching the melting temperature, the nanostructure layer starts being destroyed and the differences

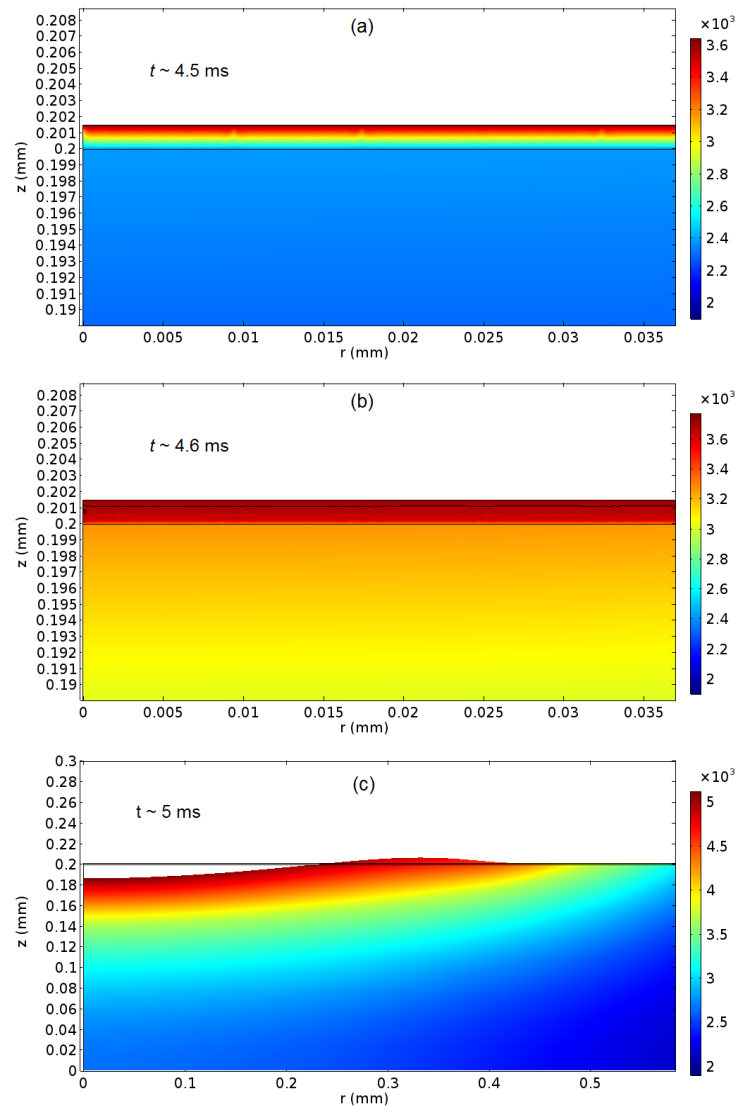


Figure 4.6: Evolution of the temperature distribution and plate surface deformation. The model takes into account the nanostructure layer. The bar is in K. (a), (b) The heated nanostructure layer is shown in detail. (b) The black line represents the melting temperature isotherm. (c) Global overview of the forming crater.

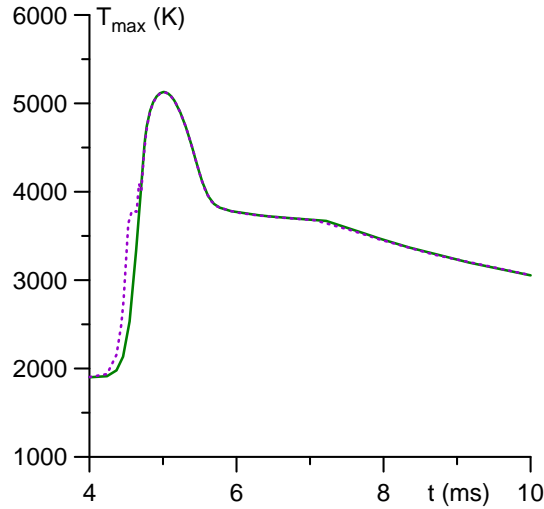


Figure 4.7: Temporal evolution of the maximum plate temperature in conditions of simulation 2. Dotted: model with account of the nanostructure layer. Solid: model without account of the nanostructure layer (from figure 4.5a).

between the layer and the bulk tungsten plate disappear within a few microseconds. The nanostructure layer does not have an influence in the melting or deformation of the surface: figure 4.6c coincides with figure 4.4d, and the subsequent distributions are also identical and skipped for brevity. The formed crater is identical to that of the modeling results shown in figure 4.4. The dependence $T_{\max}(t)$ coincides with that from the modeling of section 4.3, as shown in figure 4.7.

The simulations performed with the account of the nanostructure layer in the case of conditions of simulation 1, yield similar results. Thus, the effect of the nanostructure layer is negligible due to its rapid destruction, in agreement with the estimates in section 4.1, and the neglect of the nanostructures in the modeling of the initial stage of unipolar arcing is justified.

4.4.3 Space-charge limited electron emission current

In the experiment [75], the tungsten plate used was square, with a length, width and thickness of 20 mm, 20 mm and 0.2 mm, respectively. Furthermore, the laser pulse used to trigger the unipolar arc had a peak power of 10^{10} W/m², a pulse width of ~ 0.6 ms, and a laser beam size at the impact site on the plate with a diameter of approximately 0.8 mm, when injected normal to the plate. Note that, in conditions of simulation 1, the dimensions of the plate are similar to those of the experiment but the radial extension of the external heat load is significantly smaller, while in conditions of simulation 2, the parameters of the external heat load are similar to those of the

laser in the experiment, but the plate is much larger.

A third set of simulation conditions is considered in this section, namely with a plate of radius 10 mm, and the spatial variation a of the external heat load equal to 0.4 mm, i.e., parameters of the plate and of the external heat load similar to those of the experiment [75]. Let us analyze the current transfer by the produced tungsten plasma, and by the helium background plasma in such conditions.

The current transferred by the produced tungsten plasma is dependent on the heated surface area of the plate at the impact site of the external heat load, or in other words, on the size of the spot formed. It can be seen from the results of the previous simulations (section 4.3) that the latter is closely related to the spatial extension over the plate surface of the external heat load, i.e., the spot and crater size during the simulation are determined by the parameter a . Thus, it is clear that the expected temporal variation of the current I_1 transferred by the tungsten plasma in the spot will be similar to that of figure 4.5b.

The current transferred by the helium background plasma over the whole surface of the plate is governed by the dimensions of the plate (cf. equation (4.20) in subsection 4.2.1). In the conditions under consideration, the dependence of the current I_3 transferred by the helium background plasma over the whole surface area of the plate on the voltage drop U between the surrounding plasma and the plate is shown in figure 4.8; assuming 5 – 10 V as a typical value of the arc burning voltage (as in the model of this work), one can see from figure 4.8 that the corresponding current transferred by the helium background plasma will be approximately 10 to 15 A.

The above analysis reveals that a limitation of the current transferred in the spot by the produced tungsten plasma should be introduced in the model of this work, more specifically, an account of the limitation of the thermionic electron emission current by the space-charge accumulated in the near-cathode layer. In other words, the electric field at the plate surface appearing in the Richardson-Dushman formula with the Schottky correction employed in the modeling will be affected not only by the ions in the sheath, but also by the emitted electrons, which are significant due to tungsten being a refractory metal. This will have the effect of limiting the current transferred in the spot, so as to ensure that it will be balanced by the current transferred by the helium background plasma and that the net current transferred to the plate is zero at each moment.

A possible approach to an inclusion of an account of the space-charge limited thermionic electron emission in the modeling is based on the work [145], where a model is proposed and an expression for the electric field at the cathode surface has been derived, which takes into account the effect of not only the ions in the sheath, but also of the thermionic (emitted) and the plasma electrons.

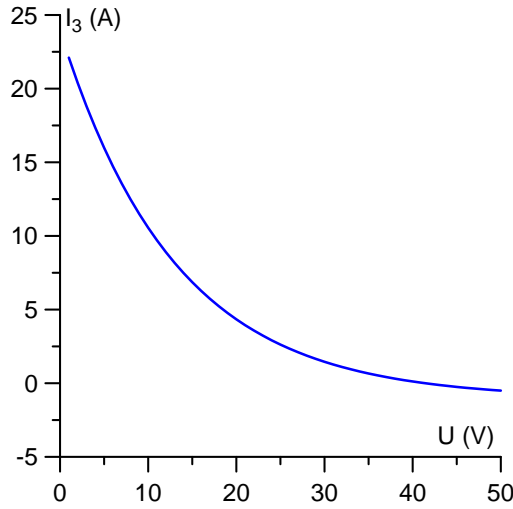


Figure 4.8: Dependence of the current I_3 transferred by the helium background plasma on the voltage drop U between the surrounding plasma and the plate. Plate radius of 10 mm.

4.5 Summary and concluding remarks

The detailed numerical model developed in chapter 3 for the modeling of plasma-cathode interaction in vacuum arcs has been used to investigate the initial phase of unipolar arcing. The interaction of an intense heat flux with and current transfer to a tungsten metal plate immersed in a helium background plasma in conditions based on the experiment [75] is simulated. The model takes into account an external energy source (the laser beam), which delivers the intense heat load to trigger the arcing, the vaporization of the tungsten atoms at the laser impact site, the ions and electrons produced by ionization of the vapor and the electron emission from the metal surface, and relevant hydrodynamic phenomena, including convection and surface deformation. The arc is unipolar, so the model of chapter 3 has been supplemented with an account of current transfer outside the arc attachment and the arc voltage is evaluated from the condition that the net current to the plate is zero at each moment.

The results revealed the formation of a crater, but no jet formation or droplet detachment. The latter is explained by significantly lower melt velocities in the conditions studied, when compared to those of cathode spots in vacuum arcs, which are much more extreme. As the plate surface starts being subjected to the external heat load, the increase in the temperature results in the initiation of electron emission and vaporization of tungsten atoms with their subsequent ionization, i.e., the ignition of a spot. The transfer of current by the produced tungsten plasma is initiated. The plate surface is rapidly heated up to 5100 K, attained at 5 ms when the power of the

delivered heat load is at maximum. The ignition of the spot leads to a reduction of the potential difference U between the plasma and the plate, from the floating potential to the arc burning voltage. After the external heat load is switched off, the spot cools down as heat is removed from the spot by heat conduction into the plate. The transfer of current in the spot rapidly decays to zero and the spot is extinguished. The plate potential returns to the floating potential. The net current transferred to the plate is zero at all stages of the simulation, as is characteristic of the unipolar arc. It was found that the nanostructure layer has a negligible effect due to its rapid destruction under the intense heat load.

Simulations of the initial phase of unipolar arcing were performed for different sets of conditions. It was found that, in the conditions of the experiment [75] concerning the plate dimensions and the laser beam parameters, the model needs to be modified: an account of the limitation of thermionic electron emission current by the space-charge accumulated in the near-cathode layer must be introduced. In other words, the electric field at the plate surface appearing in the Richardson-Dushman formula with the Schottky correction employed in the modeling will be affected not only by the ions in the sheath, but also by the emitted electrons, which are significant due to tungsten being a refractory metal.

Chapter 5

Conclusions of the thesis

A comprehensive numerical model of individual cathode spots in vacuum arcs has been developed for the first time. The model takes into account all the potentially relevant mechanisms governing the physics of cathode spots: the bombardment of the cathode surface by ions coming from a pre-existing plasma cloud; vaporization of the cathode material in the spot, its ionization, and the interaction of the produced plasma with the cathode; Joule heat generation in the cathode body; melting of the cathode material and motion of the melt under the effect of the plasma pressure and Lorentz force; the change in shape of the cathode surface; the formation of craters and liquid-metal jets; the detachment of droplets.

In order to identify effects of different mechanisms, an investigation of the thermal development of an individual cathode spot neglecting the hydrodynamic aspects was performed. The results of the modeling allow a natural identification of the phases of life of the individual spot: the ignition, the expansion over the cathode surface, and the thermal explosion or destruction by heat removal into the bulk of the cathode due to thermal conduction. Furthermore, it was found that the cathode surface temperature is limited to 4700 – 4800 K; this is the surface temperature at which the heating of the cathode surface, due to bombardment by the ions originating in the leftover plasma cloud and by the ions produced in the ionization of atoms vaporized from the surface, is balanced by the cooling of the cathode surface due to electron emission. This remarkable feature is known from the modeling of cathode spots in arcs in high-pressure ambient gases and manifests itself as a plateau in the temporal evolution of the maximum temperature in the cathode.

The above results remain applicable when the account of the hydrodynamic phenomena is introduced in the model, with the exception of the development of thermal runaway. In the framework of the full model, the ignition phase is characterized by a rapid increase of the cathode temperature up to 4700 – 4800 K, with a duration

of approximately 5 ns on the cathode with the microprotrusion and 8 ns on the planar cathode. The subsequent expansion phase is characterized by the plateau in the temporal evolution of the maximum cathode temperature and an increase in the spot current. A crater is formed due to the displacement of the molten metal from the center of the spot due to the pressure exerted by the plasma. After the leftover plasma cloud has been extinguished, the crater expansion stops and the spot starts being rapidly destroyed by heat removal into the bulk of the cathode due to thermal conduction. However, at this stage, the melt velocity is quite high, leading to the formation of a liquid-metal jet under the effect of fluid inertia, i.e., this stage may be called the jet development phase, which culminates in the detachment of the head of the jet in the form of a droplet.

The cathode temperature remains limited also in the framework of the comprehensive model, as a consequence of not only the cooling due to electron emission, but also due to convective heat transfer. If the latter mechanism is discarded, then the Joule heating becomes sufficient to initiate the thermal runaway inside the cathode body and the temperature will reach the critical temperature of copper. If the contribution of the plasma produced in the spot (and the electron emission cooling) is discarded, similar to works [53–56], the critical temperature is attained as well (although in this case the achievement of the critical temperature is simply due to heating by an external source rather than due to the development of thermal runaway). Furthermore, the neglect of the pressure exerted by the plasma produced in the spot leads to the complete solidification of the formed metal jet before the detachment of a droplet can occur.

It was found that for typical conditions of cathode spots in vacuum arcs the effect of the self-induced magnetic field on the formation of the liquid-metal jet and droplet detachment is negligible, even when (artificially) enhanced by a factor of 10. The self-induced magnetic seems to be hardly relevant for the retrograde motion of cathode spots, and the first-principle understanding of the retrograde motion is still lacking.

The modeling results conform to estimates of different mechanisms of cathode erosion, derived from experimental data on the net and ion erosion of copper cathodes of vacuum arcs. The loss of mass of the cathode due to vaporization is virtually compensated by the return of the vaporized atoms in the form of ions, so the dominant erosion mechanism is the ejection of liquid droplets, partially compensated by ion flux from the plasma cloud. The emitted droplets are partially vaporized in the near-cathode region. The produced vapor is ionized and a part of the ions move away from the cathode with the plasma jet. The rest of the ions remain in the near-cathode region and thus form a new plasma cloud, which will eventually ignite the next spot.

The modeling of this work could have, in principle, confirmed the physical picture

of the ecton concept described in section 1, since all relevant mechanisms are taken into account. However, no explosions have been observed in the conditions considered in this work; there is no appreciable effect of the pre-existing μm -size protrusion; craters are formed and droplets detach without an explosion; and even without an explosion, the ejected material and the energy deposited in the plasma are sufficient to instigate the formation of a new plasma cloud that will ignite a subsequent spot.

The model developed for the modeling of the plasma-cathode interaction in vacuum arcs was also employed in the investigation of the initial stage of unipolar arcing in fusion-relevant conditions. Appropriate modifications were introduced, in particular an account of the current transfer outside the arc attachment and the evaluation of the arc voltage from the condition of the net current transferred to the metal surface being zero at each moment. The interaction of an intense heat flux with and current transfer to a tungsten metal plate immersed in a helium background plasma was studied. The results revealed the formation of a crater, but no jet formation or droplet detachment. The latter is explained by significantly lower melt velocities in the conditions studied, when compared to those of cathode spots in vacuum arcs, which are much more extreme. As the plate surface starts being subjected to the external heat load, the increase in the temperature resulted in the initiation of electron emission and vaporization of tungsten atoms with their subsequent ionization, i.e., the ignition of a spot. The transfer of current by the produced tungsten plasma was initiated. The ignition of the spot leads to the reduction of the potential difference between the plasma and the plate, from the floating potential to the arc burning voltage, in accordance with [16]. After the external heat load is switched off, the spot cools down as heat is removed from the spot by heat conduction into the plate. The transfer of current in the spot rapidly decays to zero and the spot is extinguished. The plate potential returns to the floating potential. The net current transferred to the plate is zero at all stages of the simulation, as is characteristic of the unipolar arc. It was found that the nanostructure layer has a negligible effect due to its rapid destruction under the intense heat load.

Simulations of the initial phase of unipolar arcing were performed for different sets of conditions. The first set of conditions refers to dimensions of the plate similar to those of the experiment and a radial extension of the external heat load smaller than the laser beam diameter used in the experiment. In the second set of simulation conditions, the parameters of the external heat load are similar to those of the laser in the experiment, and the plate is significantly larger than that of the experiment. In the third case, both the dimensions of the plate and the parameters characterizing the external heat load are similar to those of the experiment. It was found that, in the latter case, the model needs to be modified: an account of the limitation of thermionic

electron emission current by the space-charge accumulated in the near-cathode layer must be introduced. In other words, the electric field at the plate surface appearing in the Richardson-Dushman formula with the Schottky correction employed in the modeling will be affected not only by the ions in the sheath (as was done in the modeling of this work), but also by the emitted electrons, which are significant due to tungsten being a refractory metal.

One could think of the following directions of the future work, among others. In the case of the plasma-cathode interaction in vacuum arcs, a natural and relevant step would be to move to 3D modeling. That would allow one to take into account that in real experimental situations, neither the leftover plasma cloud nor protrusions on the surface of the cathode are axially symmetric, as is assumed in the present modeling. Another effect that can be described by means of a 3D modeling is the development of hydrodynamic instabilities and how the latter would affect the development of the jets and the detachment of droplets. As far as the plasma-cathode interaction in unipolar arcs is concerned, one of the important questions to address is that above-discussed; a possible approach to an inclusion of an account of the space-charge limited thermionic electron emission in the modeling is based on the work [145].

Vacuum and unipolar arcs are only two examples of discharges that may be studied with the model developed in this thesis; one can hope that the model may also be used, with appropriate modifications, for investigation of plasma-electrode interaction and crater formation in discharges of other types, for instance, ignition discharges in spark plugs (e.g., [146–152] and references therein) and discharges between electrodes in liquids (e.g., [153, 154] and references therein).

Appendix A

Equation of state

The microexplosion scenario on the cathode of a vacuum arc has a number of features in common with the electrical explosion of wires. A routine approach to modeling of the wire explosion is based on the use of 1D magnetohydrodynamic simulations with an equation of state (EOS) of the metal for a wide range of temperatures and pressures; e.g., [155–158]. Similar wide-range EOS are used in the models of vacuum arc-cathode interaction assuming a continuous metal-plasma transition without an interface [46, 48, 159]. The approach to the modeling of cathode spots employed in chapters 2 and 3 does not assume a continuous metal-plasma transition nor do the modeling results reveal microexplosions, but the question as to whether a wide-range EOS should be implemented is still relevant.

Lines in figure A.1 represent isotherms of copper given by the wide-range EOS of copper [160] for several temperature values below the critical temperature (8390 K). The data were provided by the Group T-1 at the Los Alamos National Laboratory with the use of the SESAME EOS Library [161] maintained by the group. Three branches are identifiable: the gas state branch at low mass densities, which coincides with the ordinate axis; the liquid state branch at high mass densities; and the vapor-liquid equilibrium branch at intermediate mass densities (the liquid and gas phases coexist at equilibrium and variations of volume occur at a constant pressure).

The simulations of chapters 2 and 3 reveal that the maximum temperature T_{\max} in the cathode is limited to approximately 4700 – 4800 K. One can see in figure A.1 that in this temperature range and in the relevant pressure range (up to 1 GPa; cf. figure 3.2 in chapter 3) the dependence of the mass density of liquid copper on pressure is weak. The dependence on temperature is more appreciable, although not very significant: ρ decreases from 8000 kg/m³ at low temperatures to approximately 6000 kg/m³ at high temperatures.

Thus, an accurate equation of state for a wide range of temperatures and pressures

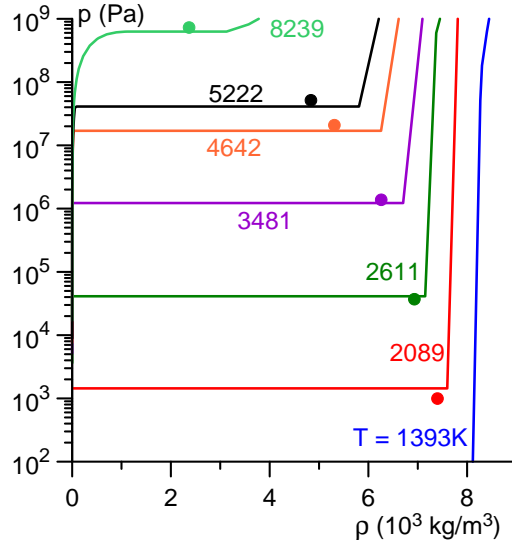


Figure A.1: Lines: data on the equation of state for copper [160]. Points: mass density of liquid copper evaluated by means of a fit formula with the use of data [115, 116] and saturated vapor pressure evaluated by means of the formula [109].

is not critical for the modeling of cathode spots performed in chapters 2 and 3: it is sufficient to take into account the variation of the mass density of liquid copper with temperature. In the modeling of chapters 2 and 3, the function $\rho(T)$ was evaluated with the use of data from [115–117] as in subsection 2.2.2.

It is of interest to compare values given by the above-mentioned function $\rho(T)$ with the data given by the wide-range EOS of copper [160] and shown in figure A.1. Furthermore, it is appropriate to also compare the latter data with those given by the formula [109] for the saturated vapor pressure of copper, used in the model of near-cathode plasma layers in vacuum arcs developed in [62] and employed in the work of chapters 2 and 3. This comparison is illustrated by the points in figure A.1: the abscissas of these points represent values of the function $\rho(T)$ and the ordinates represent the saturated vapor pressure evaluated by means of the formula [109]. (Note that the vapor pressure of copper given by the formula [109] for $T = 8390$ K, 0.79 GPa, is close to the pressure at the critical point of copper given in [117], which is 0.75 GPa.) One can see that the data used in this work do not deviate greatly from the EOS data [160].

Bibliography

- [1] Yu. P. Raizer, *Gas Discharge Physics* (Springer, Berlin, 1991).
- [2] R. L. Boxman, in *Handbook of Vacuum Arc Science and Technology: Fundamentals and Applications*, edited by R. L. Boxman, D. M. Sanders, and P. J. Martin (Noyes Publications, Park Ridge, N.J., U.S.A., 1995) pp. 3–27.
- [3] B. Jüttner, *J. Phys. D: Appl. Phys.* **34**, R103 (2001).
- [4] A. Anders, *Cathodic Arcs: From Fractal Spots to Energetic Condensation*, Springer Series on Atomic, Optical, and Plasma Physics (Springer, New York, 2008).
- [5] R. L. Boxman, D. M. Sanders, and P. J. Martin, eds., *Handbook of Vacuum Arc Science and Technology: Fundamentals and Applications* (Noyes Publications, Park Ridge, N.J., U.S.A., 1995).
- [6] J. M. Lafferty, ed., *Vacuum Arcs: Theory and Application* (Wiley, New York, 1980).
- [7] P. G. Slade, *The Vacuum Interrupter: Theory, Design, and Application* (CRC Press, 2008).
- [8] M. Lisnyak, *Theoretical, numerical and experimental study of dc and ac electric arcs*, Ph.D. thesis, GREMI, Université d’Orléans (2018).
- [9] J. F. Lancaster, ed., *The Physics of Welding*, 2nd ed. (Pergamon Press, 1986).
- [10] A. J. Shirvan and I. Choquet, *Weld. World* **60**, 821 (2016).
- [11] A. J. Shirvan, *Modelling of cathode-plasma interaction in short high-intensity electric arc: application to gas tungsten arc welding*, Ph.D. thesis, Chalmers University of Technology, Gothenburg, Sweden (2016).
- [12] J. F. Waymouth, *Electrical Discharge Lamps* (MIT Press, Cambridge, MA, 1971).

- [13] K. Günther, in *Low Temperature Plasma Physics: Fundamental Aspects and Applications*, edited by R. Hippler, S. Pfau, S. Martin, and K. H. Schoenbach (Wiley-VCH Verlag Berlin GmbH, 2001) pp. 407–431.
- [14] Y. V. Tsvetkov, in *Thermal Plasma and New Materials Technology*, Vol. 2, edited by O. P. Solonenko and M. F. Zhukov (Cambridge Interscience Publishing, Cambridge, 1995) pp. 292–323.
- [15] S. F. Paul, in *Proceedings of the International School of Plasma Physics "Piero Caldirola", Varenna, Italy, Sept. 1995*, edited by R. Benocci, G. Bonizzoni, and E. Sindoni (World Scientific Publishing, Singapore, 1996) pp. 67–86.
- [16] A. E. Robson and P. C. Thonemann, *Proc. Phys. Soc.* **73**, 508 (1959).
- [17] R. Behrisch, in *Physics of Plasma-Wall Interactions in Controlled Fusion (NATO ASI Series, Series B: Physics)* (Plenum Press, New York, 1986) pp. 495–513.
- [18] G. Ecker, *Ergeb. Exakten Naturwiss.* **33**, 1 (1961).
- [19] G. A. Mesyats, *J. Nucl. Mater.* **128-129**, 618 (1984).
- [20] I. I. Beilis, *IEEE Trans. Plasma Sci.* **29**, 657 (2001).
- [21] M. S. Benilov, *Plasma Sources Sci. Technol.* **11**, A49 (2002).
- [22] E. Hantzsche, *IEEE Trans. Plasma Sci.* **31**, 799 (2003).
- [23] G. A. Mesyats, *Plasma Phys. Control. Fusion* **47**, A109 (2005).
- [24] M. S. Benilov, *J. Phys. D: Appl. Phys.* **41**, 144001 (30pp) (2008).
- [25] G. A. Mesyats, *IEEE Trans. Plasma Sci.* **41**, 676 (2013).
- [26] R. Kh. Amirov, N. A. Vorona, A. V. Gavrikov, G. D. Liziakin, V. P. Polistchook, I. S. Samoylov, V. P. Smirnov, R. A. Usmanov, and I. M. Yartsev, *Plasma Phys. Rep.* **41**, 808 (2015).
- [27] M. S. Benilov and L. G. Benilova, *IEEE Trans. Plasma Sci.* **43**, 2247 (2015).
- [28] V. F. Puchkarev, in *Handbook of Vacuum Arc Science and Technology: Fundamentals and Applications*, edited by R. L. Boxman, D. M. Sanders, and P. J. Martin (Noyes Publications, Park Ridge, N.J., U.S.A., 1995) pp. 256–264.
- [29] A. Batrakov, S. Popov, N. Vogel, B. Juettner, and D. Proskurovsky, *IEEE Trans. Plasma Sci.* **31**, 817 (2003).

-
- [30] A. Anders, E. M. Oks, G. Y. Yushkov, K. P. Savkin, I. G. Brown, and A. G. Nikolaev, *IEEE Trans. Plasma Sci.* **33**, 1532 (2005).
- [31] A. M. Chaly and S. M. Shkol'nik, *IEEE Trans. Plasma Sci.* **39**, 1311 (2011).
- [32] S. Jia, Z. Shi, and L. Wang, *J. Phys. D: Appl. Phys.* **47**, 403001 (2014).
- [33] G. A. Mesyats and S. A. Barengol'ts, *Annu. Rev. Fluid Mech.* **45**, 1001 (2002).
- [34] S. P. Bugaev, E. A. Litvinov, G. A. Mesyats, and D. I. Proskurovsky, *Sov. Phys. Usp.* **18**, 51 (1975).
- [35] G. A. Mesyats, *IEEE Trans. Plasma Sci.* **23**, 879 (1995).
- [36] E. Hantzsche, *Beitr. Plasmaphys.* **14**, 135 (1974).
- [37] J. Prock, *IEEE Trans. Plasma Sci.* **14**, 482 (1986).
- [38] J. Mitterauer and P. Till, *IEEE Trans. Plasma Sci.* **15**, 488 (1987).
- [39] M. S. Benilov, *Phys. Rev. E* **48**, 506 (1993).
- [40] T. Klein, J. Paulini, and G. Simon, *J. Phys. D: Appl. Phys.* **27**, 1914 (1994).
- [41] I. I. Beilis, *Appl. Phys. Lett.* **97**, 121501 (2010).
- [42] I. I. Beilis, *IEEE Trans. Plasma Sci.* **41**, 1979 (2013).
- [43] D. L. Shmelev and S. A. Barengol'ts, *IEEE Trans. Plasma Sci.* **41**, 1959 (2013).
- [44] M. S. Benilov, *IEEE Trans. Plasma Sci.* **22**, 73 (1994).
- [45] Z.-J. He and R. Haug, *J. Phys. D: Appl. Phys.* **30**, 603 (1997).
- [46] D. L. Shmelev and E. A. Litvinov, *IEEE Trans. Plasma Sci.* **25**, 533 (1997).
- [47] R. Schmoll, *J. Phys. D: Appl. Phys.* **31**, 1841 (1998).
- [48] D. L. Shmelev and E. A. Litvinov, *IEEE Trans. Dielectrics Elect. Insulation* **6**, 441 (1999).
- [49] I. V. Uimanov, *IEEE Trans. Plasma Sci.* **31**, 822 (2003).
- [50] S. A. Barengol'ts, G. A. Mesyats, and M. M. Tsventoukh, *JETP* **107**, 1039 (2008).
- [51] M. S. Benilov, M. D. Cunha, W. Hartmann, S. Kosse, A. Lawall, and N. Wenzel, *IEEE Trans. Plasma Sci.* **41**, 1950 (2013).

- [52] E. Hantzsche, *IEEE Trans. Plasma Sci.* **11**, 115 (1983).
- [53] G. A. Mesyats and I. V. Uimanov, *IEEE Trans. Plasma Sci.* **43**, 2241 (2015).
- [54] G. A. Mesyats and I. V. Uimanov, *IEEE Trans. Plasma Sci.* **45**, 2087 (2017).
- [55] X. Zhang, L. Wang, S. Jia, and D. L. Shmelev, *J. Phys. D: Appl. Phys.* **50**, 455203 (2017).
- [56] L. Wang, X. Zhang, Y. Wang, Z. Yang, and S. Jia, *Phys. Plasmas* **25**, 043511 (2018).
- [57] G. A. Mesyats and N. M. Zubarev, *J. Appl. Phys.* **117**, 043302 (2015).
- [58] M. A. Gashkov, N. M. Zubarev, O. V. Zubareva, G. A. Mesyats, and I. V. Uimanov, *J. Exp. Theor. Phys.* **122**, 776 (2016).
- [59] M. A. Gashkov, N. M. Zubarev, G. A. Mesyats, and I. V. Uimanov, *Tech. Phys. Lett.* **42**, 852 (2016).
- [60] M. S. Benilov and M. D. Cunha, *J. Phys. D: Appl. Phys.* **36**, 603 (2003).
- [61] M. S. Benilov and L. G. Benilova, *J. Phys. D: Appl. Phys.* **43**, 345204 (12pp) (2010).
- [62] N. A. Almeida, M. S. Benilov, L. G. Benilova, W. Hartmann, and N. Wenzel, *IEEE Trans. Plasma Sci.* **41**, 1938 (2013).
- [63] E. L. Murphy and R. H. Good, *Phys. Rev.* **102**, 1464 (1956).
- [64] D. L. Shmelev, S. A. Barengolts, and M. M. Tsventoukh, *IEEE Trans. Plasma Sci.* **45**, 3046 (2017).
- [65] B. Jüttner, *Beitr. Plasmaphys.* **19**, 25 (1979).
- [66] V. F. Puchkarev and A. M. Murzakayev, *J. Phys. D: Appl. Phys.* **23**, 26 (1990).
- [67] “Simulations of explosive electron emission in cathodic arcs,” CFD Research Corporation (2016).
- [68] D. Levko, R. Arslanbekov, and V. Kolobov, “Modeling of vacuum arcs with liquid-metal cathodes,” Abstract submitted to Session HW3, 71st Annual Gaseous Electronics Conference, CFD Research Corporation, DoE SBIR Phase II Contract: DE-SC0015746 (2018).

- [69] A. Herrmann, M. Balden, M. Laux, K. Krieger, H. W. Müller, R. Pugno, and V. Rohde, *J. Nucl. Mater.* **390-391**, 747 (2009).
- [70] V. Rohde, N. Endstrasser, U. v Toussaint, M. Balden, T. Lunt, R. Neu, A. Hakola, and J. Bucalossi, *J. Nucl. Mater.* **415**, S46 (2011).
- [71] D. L. Rudakov, C. P. Chrobak, R. P. Doerner, S. I. Krasheninnikov, R. A. Moyer, K. R. Umstadter, W. R. Wampler, and C. P. C. Wong, *J. Nucl. Mater.* **438**, S805 (2013).
- [72] R. A. Pitts, S. Bardin, B. Bazylev, M. A. van den Berg, P. Bunting, S. Carpentier-Chouchana, J. W. Coenen, Y. Corre, R. Dejarnac, F. Escourbiac, J. Gaspar, J. P. Gunn, T. Hirai, S.-H. Hong, J. Horacek, D. Iglesias, M. Komm, K. Krieger, C. Lasnier, G. F. Matthews, T. W. Morgan, S. Panayotis, S. Pestchanyi, A. Podolnik, R. E. Nygren, D. L. Rudakov, G. D. Temmerman, P. Vondracek, and J. G. Watkins, *Nucl. Mater. Energy* **12**, 60 (2017).
- [73] B. N. Bazylev, G. Janeschitz, I. S. Landman, A. Loarte, and S. E. Pestchanyi, *J. Nucl. Mater.* **363-365**, 1011 (2007).
- [74] B. Bazylev, G. Janeschitz, I. Landman, S. Pestchanyi, A. Loarte, G. Federici, M. Merola, J. Linke, T. Hirai, A. Zhitlukhin, V. Podkovyrov, and N. Klimov, *Fusion Eng. Des.* **83**, 1077 (2008).
- [75] S. Kajita, S. Takamura, and N. Ohno, *Nucl. Fusion* **49**, 032002 (2009).
- [76] G. V. Miloshevsky and A. Hassanein, *Nucl. Fusion* **50**, 115005 (2010).
- [77] B. Bazylev, Y. Igitkhanov, J. W. Coenen, V. Philipps, and Y. Ueda, *Phys. Scr.* **2011**, 014054 (2011).
- [78] J. W. Coenen, V. Philipps, S. Brezinsek, B. Bazylev, A. Kreter, T. Hirai, M. Laengner, T. Tanabe, Y. Ueda, U. Samm, and the TEXTOR Team, *Nucl. Fusion* **51**, 083008 (2011).
- [79] J. W. Coenen, V. Philipps, S. Brezinsek, G. Pintsuk, I. Uytendhouwen, M. Wirtz, A. Kreter, K. Sugiyama, H. Kurishita, Y. Torikai, Y. Ueda, U. Samm, and the TEXTOR-Team, *Nucl. Fusion* **51**, 113020 (2011).
- [80] S. Kajita, M. Fukumoto, M. Tokitani, T. Nakano, Y. Noiri, N. Ohno, S. Masuzaki, S. Takamura, N. Yoshida, and Y. Ueda, *Nucl. Fusion* **53**, 053013 (2013).

- [81] V. A. Makhraj, I. E. Garkusha, N. N. Aksenov, B. Bazylev, I. Landman, J. Linke, S. V. Malykhin, A. T. Pugachov, M. J. Sadowski, E. Skladnik-Sadowska, and M. Wirtz, *Phys. Scr.* **2014**, 014024 (2014).
- [82] J. W. Coenen, G. Arnoux, B. Bazylev, G. F. Matthews, A. Autricque, I. Balboa, M. Clever, R. Dejarnac, I. Coffey, Y. Corre, S. Devaux, L. Frassinetti, E. Gauthier, J. Horacek, S. Jachmich, M. Komm, M. Knaup, K. Krieger, S. Marsen, A. Meigs, P. Mertens, R. A. Pitts, T. Puetterich, M. Rack, M. Stamp, G. Sergienko, P. Tamain, V. Thompson, and J.-E. Contributors, *Nucl. Fusion* **55**, 023010 (2015).
- [83] J. W. Coenen, G. Arnoux, B. Bazylev, G. F. Matthews, S. Jachmich, I. Balboa, M. Clever, R. Dejarnac, I. Coffey, Y. Corre, S. Devaux, L. Frassinetti, E. Gauthier, J. Horacek, M. Knaup, M. Komm, K. Krieger, S. Marsen, A. Meigs, P. Mertens, R. A. Pitts, T. Puetterich, M. Rack, M. Stamp, G. Sergienko, P. Tamain, and V. Thompson, *J. Nucl. Mater.* **463**, 78 (2015).
- [84] G. F. Matthews, B. Bazylev, A. Baron-Wiechec, J. Coenen, K. Heinola, V. Kiptily, H. Maier, C. Reux, V. Riccardo, F. Rimini, G. Sergienko, V. Thompson, A. Widdowson, and J. Contributors, *Phys. Scr.* **2016**, 014070 (2016).
- [85] S. Wiesen, M. Groth, S. Brezinsek, M. Wischmeier, and J. contributors, *Phys. Scr.* **2016**, 014078 (2016).
- [86] S. Kajita, N. Ohno, S. Takamura, and Y. Tsuji, *Phys. Lett. A* **373**, 4273 (2009).
- [87] S. Kajita, S. Takamura, and N. Ohno, *Plasma Phys. Control. Fusion* **53**, 074002 (2011).
- [88] S. Kajita, N. Ohno, N. Yoshida, R. Yoshihara, and S. Takamura, *Plasma Phys. Control. Fusion* **54**, 035009 (2012).
- [89] S. Kajita, D. Hwangbo, N. Ohno, M. M. Tsventoukh, and S. A. Barengolts, *J. Appl. Phys.* **116**, 233302 (2014).
- [90] D. Hwangbo, S. Kajita, S. A. Barengolts, M. M. Tsventoukh, and N. Ohno, *Results Phys.* **4**, 33 (2014).
- [91] D. U. B. Aussems, D. Nishijima, C. Brandt, H. J. van der Meiden, M. Vilemova, J. Matejicek, G. D. Temmerman, R. P. Doerner, and N. J. L. Cardozo, *J. Nucl. Mater.* **463**, 303 (2015).
- [92] S. A. Barengolts, M. M. Tsventoukh, S. Kajita, D. Hwangbo, and N. Ohno, in *Proc. ISDEIV 2016 (Sept. 18-23, 2016, Suzhou, China)* (2016).

- [93] M. J. Baldwin and R. P. Doerner, *J. Nucl. Mater.* **404**, 165 (2010).
- [94] D. Nishijima, M. J. Baldwin, R. P. Doerner, and J. H. Yu, *J. Nucl. Mater.* **415**, S96 (2011).
- [95] S. Kajita, G. D. Temmerman, T. Morgan, S. van Eden, T. de Kruif, and N. Ohno, *Nucl. Fusion* **54**, 033005 (2014).
- [96] S. Kajita, T. Yagi, K. Kobayashi, M. Tokitani, and N. Ohno, *Results Phys.* **6**, 877 (2016).
- [97] S. A. Barengolts, G. A. Mesyats, and M. M. Tsventoukh, *Nucl. Fusion* **50**, 125004 (2010).
- [98] S. A. Barengolts, G. A. Mesyats, and M. M. Tsventoukh, in *Proc. ICPIG 2011 (Aug. 28-Sep. 2, Belfast, Northern Ireland, UK)* (2011).
- [99] M. D. Cunha, H. T. C. Kaufmann, M. S. Benilov, W. Hartmann, and N. Wenzel, *IEEE Trans. Plasma Sci.* **45**, 2060 (2017).
- [100] H. T. C. Kaufmann, M. D. Cunha, M. S. Benilov, W. Hartmann, and N. Wenzel, *J. Appl. Phys.* **122**, 163303 (2017).
- [101] M. H. Kim, “A thorough numerical model of cathode spots challenges conventional wisdom,” AIP Scilight (2017).
- [102] M. S. Benilov, M. D. Cunha, W. Hartmann, and N. Wenzel, *Plasma Sources Sci. Technol.* **23**, 054007 (2014).
- [103] M. S. Benilov, N. A. Almeida, M. Baeva, M. D. Cunha, L. G. Benilova, and D. Uhrlandt, *J. Phys. D: Appl. Phys.* **49**, 215201 (2016).
- [104] E. Hantzsche, *Beitr. Plasmaphys.* **22**, 325 (1982).
- [105] M. S. Benilov and L. G. Benilova, *J. Appl. Phys.* **114**, 063307 (2013).
- [106] J. Paulini, T. Klein, and G. Simon, *J. Phys. D: Appl. Phys.* **26**, 1310 (1993).
- [107] Y. S. Touloukian, R. W. Powell, C. Y. Ho, and P. G. Clemens, *Thermal Conductivity, Metallic Elements and Alloys., Thermophysical Properties of Matter, vol. 1* (IFI/Plenum, New York-Washington, 1970).
- [108] C. Y. Ho, R. W. Powell, and P. E. Liley, *J. Phys. Chem. Ref. Data* **1**, 279 (1972).
- [109] D. R. Lide, *CRC Handbook of Chemistry and Physics, 84th edition* (CRC Press, 2003).

- [110] I. S. Grigoriev and E. Z. Meilikhov, eds., *Handbook of Physical Quantities* (CRC Press, Boca Raton, 1997).
- [111] W. F. Gale and T. C. Totemeier, eds., *Smithells Metals Reference Book*, 8th ed. (Elsevier Butterworth-Heinemann, Amsterdam and Boston, 2004).
- [112] G. R. Gathers, *Int. J. Thermophysics* **4**, 209 (1983).
- [113] G. K. White and M. L. Minges, *Int. J. Thermophysics* **18**, 1269 (1997).
- [114] R. W. Lewis and K. Ravindran, *Int. J. Numer. Meth. Engng.* **47**, 29 (2000).
- [115] M. J. Assael, A. E. Kalyva, K. D. Antoniadis, R. M. Banish, I. Egry, J. Wu, E. Kaschnitz, and W. A. Wakeham, *J. Phys. Chem. Ref. Data* **39**, 033105 (2010).
- [116] J. A. Cahill and A. D. Kirshenbaum, *J. Phys. Chem.* **66**, 1080 (1962).
- [117] V. E. Fortov, I. T. Iakubov, and A. G. Khrapak, *Physics of Strongly Coupled Plasma* (Oxford University Press, Oxford, 2007).
- [118] E. Hantzsche, *IEEE Trans. Plasma Sci.* **17**, 657 (1989).
- [119] I. G. Brown and X. Godechot, *IEEE Trans. Plasma Sci.* **19**, 713 (1991).
- [120] S. A. Barenholts, D. L. Shmelev, and I. V. Uimanov, *IEEE Trans. Plasma Sci.* **43**, 2236 (2015).
- [121] T. Matsumoto, H. Fujii, T. Ueda, M. Kamai, and K. Nogi, *Meas. Sci. Technol.* **16**, 432 (2005).
- [122] D. A. Harrison, D. Yan, and S. Blairs, *J. Chem. Thermodynamics* **9**, 1111 (1977).
- [123] B. J. Keene, *Int. Mater. Rev.* **38**, 157 (1993).
- [124] K. Nogi, K. Ogino, A. McLean, and W. A. Miller, *Metall. Trans. B* **17**, 163 (1986).
- [125] A. Anders, S. Anders, B. Juettner, and H. Lueck, *IEEE Trans. Plasma Sci.* **24**, 69 (1996).
- [126] V. Alexiades, N. Hannoun, and T. Z. Mai, *EJDE* **2003**, 55 (2003).
- [127] V. R. Voller and C. Prakash, *Int. J. Heat Mass Transfer* **30**, 1709 (1987).
- [128] A. D. Brent, V. R. Voller, and K. J. Reid, *Numer. Heat Transfer* **13**, 297 (1988).

- [129] P. C. Carman, *Trans. Instn. Chem. Engrs.* **15**, 150 (1937).
- [130] S. J. Osher and J. A. Sethian, *J. Comput. Phys.* **79**, 12 (1988).
- [131] E. Olsson and G. Kreiss, *J. Comput. Phys.* **210**, 225 (2005).
- [132] E. Olsson, G. Kreiss, and S. Zahedi, *J. Comput. Phys.* **225**, 785 (2007).
- [133] J. A. Sethian and P. Smereka, *Annu. Rev. Fluid Mech.* **35**, 341 (2003).
- [134] J. U. Brackbill, D. B. Kothe, and C. Zemach, *J. Comput. Phys.* **100**, 335 (1992).
- [135] L. Wang, S. Jia, D. Yang, K. Liu, G. Su, and Z. Shi, *J. Phys. D: Appl. Phys.* **42**, 145203 (2009).
- [136] L. Wang, S. Jia, Y. Lin, B. Chen, D. Yang, and Z. Shi, *J. Appl. Phys.* **107**, 113306 (2010).
- [137] L. Wang, X. Zhou, H. Wang, Z. Qian, S. Jia, D. Yang, and Z. Shi, *IEEE Trans. Plasma Sci.* **40**, 2237 (2012).
- [138] X. Huang, L. Wang, J. Deng, S. Jia, K. Qin, and Z. Shi, *J. Phys. D: Appl. Phys.* **49**, 075202 (2016).
- [139] B. Juettner and V. Puchkarev, in *Handbook of Vacuum Arc Science and Technology: Fundamentals and Applications*, edited by R. L. Boxman, D. M. Sanders, and P. J. Martin (Noyes Publications, Park Ridge, N.J., U.S.A., 1995) pp. 73–151.
- [140] E. Hantzsche, in *Handbook of Vacuum Arc Science and Technology: Fundamentals and Applications*, edited by R. L. Boxman, D. M. Sanders, and P. J. Martin (Noyes Publications, Park Ridge, N.J., U.S.A., 1995) pp. 151–208.
- [141] M. S. Benilov, *IEEE Trans. Plasma Sci.* **32**, 249 (2004).
- [142] M. S. Benilov and A. Marotta, *J. Phys. D: Appl. Phys.* **28**, 1869 (1995).
- [143] P. Talias, *Nucl. Mater. Energy* **13**, 42 (2017).
- [144] S. W. H. Yih and C. T. Wang, *Tungsten: Sources, Metallurgy, Properties, and Applications* (Plenum Press, New York, 1979).
- [145] P. D. Prewett and J. E. Allen, *Proc. R. Soc. Lond. A* **348**, 435 (1976).
- [146] F. A. Soldera, F. T. Mucklich, K. Hrastnik, and T. Kaiser, *IEEE Trans. Vehicular Tech.* **53**, 1257 (2004).

- [147] N. Jeanvoine and F. Muecklich, *J. Phys. D: Appl. Phys.* **42**, 035203 (2009).
- [148] N. Jeanvoine, *Plasma-material interaction and electrode degradation in high voltage ignition discharges*, Ph.D. thesis, Universitaet des Saarlandes, Saarbruecken (2009).
- [149] M. Janda and Z. Machala, *IEEE Trans. Plasma Sci.* **39**, 2246 (2011).
- [150] M. Benmouffok, P. Freton, P. Teulet, and J. J. Gonzalez, in *Proc. 14th HTPP 2016 (July 2-7, Munich, Germany)* (2016).
- [151] A. Karpatne, D. P. Breden, and L. Raja, *Simulations of Spark-Plug Transient Plasma Breakdown in Automotive Internal Combustion Engines*, Tech. Rep. SAE Technical Paper 2017-01-0563 (SAE International, 2017).
- [152] D. P. Breden, A. Karpatne, and L. Raja, *Modelling of Electrode Erosion for Prediction of Spark Plug Lifetime*, Tech. Rep. SAE Technical Paper 2018-01-0175 (SAE International, 2018).
- [153] A. Hamdan, C. Noel, F. Kosior, G. Henrion, and T. Belmonte, *J. Appl. Phys.* **113**, 043301 (2013).
- [154] A. Hamdan, F. Kosior, C. Noel, G. Henrion, J. N. Audinot, T. Gries, and T. Belmonte, *J. Appl. Phys.* **113**, 213303 (2013).
- [155] S. I. Tkachenko, K. V. Khishchenko, V. S. Vorob'ev, P. R. Levashov, I. V. Lomonosov, and V. E. Fortov, *High. Temp.* **39**, 674 (2001).
- [156] V. I. Oreshkin, S. A. Barengol'ts, and S. A. Chaikovsky, *Tech. Phys.* **52**, 642 (2007).
- [157] D. Sheftman and Y. E. Krasik, *Phys. Plasmas* **17**, 112702 (2010).
- [158] A. E. Barysevich and S. L. Cherkas, *Phys. Plasmas* **18**, 052703 (2011).
- [159] H. Hess, *J. Phys. D: Appl. Phys.* **24**, 36 (1991).
- [160] J. H. Peterson, K. G. Honnell, C. W. Greeff, J. D. Johnson, J. C. Boettger, and S. D. Crockett, in *American Institute of Physics Conference Series*, Vol. 1426 (2012) pp. 763–766.
- [161] S. P. Lyon and J. D. Johnson, *SESAME: The Los Alamos National Laboratory Equation of State Database*, Tech. Rep. LA-UR-92-3407 (Los Alamos National Laboratory, 1992).